



**UNIVERSITÀ
DI SIENA 1240**

University of Siena
Department of Molecular and Developmental Medicine

Ph.D. in
Molecular Medicine
CYCLE XXXIV
COORDINATOR Prof. Vincenzo Sorrentino

**Morpho-functional investigation of cardiac
remodeling in an arrhythmogenic mouse
model by advanced optical methods.**

Academic Discipline (SSD) BIO/09

Doctoral Candidate

Francesco Giardini

Supervisor

Dr. Leonardo Sacconi

Tutors

Prof. Elisabetta Cerbai

Prof. Corrado Poggesi

Academic Year **2020/2021**

Contents

1	Summary	2
2	Introduction.....	4
2.1	Cardiac anatomy and physiology	5
2.1.1	Cardiac macroscopic anatomy	5
2.1.2	Cardiac microscopic anatomy	7
2.1.3	Cardiac conduction system	9
2.1.4	Action Potential physiology	12
2.1.5	Cardiac cycle.....	15
2.2	Cardiac pathophysiology	16
2.2.1	Sinus rhythm and arrhythmogenesis	17
2.2.2	Cardiac tissue remodeling	20
2.2.3	Arrhythmogenic Cardiomyopathy	26
2.3	Functional imaging: cardiac optical mapping.....	28
2.4	Optical methods for anatomical investigation of the heart	30
2.4.1	Histological Imaging.....	30
2.4.2	Tissue clearing techniques	32
2.4.3	Optical imaging of clarified samples.....	36
3	Methods.....	41
3.1	Animal models.....	42
3.2	Isolated and perfused mouse heart	42

3.3	Optical Mapping platform and Arrhythmia induction	43
3.3.1	Optical Mapping platform.....	43
3.3.2	Optical recording and arrhythmia induction protocol.....	45
3.3.3	Optical mapping image analysis.....	45
3.4	Whole heart clearing	46
3.4.1	Tissue clearing method.....	46
3.4.2	Histological analysis on clarified tissue	47
3.5	Whole heart reconstruction	48
3.5.1	MesoSPIM setup	48
3.5.2	Acquisition protocol	53
3.5.3	Images pre-processing.....	54
3.6	Image analysis	57
3.6.1	Myocardium anatomy and fibrosis quantification	57
3.6.2	Orientation fibers reconstruction and analysis	59
3.6.3	Fibrosis and fiber disarray spatial distribution	63
3.7	Alignment of LV fibrosis maps with optical mapping images	65
3.8	Data visualization and statistical analysis.....	67
3.8.1	Statistical analysis.....	67
3.8.2	Data visualization	67
4	Results	69
4.1	Functional data	70
4.1.1	Optical mapping of cardiac electrical activity.....	70
4.1.2	Arrhythmias	73

4.2	Whole heart reconstruction	76
4.2.1	Cleared tissue preservation	76
4.2.2	Image acquisition and analysis.....	77
4.3	Mesosopic structural investigation.....	87
4.3.1	Myocardium fiber organization	87
4.3.2	Quantification of fibrotic tissue.....	98
4.3.3	Spatial correlation between fibrosis and fibers disarray	100
4.4	Morpho-Functional Correlation.....	103
4.4.1	Alignment of morpho-functional data	103
4.4.2	Fibrosis impacts on AP propagation.....	104
5	Discussion and Conclusion.....	107
6	Glossary.....	116
7	Table of Figures.....	119

1 Summary

Severe remodeling processes may occur in the heart due to both genetic and non-genetic diseases. Structural remodeling, such as collagen deposition (fibrosis) and cellular misalignment, can affect electrical conduction at different orders of magnitude and, eventually, lead to arrhythmias. In this scenario, arrhythmogenic cardiomyopathy (ACM) is an inherited heart disease that involves ventricular dysfunction, arrhythmias, and localized replacement of contractile fibers with fibrofatty scar tissue. Unfortunately, nowadays, predicting the impact of fine structural alterations on the electrical disfunction in entire organs is challenging, due to the inefficacy of standard imaging methods in performing high-resolution three-dimensional reconstructions in massive tissues.

In this work, we developed a new full-optical correlative approach to quantify and integrate the electrical dysfunctions with three-dimensional structural reconstructions of entire hearts, both in controls and in a mouse model of ACM. We combined optical mapping of the action potential propagation (APP) with advances in tissue clearing and light-sheet microscopy techniques. First, we employed an optical platform to map and analyze the APP in Langendorff-perfused hearts. Then, we optimized the SHIELD procedure for the clearing of cardiac tissue, thus converting the previously electrically characterized samples into well-preserved and fully-transparent specimens. A high-throughput light-sheet microscope has been developed allowing the reconstruction of the whole mouse heart with a micrometric resolution allowing fine quantification of myocytes alignment and fibrosis deposition across the organ. Finally, we developed a software pipeline that employs high-resolution 3D images to analyze and co-register

APP maps with the 3D anatomy, contractile fibers disarray, and fibrosis deposition on each heart. We found that although fiber disarray is not involved in this remodeling process, the accumulation of fibrotic patches found in the ACM mouse model can deform the propagating wavefront potentially facilitating the formation of reentry circuits.

We believe that this promising methodological framework will allow clarifying the involvement of fine structural alterations in the electrical dysfunctions, thus enabling a unified investigation of the structural causes that lead to electrical and mechanical alterations after the tissue remodeling.

2 Introduction

2.1 Cardiac anatomy and physiology

2.1.1 Cardiac macroscopic anatomy

The heart is the center of the cardiovascular system, and ensures, through its rhythmic contractions, the flow of blood in the systemic circulation. It is a muscular-membranous organ, located in the thoracic cavity in the anterior mediastinum region: located between the two lungs, above the diaphragm, which separates it from the abdominal viscera, behind the sternum and the intercostal cartilages, which protect it.

The heart has the shape of a flattened truncated cone, and has a base facing upward, backward, to the right, corresponding to the atrial component, and an apex facing forward, downward, to the left, corresponding to the ventricular component. In the heart, we can also distinguish an anterior face, the sternocostal face, and a posterior face, the diaphragmatic face.

On the outside, the heart is enclosed in the pericardial sac, which protects it and keeps it in place. Internally, the heart is divided into four cardiac chambers: two posterior-superior, right atrium and left atrium, and two antero-inferior, the right and left ventricles. The right atrium communicates with the right ventricle (RV) through the atrioventricular (AV) orifice, which has an AV valve called the tricuspid valve. It is formed by three fibrous, avascularized flaps, termed cusps: their free edge is attached to thin cords of fibrous tissue, the chordae tendineae, which in turn originate from the papillary muscles, located on the inner surface of the RV. Similarly, the cavity of the left atrium communicates with the left ventricle (LV) through an AV orifice, which has a valve called the bicuspid or mitral valve, formed by two cusps. The two right cavities do not communicate with those of the left but are separated by a continuous wall, the upper portion of which, the interatrial septum, separates the two atria, while the lower portion, the interventricular septum, separates the two ventricles.

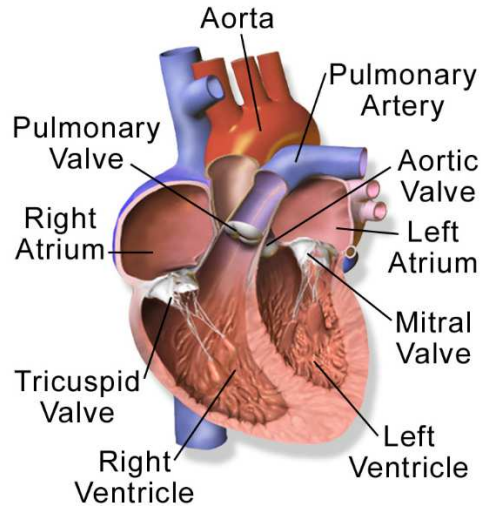


Figure 1: Cardiac anatomy. Frontal section of the heart. Arrows indicate the main components (1).

The pulmonary valve is located between the RV and the pulmonary artery, while the aortic valve is located between the LV and the aorta. The correct functioning of these four valves is fundamental to ensure that during the cardiac cycle the blood proceeds in a single direction, established by the pressure gradient, preventing retrograde flows.

The heart can be considered to function as two separate pumps working in series: the right atrium and RV pumping blood from the systemic veins into the pulmonary circulation; the left atrium and LV pumping blood from the pulmonary veins into the systemic circulation. Specifically, the right atrium receives non-oxygenated blood both from the heart itself, through the coronary sinus, and from the systemic circulation, through two large veins: the inferior vena cava and the superior vena cava. From the right atrium, blood passes to the RV, which pumps it into the pulmonary circulation through the pulmonary arteries. The oxygenated blood refluxed from the pulmonary circulation is collected in the left atrium through the four pulmonary veins, and from there it flows into the LV, which, by contracting,

pumps it back into the systemic circulation through the aorta. Then, from the aorta originate all the branches of the vascular network, which allow the blood to reach the peripheral tissues (2).

2.1.2 Cardiac microscopic anatomy

The cardiac wall is mainly formed by three different types of cells: fibroblasts, endothelial cells, and cardiomyocytes, where the latter constitutes about 75% of the entire cardiac mass. In section, the wall is composed, from the outside to the inside, of three overlapping layers: epicardium, myocardium, and endocardium.

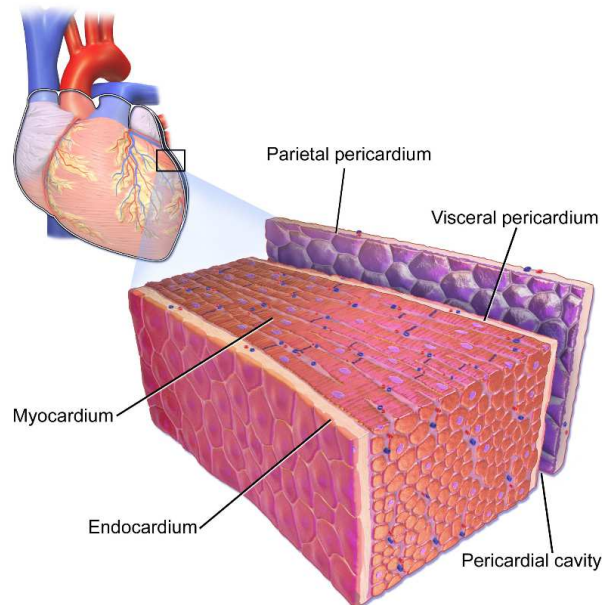


Figure 2: Section of the cardiac wall. The different layer that compose it are represented: from the inside towards the outside, there is the endocardium, the myocardium, and the visceral pericardium, which constitutes the epicardium. This is followed by the pericardial cavity and finally the parietal pericardium (1).

The epicardium is the outermost layer: it consists of a serous membrane made up of a superficial mesothelium sheet, and a layer of loose connective

tissue that adheres to the underlying myocardium. The myocardium, the middle and thickest layer, represents the muscular component of the cardiac wall, and contains cardiac striated muscle tissue, connective tissue, blood vessels, and nerves; it is this layer that allows the organ to contract. Finally, there is the endocardium, consisting of a thin layer of epithelial cells that line the heart valves and chambers, as well as the entire circulatory system (2).

The myocardium is made up of individual elements called cardiomyocytes, striated cells with a diameter of about 10-20 μm and a length of about 50-100 μm . Their shape is cylindrical, with the ends often divided into two or more branches that make contact with the branches of adjacent elements.

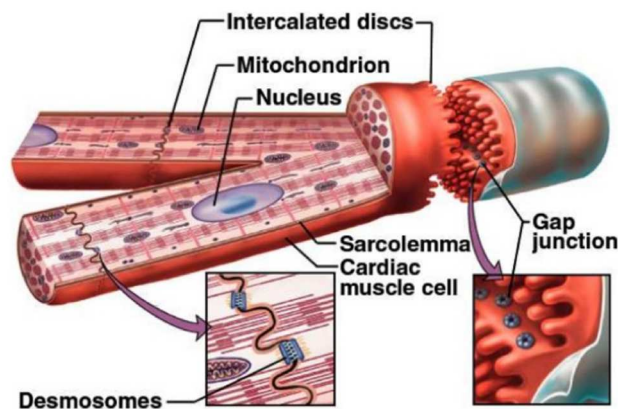


Figure 3: Cardiomyocyte. External and internal structure of a cardiomyocyte. In detail, the main constituents of the intercalary discs. Modified from (3).

The cardiomyocytes are organized in a complex three-dimensional network: from a functional point of view, the heart muscle is defined as a functional syncytium, i.e. all cells contract synchronously, coordinated by the electrical system of the heart. This means that the individual cardiomyocytes have specialized structures in their contact zones, known as intercalary discs, in

which are located gap junctions that allow almost completely free diffusion of ions between adjacent cells. It is the presence of these gap junctions that makes the heart a functional syncytium.

The plasma membrane of cardiomyocytes, the sarcolemma, forms characteristic invaginations called T-tubules, which penetrate to the center of the cell. These structures are essential for the correct propagation of the action potential (AP), as they ensure that the depolarizing current propagates synchronously. Inside, these cells have an extensive smooth endoplasmic reticulum, the sarcoplasmic reticulum, and this forms a single dilated terminal cisterna which is coupled to the T-tubules at the Z-line: this complex is called a dyad. Instead, the structure formed by a T-tubule surrounded on the right and left by the cisternae of the sarcoplasmic reticulum is called a triad; this arrangement facilitates a rapid supply of calcium ions, which allow muscular contraction.

More specifically, the heart is composed of two syncytia, as the atria are separated from the ventricles by an electrically non-conductive fibrous layer that surrounds and supports the valves. A specialized cardiac conduction system is therefore required to ensure adequate transmission of electrical excitation from the atria to the ventricles (4).

2.1.3 Cardiac conduction system

Cardiac muscle contractions are generated by signals originating within the muscle itself; for this reason, the contractile activity of the cardiac muscle is called myogenic. More precisely, cardiac tissue is defined as excitable because it is capable of generating an AP, a wave of depolarization of the cell membrane which, following a stimulus, propagates throughout the tissue.

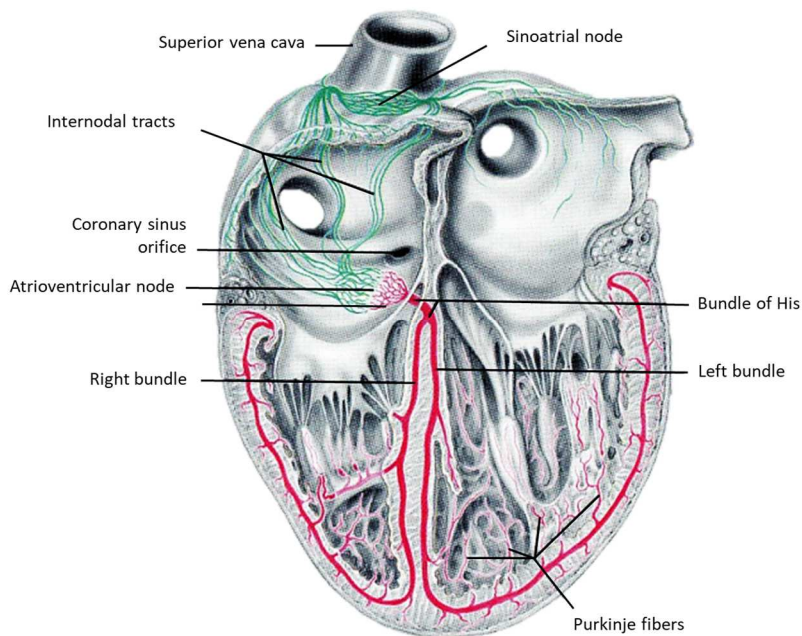


Figure 4: Cardiac conduction system. The anatomical pathways of the cardiac conduction system are shown in a four chamber view (5).

The anatomical structures that allow the conduction of the electrical impulse in the heart are:

- the sinoatrial node: located in the upper epicardial wall of the right atrium, next to the orifice of the superior vena cava;
- the AV node: an endocardial structure located in the lower part of the interatrial groove, near the tricuspid valve;
- His bundles: runs through the right fibrous trigone and the membranous part of the septum, dividing into a right and a left bundle;
- the Purkinje fibers: these form the terminal part of the conduction system, and with their thin terminal branches penetrate the myocardium. These structures allow the common depolarisation front to be transmitted to all the cardiomyocytes.

The conduction system is the only electrical link between the atria and ventricles: the AV node allows impulses to pass between the atria and ventricles and is responsible for protecting the ventricle from atrial arrhythmias.

The heart's ability to generate signals that periodically activate its contractions is called autorhythmicity; it is due to the action of a small percentage of modified muscle cells, called autorhythmic cells, which are essential for the heart's pumping action (6).

In particular, the heart has a specialized tissue made up of two types of cells: pacemaker cells, which trigger APs and set the heart's rhythm, and conduction fibers, which conduct APs and propagate them through the heart. These cells constitute the heart's conduction system. Pacemaker cells are concentrated in the sinoatrial node (SA node) and the AV node. The heartbeat is generated by impulses originating in the SA node because the SA node has a higher discharge frequency than the AV node cells (70 impulses/minute for the SA node; 50 impulses/minute for the AV node).

Under physiological conditions, the sequence of electrical events begins in the SA node, with the onset of the excitation wave that depolarises the atria; the wave is then conducted to the cells of the AV node, which propagates it to the ventricles after an interval of 170-200 ms. This delay separates the mechanical contraction of the atria from that of the ventricles: atrial contraction thus precedes ventricular contraction. From the AV node, the wave passes to the AV bundle, the bundle of His, where the wave divides into the right and left bundle branches, which conduct the impulse to the right and LV respectively. The wave then continues through the extensive network of Purkinje fiber branches, which reach the apex of the ventricles: from here, the wave spreads upwards, thus depolarising the ventricles.

These latter structures allow a common depolarisation front to be generated and transmitted to all the cardiomyocytes. The depolarising wave is called the excitation wave and generates muscle contraction.

If the SA node ceases to generate impulses, or if conduction between the nodes is blocked, the AV node begins to generate them, so that ventricular contraction is normal (7).

2.1.4 Action Potential physiology

Membrane potential is defined as the difference in potential between the two sides of the plasma membrane: a cardiomyocyte at rest has an electrical membrane potential of approximately -90 mV. This value is maintained by ATP-dependent Na⁺/K⁺ pump, which transports 3 sodium ions (Na⁺) out of the cell and simultaneously introduce 2 potassium ions (K⁺). This causes sodium to be more concentrated on the outside, while potassium is more concentrated on the inside.

Ion channels, transmembrane proteins that regulate the passage of specific ions between the inside and outside of the cell and thus modifying the electrical membrane potential, are responsible for generating the AP. When a stimulus reaches a cardiomyocyte, the membrane potential becomes less negative: if the membrane potential reaches the threshold value of -60 mV, an AP is generated. The AP is an all-or-none event: once the threshold value is reached, the amplitude of the AP no longer depends on the stimulus (6).

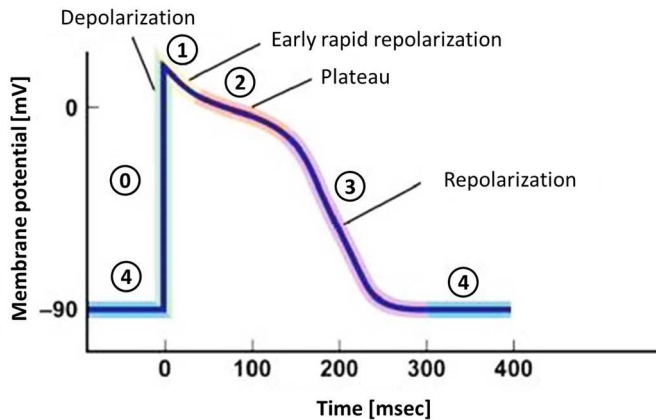


Figure 5: Phases of the membrane action potential. Representation of the membrane action potential phases in a cardiomyocyte. Modified from (8).

The AP can be divided into 4 phases:

- Phase 0 (depolarisation): entry of sodium into the cell-mediated by the opening of voltage-dependent fast sodium (Na^+) channels. The increased flux of Na^+ ions makes the cell's membrane potential more positive, inducing the opening of additional Na^+ channels. The result is a depolarization of the membrane potential, which reaches $+30/+40$ mV.
- Phase 1 (hyper-polarisation): The Na^+ channels that had opened in phase 0 start to become inactivated. This reduces the flow of Na^+ into the cell, leading the membrane potential to negative values. However, the value of the membrane potential drops only slightly: voltage-dependent potassium (K^+) channels close, reducing the outflow of K^+ ; at the same time, L-type Ca^{2+} channels open, increasing the flow of Ca^{2+} into the cell. These changes maintain membrane depolarization;
- Phase 2 (plateau): minimal leakage of K^+ that maintains the membrane potential slightly positive; during this phase, Ca^{2+} entering the cell through L-type channels causes the sarcoplasmic

reticulum to slowly release Ca^{2+} ; this phenomenon is known as calcium-induced calcium release;

- Phase 3 (repolarisation): the opening of K^{+} channels increases the release of K^{+} from the cell, causing the membrane potential to fall to more negative values. This fall of the potential towards negative values causes the Ca^{2+} channels to close, and the Ca^{2+} flux inside the cell decreases. These events repolarise the membrane to its resting value, terminating the AP;
- Phase 4 (resting): thanks to the ATP-dependent $\text{Na}^{+}/\text{K}^{+}$ pump, the cell recovers ionic balance.

The cardiomyocyte is no longer excitable from phase 0 to the middle of phase 3 (absolute refractory period) and returns to being excitable in phase 4. The second part of phase 3 is known as the relative refractory period: the cell may be excited, but only if the stimulus reaching it is intense.

Contractile cells are connected to conduction cells by communicating junctions, allowing the AP to propagate. However, the mechanism underlying the AP of pacemaker cells is different from that of contractile cells.

Indeed, the AP of pacemaker cells is preceded by a slow depolarization, in which the spontaneous entry of positive ions (Na^{+} , K^{+} , and Ca^{2+}) leads to the threshold value for the onset of the subsequent AP being exceeded. Under resting conditions, the membrane potential of these cells is less negative (-55 mV) and more unstable, because it is characterized by a mixed cationic current of Na^{+} (incoming) and K^{+} (outgoing). This current, called Funny current, is activated at the end of each AP, and through this mechanism controls the frequency of spontaneous activity of the pacemaker cells.

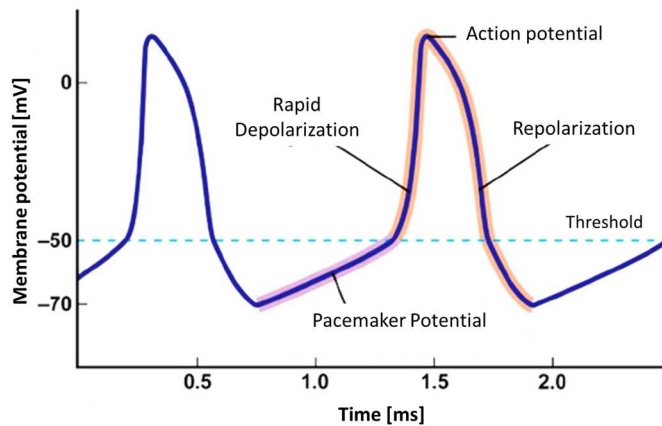


Figure 6: Action potential of a peacemaker cell. Representation of the electrical activity of a pacemaker cell. Modified from (8).

In pacemaker cells the final phase is therefore no longer called the resting phase, but “spontaneous slow depolarization phase”, and is the mechanism responsible for cardiac automatism (8).

2.1.5 Cardiac cycle

The heart functions as a suction and pressure pump, where the energy required is provided by the contraction of the heart muscle itself. A cardiac cycle consists of all the events from the beginning of one beat to the beginning of the next, and can be divided into two parts: systole, when the heart contracts, and diastole, when it relaxes. The different parts of the heart, beat in an orderly sequence: first the atria contract (atrial systole), and then the ventricles (ventricular systole); during the diastole phase, all four heart chambers are relaxed.

Consider the cardiac cycle starting from the diastolic resting phase, in which the atria and ventricles are relaxed; the semilunar valves are closed because the ventricular pressure is lower than the aortic pressure, and the AV valves

have not yet begun to open. Blood arrives at the heart and enters the atria: as the atria fill up, a pressure difference is created between them and the still empty ventricles. The AV valves then open, yielding to the pressure of the atria, and the blood passes into the ventricles, which begin to fill. At the end of diastole, the atria contract (atrial systole), pushing more blood into the ventricles.

The ventricular systole phase then begins: the ventricles begin to contract, increasing the pressure inside them. The pressure in the ventricles begins to exceed the pressure in the atria, and consequently, the AV valves close, as their cusps are pushed upwards by the pressure of the blood mass in the ventricles. This ensures the correct directionality of flow. The pressure within the ventricles then continues to increase further, until the pressure in the left and RVs exceeds the pressure in the aorta and pulmonary artery, and the aortic and pulmonary valves open. When the aortic and pulmonary valves open, ventricular ejection begins: blood is pumped into the aorta and pulmonary arteries, and ventricular pressure decreases. When the ventricular pressure falls below the aortic pressure, the semilunar valves close. This ends systole, and diastole begins again: blood enters the atria but does not flow into the ventricles because the AV valves are still closed. When the ventricular pressure decreases compared to the atrial pressure, the AV valves open and the cardiac cycle begins again (7).

2.2 Cardiac pathophysiology

Cardiovascular diseases represent the main cause of death in Europe with great social and economic burdens. Unfortunately, there are many families of cardiovascular diseases differing in etiology, pathogenesis, effects, and severity, up to the risk of death. Among them, there are acquired and congenital diseases that, as a result of cardiac remodeling processes,

determine alterations in electrical conduction with consequent electromechanical dysfunction and the development of arrhythmias.

This section will describe the main features of cardiac arrhythmias and cardiac remodeling processes due to pathology.

2.2.1 Sinus rhythm and arrhythmogenesis

The normal heart rhythm is called sinus rhythm (SR), in which each beat is spontaneously generated from the SA node. The heart rhythm is typically monitored by an electrocardiogram (ECG): P wave is associated with atria contraction, QRS complex is associated with ventricles contraction and the T wave is associated with ventricles relaxation. The time required for the electrical impulse to reach the first point where begins the activation of the ventricles is called PR interval, while the time in which the ventricles contract and relax is called QT interval (9) (Figure 7, panel A).

Arrhythmias are defined as alterations in the normal rhythm of the heart: the heartbeat may be slower (bradycardia), faster (tachycardia), and/or irregular (fibrillation) compared to the physiological rate (Figure 7, panel B). Arrhythmias are classified according to the structure where they are thought to have originated and the mechanism that is presumed to be at the root of the disorder. In particular, arrhythmias are divided into supraventricular, when they originate in the SA node, atria, or AV junction, and ventricular, when they originate below the bifurcation of the bundle of His. Ventricular tachycardia is one of the most common and also one of the most dangerous arrhythmias; it can degenerate into ventricular fibrillation, the outcome of which is often fatal (10).

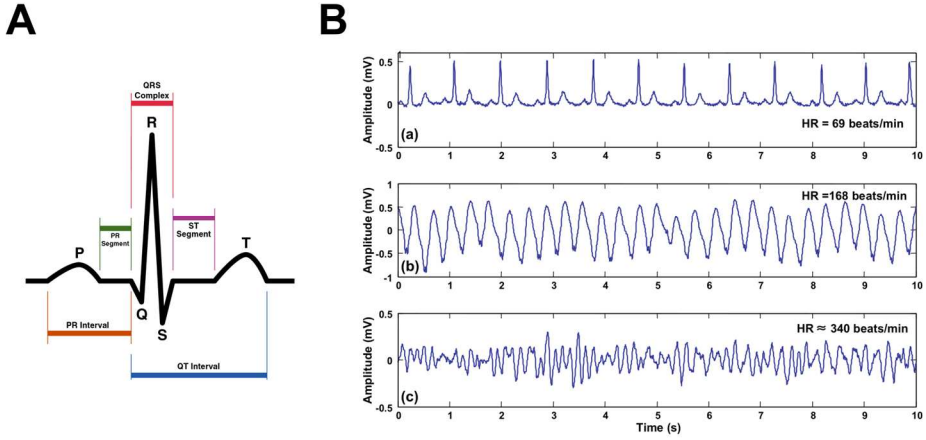


Figure 7: Schematization of ECG traces of SR and different cardiac rhythms. (A) Scheme of electrocardiogram (ECG) trace of one beat of cardiac SR with waves and segments names. P wave: atrial contraction; QRS complex: ventricle activation and contraction; T wave: ventricle repolarization; PR segment: time interval between atrioventricular (AV) node and ventricles activation; QT segment: depolarization and repolarization of ventricles. From (11). (B) Human ECGs during normal sinus rhythm (SR), top; ventricular tachycardia (VT), middle; and ventricular fibrillation (VF), bottom. from (12).

The main cause of many cardiac arrhythmias is the onset of cardiac re-entry. The mechanism was first described in 1913 by Mines and remains a valid model to this day (13).

Normally, the heart is endowed with anisotropy: when a stimulus arrives from the upper part of the region considered (for example, in the case of the ventricle, from the AV node), it follows orderly pathways, dictated by the direction of the muscle bundles. When the propagation fronts following these paths collide with each other, they are blocked in their propagation. This is possible due to a fundamental characteristic of the heart, namely the existence of a refractory period: at the moment of collision, the neighboring tissue regions are in their absolute refractory period, and this prevents the propagation of a wavefront in the tissue area just crossed by the other front.

However, a situation known as unidirectional blocking can be generated, where the stimulus coming from a region above encounters an area where it cannot continue, or where the speed of its conduction decreases. At the final moment of collision, the neighboring tissue zones will no longer be in their absolute refractory period, due to the delay of the stimulus that has occurred in the block. The zone that is still excitable is then traversed in a retrograde direction, and thus a vicious circle is formed, defined as a re-entry circuit: this consists of an excitation wave that propagates along a more or less constant closed path, disinterested in the stimuli coming from the upper part, and that to self-maintain itself must find at the beginning of each cycle the tissue in excitable conditions.

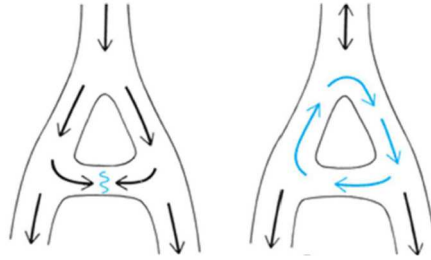


Figure 8: Scheme of a reentrant circuit. Schematic representation of the difference in impulse conduction between a healthy tissue and a re-entrant circuit. From (10).

For generate an anatomically based re-entry circuit to be found in normal tissue, it is necessary to establish a unidirectional block, i.e. the presence of an area that is only capable of conducting in one direction. For the stimulus to re-enter the same area, the conduction velocity (CV) must decrease in at least one region of the circuit, or its refractoriness must change. Re-entry is therefore a phenomenon in which a single electrical impulse gives rise to two or more propagating waves, which can be caused by both pathophysiological and anatomical mechanisms. Pathophysiological causes may be abnormalities in conduction, heterogeneity in resting potential, AP amplitude, and refractoriness of the affected area. Anatomical causes of re-

entry may be the presence of damaged tissue and abnormal conduction structures (14, 15).

2.2.2 Cardiac tissue remodeling

2.2.2.1 Definition of cardiac remodeling

Cardiac remodeling is defined as all the structural changes that occur in the heart wall in response to damage. The phenomenon begins with a defect in the contractile capacity of the affected portion of the wall, which, together with morphological changes such as compensatory cardiomyocyte proliferation, resulting in a distortion of the normal profile of the cardiac chamber. In particular, these mechanisms generate cardiac hypertrophy and extensive production of extracellular matrix (ECM) (16).

This phenomenon is not exclusively due to acute damage, such as a myocardial infarction, but occurs in all those conditions that lead to a modification of the dynamic balance between the central cardiac thrust and the peripheral body resistances, as found in chronic arterial hypertension, in many valvular alterations, in most congenital heart diseases, and even during normal body growth.

The heart has several regulatory mechanisms to increase its function and cope with increased workload:

- The Frank-Starling mechanism, that is the regulation by changes in fiber length; increased filling volumes lead to dilation of the heart, thus enhancing the number of functional cross-links within the sarcomeres and so improving contractility.
- Activation of neurohumoral systems, such as the release of noradrenaline by the autonomic nervous system, activation of the renin-angiotensin-aldosterone system, or the release of atrial natriuretic peptide.

- Regulation by biochemical changes within myocardial cells (myocardial contractility and excitation-contraction coupling);

In its initial phase, in fact, remodeling is a compensatory adaptive response, effective in case of acute hemodynamic overloads or in the initial phases of chronic overloads; however, in case of persistent phenomena, it can lead to Desmoglein-2 gene (DSG2) structural changes which in turn represent a risk factor for the onset of arrhythmias, even fatal ones (17, 18).

Remodeling can therefore be described as physiological or DSG2, where the physiological one is the set of those adaptive mechanisms that normally occur during pregnancy, growth, or exercise, with a response that is gradually established following an increase in workload for the heart over a longer or shorter time. DSG2 remodeling, on the other hand, occurs after acute events and is an attempt to maintain or restore cardiac function that has been abruptly damaged by necrosis (19).

Physiological remodeling is usually harmonic, and as such it affects the entire cardiac chamber (atrial and/or ventricular), whereas DSG2 remodeling is typically segmental, and almost exclusively affects the LV. The latter will be characterized by an irregular profile of its walls: it will present thinning and akinesia in the damaged area, and compensatory hypertrophy in the surrounding uninjured regions.



Figure 9: Cardiac remodeling in pathology. Comparison of longitudinal four chambers sections of a hypertrophied human heart (left) and a healthy human heart (right). From (20).

2.2.2.2 Pathogenesis of cardiac remodeling

Following injury, necrosis of cardiomyocytes causes a loss of contractile activity and thinning of the affected area. This results in a decrease in ejection fraction, followed by ventricular dilatation reflecting an attempt to maintain an adequate systolic outflow. The uninjured cardiomyocytes are overworked, having to compensate for the lack of contractility of the lost neighboring cardiomyocytes, and undergo compensatory hypertrophy. Both of these phenomena are accompanied by a proliferation of fibroblasts, which are responsible for the deposition of collagen and thus for the healing of the injured area. The loss of contractile elements is called early remodeling.

As time goes by, a vicious circle is established: there is an increase in parietal tension, ventricular enlargement, and this all starts to involve both the injured and the non-infarcted and scarred areas. This process is called late remodeling (21).

The main changes that occur therefore concern the architecture of the cardiac chambers, the cardiomyocyte component, and the organization of the ECM.

2.2.2.3 Alterations to the cardiac chambers

From a hemodynamic point of view, the ventricular cavity is normally kept under tension during the different phases of the cardiac cycle by forces acting on the ventricular wall, which create a situation of dynamic equilibrium, where the ventricle does not collapse completely in systole and does not expand excessively in systole.

The forces from which this equilibrium arises are, on the one hand, the pre- and post-load, and on the other hand, the tension developed by the ventricular walls (intrinsic contractility). The pre-load, that is the venous return, promotes diastolic dilation of the ventricular cavity; the afterload, represented by peripheral resistances, opposes ventricular dilation. Finally, intrinsic contractility (independent of venous return and peripheral resistance) is responsible for systolic contraction, which occurs as a result of the union of actin and myosin filaments following the release of Ca^{2+} ions.

In the damaged area, this intrinsic contractility is lost: the venous return remains unchanged, and since it is no longer counterbalanced by contractility, it ends up favoring ventricular distortion. The systolic thrust of the infarcted area is lost, while the contractile function is maintained in the remaining uninjured segments. This distortion induces an asynchrony of motion between the injured and uninjured areas, which in turn causes an irregularity in the cardiac profile, distorting the normal ventricular architecture and altering ventricular function (22).

2.2.2.4 Alterations to the cardiomyocyte component

The main alterations that occur in the cardiomyocyte are modification of the excitation-contraction coupling, hypertrophy, myocytolysis, and alteration of cytoskeleton proteins.

At the initial stage of cardiac hypertrophy, the number of myofibrils and mitochondria within the cardiomyocytes increases: at this stage, the cells are larger, but their organization is still normal. Subsequently, there is a

reduction in the number of individual contractile elements (myocytolysis), and the physiological organization of the sarcomeres is lost.

Together with hypertrophy, there is a switch in the myocyte's biological phenotype, due to the reactivation of a whole series of genes that are normally no longer expressed after birth. At the same time, the expression of genes typical of the adult heart is reduced.

Fetal gene re-expression is promoted by various stimuli: stretching and stressing of the myocyte through stimulation of its mechanoreceptors, neurohormones (as for instance noradrenaline and angiotensin 2), inflammatory cytokines (TNF, IL-6), growth factors (such as endothelin), and reactive oxygen species (ROS) (nitric oxide (NO), superoxide (O₂⁻)). The activation of the fetal genetic program is an attempt to adapt the myocardium to DSG2 stress conditions: the transition/the switch to a fetal type of metabolism (anaerobic) allows a reduction in energy required, but leads to a decrease in contractility; these phenomena therefore soon prove to be maladaptive (22).

2.2.2.5 Alterations to the extracellular matrix

Apart from cardiomyocytes, the other element modified during cardiac remodeling is the extracellular matrix (ECM). The ECM consists of the basal membrane, a network of fibrillar collagen surrounding the cardiomyocytes, proteoglycans, glycosaminoglycans, and specialized proteins, such as matricellular proteins.

Fibrillar collagen, types 1 and 3, ensures the structural integrity of adjacent myocytes and is essential for maintaining the alignment of myofibrils even within the myocyte itself, through interaction with integrins and cytoskeletal proteins. The three-dimensional organization of the ECM thus plays an essential role in maintaining the structural and functional integrity of the heart (23).

Following an insult, tissue repair begins with the migration of inflammatory cells, such as monocytes and macrophages, to the site of the injury. Subsequently, fibroblasts are also activated and generate a deposition of scar collagen to replace the lost cardiomyocytes. This process is an attempt to circumscribe the necrotic area, but tends to extend beyond the affected tissue, affecting healthy tissue as well. Indeed, fibroblasts play an important role in cardiac remodeling: one of the central events is their conversion into myofibroblasts, which produce and deposit collagen, glycoproteins, and proteoglycans (e.g. fibronectin, galectins, and periostin), with the formation of scar tissue.

The formation of fibrotic structures requires a multi-step process, involving the degradation and processing of pre-existing ECM to remove damaged tissue, and the production, secretion, cross-linking, and maturation of new ECM. Following damage, a repair process is then established that leads to the progressive replacement of myocardial cells with connective tissue: this deposition of connective tissue leads to fibrosis (24, 25).

Myocardial fibrosis is therefore an endogenous, suboptimal mechanism of heart repair: it can provide structural support while cardiomyocyte loss occurs, but without their adequate replacement. Given its complex pathophysiology, new models of study are desirable to better understand and characterize fibrotic processes, which could allow a better understanding of the phenomenon (26).

2.2.3 Arrhythmogenic Cardiomyopathy

Arrhythmogenic Cardiomyopathy (ACM) is a hereditary disease that predominantly affects the RV. It is a genetic pathology with autosomal dominant transmission and incomplete penetrance.

The disease generally has its onset at a young age, a stage in which no major structural alterations of the tissue have been observed. Instead, proceeding to the more advanced stages, a progressive replacement of the contractile tissue with fibrotic material is observed (27). As a result of this anomaly, the right ventricular wall is no longer able to adequately support the effort of the cardiac contraction and therefore brings to slow degeneration. From a histological point of view, the disease is characterized by the progressive loss of the myocardial tissue, followed by its fibrofatty substitution, which proceeds from the epicardium to the endocardium, up to the involvement of the entire wall. This pathological process leads, on the one hand, to the gradual thinning and dilation of the RV wall, progressively from a simple regional kinetic anomaly, up to the deterioration of the global contractile function; on the other hand, it constitutes the arrhythmic substrate. The presence of fibrofatty tissue interspersed with cardiac muscle tissue predisposes the patient to the development of life-threatening arrhythmias and right ventricular dilation.

Moreover, if the LV is dilated too, the disease can progress towards heart failure. Indeed, right ventricular involvement is predominant and more evident, but the LV is also significantly affected; the increasingly frequent occurrence of forms with biventricular or predominantly left ventricular involvement, has led to the need to replace the original definition of “Arrhythmogenic right ventricular cardiomyopathy” with the expression “Arrhythmogenic cardiomyopathy”, in order to encompass all the phenotypic forms of the disease in a single phrase (28, 29).

ACM has a slow evolutionary course. Over time, the majority of the patients show changes in the ECG and structural abnormalities of the heart echocardiogram and cardiac magnetic resonance (30).

In most patients, cardiomyopathy is caused by the congenital weakening of the structures that connect and hold together the cardiomyocytes, the so-called “desmosomes”. Nowadays, 14 genes related to the pathology have been discovered and, between the genes known so far, at least 9 of them code for proteins that are involved in the formation of the cellular junctions of intercalary discs. They consist of both mechanical junctions such as the desmosomes and gap junctions, which make the cytoplasm of two adjacent cardiomyocytes directly communicate. Based on the literature, 80-85% of the mutations are located in 3 genes: Desmoplakin, Plakophilin-2, and Desmoglein-2 (27, 30-33).

2.2.3.1 DSG2^{mut/mut} mouse model

To further investigate the role of desmosomes-related mutations in pathology, recently Chelko and colleagues generated a novel mouse strain carrying a mutation in the DSG2 in all DSG2-expressing cells (DSG2^{mut/mut} mice) (34, 35). Authors employed the Cre-Lox system to obtain the germline deletion of exons 4-5 in the DSG2 gene. This causes a frameshift mutation yielding a truncated form of the protein, which is subsequently degraded, thus resulting in the knock-down of the DSG2 protein in all DSG2-expressing cells. Homozygous DSG2^{mut/mut} mice start to present the signs typical of the disease at 8 weeks of age. At the structural level, the animals showed similar characteristics to patients with ACM (36-39). DSG2^{mut/mut} hearts show cardiomyocyte death, inflammatory infiltrate, and fibrotic remodeling, which started to appear at the level of the RV wall, but, lately, also affects the LV. Fatty areas have been described at the level of the atrial-ventricular junction. Such structural alterations lead to contractile dysfunction (evaluated as decreased fractional shortening and ejection fraction) and

increased arrhythmias propensity. Notably, in line with human disease, male mice were more affected than female ones. Heterozygous mice also develop the disease, which, however, requires more time to become evident (i.e. 6-8 months). For the similarity in the phenotype of $DSG2^{mut/mut}$ mice with the human disease, we employed it in this study as a pathological model of ACM.

2.3 Functional imaging: cardiac optical mapping

Cardiac optical mapping is a widely used imaging technique for investigating cardiac electrophysiology in intact Langendorff-perfused hearts.

Optical mapping techniques are based on the use of Voltage Sensitive Dyes (VSDs). The most used voltage-sensitive indicators are organic chromophores that bind to the outer cellular membrane and exhibit electrochromism as mechanism of voltage sensing. The electrochromic mechanism is a direct interaction of the electric field with the dye and does not require any movement of the chromophore. This means that the dye rapidly responds to the membrane potential variations by altering their emission spectra in response to changes in transmembrane voltage. As result, changes in the quantity of emitted fluorescent light, are proportional to changes in transmembrane voltage, allowing a non-invasive assessment of transmembrane voltage changes, such as AP (40).

Optical mapping imaging is performed in wide-field configuration. The heart is perfused *ex vivo* and stained with a VSD, which binds to the outer layer of the cardiomyocytes membrane. The VSD is then excited by entirely illuminating the heart surface with a light source with the appropriate excitation wavelength, which corresponds to the VSD's absorption spectrum.

When it returns to its ground state from its excited state, the VSD emits photons of a wavelength longer than that of the excitation light thanks to the electrochromism. The emitted photons are then filtered and focused by a system of optics onto a photodetector, which quantifies the amount of emitted fluorescent light for each of its multiple pixels. Therefore, each pixel represents a measure of fluorescent intensity collected from a specific location on the tissue preparation at a specific time (Figure 10).

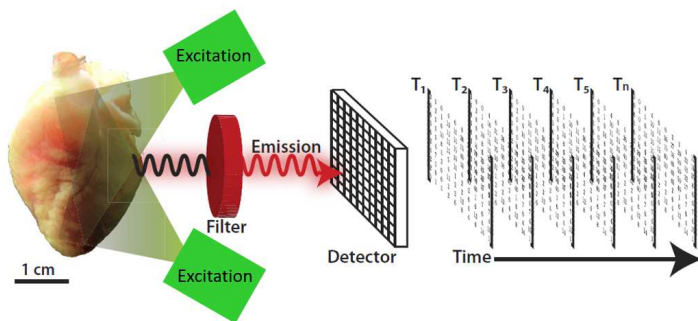


Figure 10: Optical mapping setup and data acquisition. The heart is stained with a VSD which emits a fluorescence signal when excited by the excitation light source. The emitted fluorescence light is filtered and detected, and the data is collected from a camera as a series of matrixes of fluorescent intensity at different time points. Modified from (41).

The photodetector measuring the emission light is typically the sensor of a high-speed, high dynamic range, camera (charge-coupled devices, CCD or scientific complementary metal-oxide-semiconductor, sCMOS). The high dynamic range of the camera is an important feature to amplify the small-amplitude fluorescent signals of the dye (ΔF), which need to be extracted from the overall raw fluorescent light (F).

One advantage of optical mapping is the ability to simultaneously record optical APs from a large number of sites, allowing the generation of extremely high-resolution activation maps of the whole heart. The activation map, usually shown as an isochronal map, is generated by assigning to all

pixels their activation times and it is easier to create when the heart is in SR or a paced rhythm than in a re-entrant rhythm or fibrillation, in which the myocardium is being continuously activated. Because changes in fluorescence intensity are proportional to changes in transmembrane voltage, AP duration (APD) values can be calculated from the optical signal, enabling the generation of APD maps.

APD maps are a valid tool to investigate apical-basal or endocardial-epicardial gradients in APD or its spatial heterogeneities, which are important in arrhythmogenesis. Optical mapping data can also be used to generate local conduction vectors, allowing quantification of local CV, as well as providing a description of myocardium wave-front direction.

Due to its high temporal resolution, cardiac optical mapping is used to image normal and abnormal electrical activity in intact hearts, increasing knowledge of cardiac electrophysiological processes, as well as a deeper understanding of complex arrhythmias. Indeed, providing maps of wave dynamics during heart rhythm disorders, this imaging technique has had a huge impact on the understanding of cardiac arrhythmias (42, 43).

2.4 Optical methods for anatomical investigation of the heart

2.4.1 Histological Imaging

Organs and tissues are made up of many different cell types, each responsible for a specific role. The overall activity of the biological structure derives from the interconnections and cooperation of the individual cells that constitute it. Cardiac tissue is not an exception: it is made up of individual cardiomyocytes arranged according to a precise organization, which, by

interacting with each other, make the process of cardiac contraction perfectly rhythmic and synchronized, thus ensuring that the heart functions correctly.

Therefore, it is essential to study the organ in its entirety to fully understand its physiological and DSG2 aspects.

Performing high-resolution imaging in massive tissues is, however, extremely complex due to the phenomenon of light scattering. This process, caused by the different nature and therefore the different refractive index (RI) of the biomolecules that compose them, causes the tissues to deflect the light used for their observation, both the excitation and the detection one: they so appear opaque, and resolution is lost by going deeper (44).

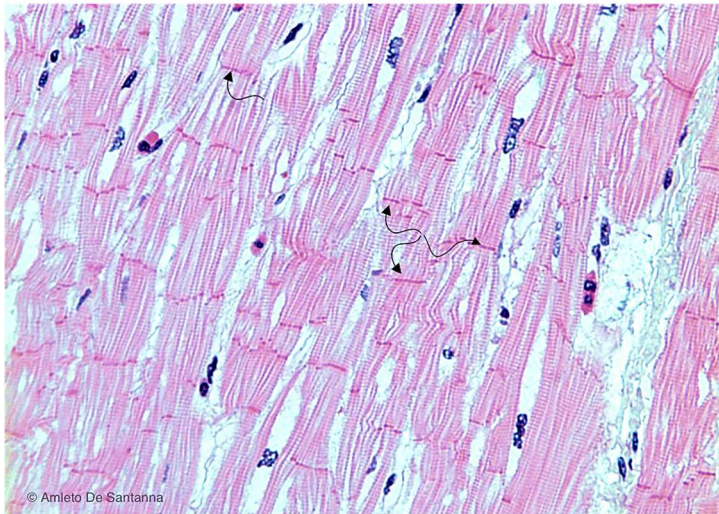


Figure 11: Histological imaging of contractile human heart tissue. The transversal striae, nuclei, and intercalary discs (black arrows), placed at the cell-cell junction system, are evident. From (45).

To date, histological investigations have overcome this limitation by mechanically sectioning the sample using an instrument called microtome. It is thus possible to obtain very thin tissue slices, even of the order of 1

micron, to facilitate their observation under the microscope due to their reduced thickness (46).

However, this approach has its criticalities: the mechanical sectioning may damage or distort the tissues, and reconstructing the three-dimensional structure of the sample by aligning and reassembling the images obtained from each section is a process that requires complex, costly, and time-consuming computer procedures.

In recent years, several methodologies have been developed to defeat the limitations of classical histology and the nature of biological tissues, thus overcoming the limitations imposed both by classical histology and the nature of biological tissues.

2.4.2 Tissue clearing techniques

The various biomolecules that compose tissues and organs are characterized by different RIs (approximately 1.33 for water, 1.43 for proteins, and 1.44 for lipids) (47). In microscopy, due to this internal inhomogeneity, the acquisition of images of large samples has been severely limited by light scattering.

Refractive index is a nondimensional parameter that quantifies the reduction in the propagation speed of incident light passing through a certain material and it depends on the material itself. This mechanism explains why light doesn't propagate well within biological tissues, which are opaque, preventing the acquisition of images beyond a certain depth.

To overcome this limitation, various optical clearing techniques have been developed in recent years to make the RI inside and outside the sample homogeneous; this makes the samples optically transparent and minimizes scattering effects so that light can penetrate deep into the tissue.

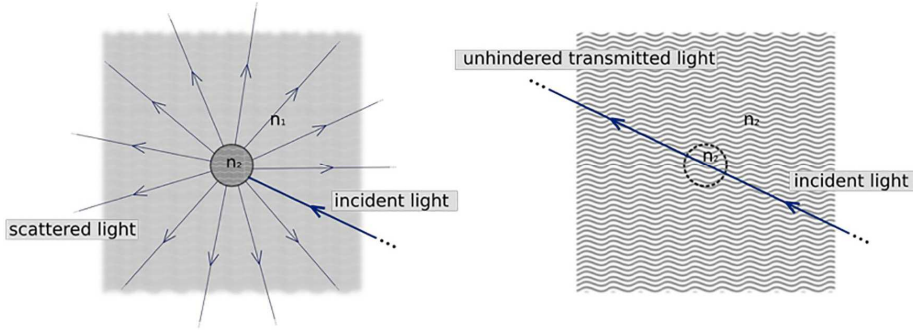


Figure 12: Schematic representation of light scattering before and after an optical clearing process. On the left, light is deflected due to the different refractive indices ($n_1 \neq n_2$) of the diverse media it passes through. On the right, light is not deflected, because the diverse media it passes through have the same refractive index ($n_2 = n_2$). From (44).

The clearing techniques are based on the removal of the elements that contribute to tissue inhomogeneity through a process of delipidation and/or decolorization, without altering the morphological structure of the tissue, and by immersing it into substances with a RI matching to the average RI of the sample (RI matching). The tissue becomes clarified, which means transparent, and light can pass through it.

Other optical clearing techniques that have been developed over the years can be divided according to the type of solvents used.

In the organic solvent-based methods, the procedure mainly consists of two steps: first, the sample is dehydrated by immersing it in alcoholic solutions, thus removing water molecules which present the lower RI (such as methanol or tetrahydrofuran), while at the same time dissolving and removing part of the lipids. Subsequently, the sample is placed in organic solvents, such as BABB (1:2 benzyl alcohol and benzyl benzoate) or dichloromethane, which intercalate with the sample to remove residual lipids. At the end of the process, the spaces previously occupied by water and lipids are filled with the organic solvent: by choosing solvents with the same index as the proteins, the RI is homogenized and the tissue is clarified (48).

The best-known techniques are BABB, 3DISCO, and iDISCO: all of them guarantee high transparency of the sample through quick and easy steps, but due to the initial dehydration process, they induce alterations in the shape and a reduction in the size of the tissue (49-51).

Therefore, methods based on aqueous solutions have been developed.

In simple immersion methods, the sample is placed in a water-based solution in which molecules with a high RI have previously been dissolved. However, these techniques are mainly suitable for thin samples: the solutions used are characterized by a high viscosity at the concentrations necessary to obtain RI matching, which prevents their penetration into the deeper layers of the tissue. Their ability to clear in massive samples is therefore limited. Simple immersion techniques are for example FocusClear, SeeDB, and TDE (2,2'-thiodiethanol) (52-54).

On the contrary, in hyperhydration methods, the sample is placed for days or months in a solution of water, non-hydrophobic detergents (as TritonTM X-100) to remove lipids, and urea, which penetrates the tissue and generates an osmotic gradient that promotes the entry of additional water. Here, the effectiveness of clearing increases as the degree of hydration increases. It results in greater expansion of the treated tissue which may undergo alterations in its morphological structure. In addition, urea can cause the denaturation of internal proteins.

Rather than attempting to change only the RI of the solvent in which the sample is immersed, alternative approaches have been developed that are based on tissue transformation processes, to change the RI of the sample itself, thus allowing it to be more effectively homogenized with the substance in which it is immersed.

In hydrogel-based techniques, acrylamide monomers and a fixative are introduced into the sample, and subsequently, polymerization is induced. This creates a supporting scaffold within each cell that keeps all the proteins

connected, giving the tissue the structural integrity to withstand subsequent treatments. Indeed, the sample is then delipidated and decolorized by being soaked for a certain period in a strong solution containing a high concentration of a detergent, the Sodium Dodecyl Sulphate (SDS), with simultaneous application of electrophoresis to accelerate the delipidation step. After that, the sample is subjected to RI matching by simple immersion to achieve the desired transparency.

The most widely used technique of this type is called CLARITY (55). However, the CLARITY-cleared samples become very gelatinous, so they have to be handled very carefully and it is easy to introduce damages to the tissue while performing the staining and/or imaging procedures.

A valid alternative is offered by the SHIELD technique, which produces a uniformly rigid and transparent sample (56).

2.4.2.1 SHIELD tissue transformation protocol

The SHIELD protocol (Stabilization to Harsh conditions via Intramolecular Epoxide Linkages to prevent Degradation) (57) allows large volumes of tissue to become optically transparent through a process of tissue transformation. The protocol is based on a polyepoxy resin, characterized by a flexible molecular structure with numerous epoxy groups, which can form intramolecular cross-links with the amino groups of proteins and nucleic acids. Due to these bonds, an internal scaffold is created, which protects the tertiary structure of the biomolecules, and their functions, from subsequent stress factors (such as heat, detergents, organic solvents, acidic pH). The polyepoxy resin is also able to form cross-links between several endogenous biomolecules, to keep them in their physiological positions and increase mechanical stability. The SHIELD protocol thus protects the native tissue architecture from subsequent delipidation and clearing processes.

This protocol is structured as follows. The sample is initially incubated in a solution called SHIELD-OFF, containing the polyepoxy resins that create specific bonds with proteins and nucleic acids to form the solid scaffold that maintains the integrity of the tissue. Then, it is immersed in the SHIELD-ON solution, which is a buffer solution, and afterward, it is incubated in the clearing solution, which contains SDS, a lipophilic molecule, which binds to the lipids; the periodic change of this solution causes the lipids, which have bound to the SDS micelles, to be removed from the tissue. At the end of the process, it is possible to obtain entire organs that are optically transparent and perfectly preserved in their structure.

2.4.3 Optical imaging of clarified samples

2.4.3.1 *Light-sheet Microscopy*

To obtain a detailed anatomical reconstruction of clarified samples, it is necessary to employ imaging techniques that guarantee high spatial resolution and reasonable scan times. To date, the best performing technique for massive imaging of clarified specimens is the Light Sheet Fluorescence Microscopy (LSFM).

The basic scheme of LSFM is to illuminate the sample with a light-sheet, coupled with a wide-field detection system positioned orthogonally to the direction of propagation of the light-sheet (Figure 13).

By decoupling the excitation system from the detection one (widefield type), it is possible to collect the signal from the entire field of view (FOV) in parallel. Such a system allows for significantly shorter imaging times compared to previous techniques, such as confocal microscopy, whilst maintaining effective optical sectioning provided by the localization of the excitation. This configuration allows a radial resolution determined by the detection optics, and therefore expressed by Abbe's formula, while the axial resolution (optical sectioning) is dictated by the thickness of the light sheet.

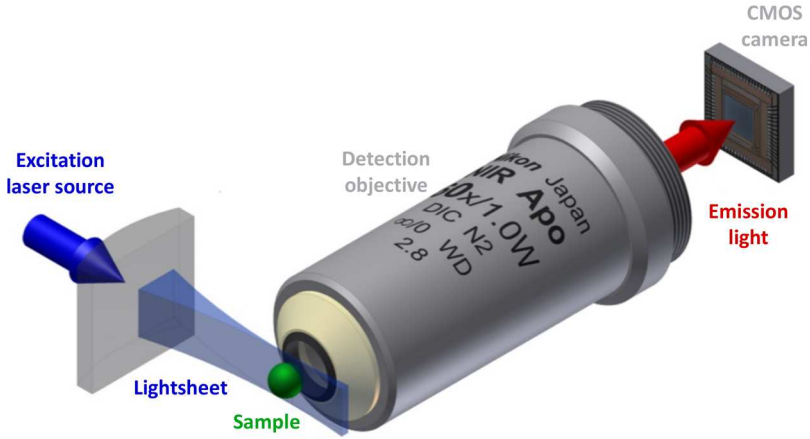


Figure 13: **Light-sheet fluorescence microscope.** Representative scheme of the functioning of a light-sheet fluorescence microscope (LSFM) (58).

To date, the light-sheet can be realized dynamically with galvanometric mirrors instead of using a cylindric lens. The light beam is sent to the mirror that, rotating along its axis, shift the entrance position of the rays into the converging lens, thus moving the light beam throughout the illumination plane. By rotating the mirror at high speed, a “virtual” sheet of light is generated. Compared to using a cylindric lens, this mechanism ensures a uniformly light intensity along the image plane and less corruption of the light sheet in presence of impurities in the sample.

The excitation beam has a Gaussian profile (Fig. 15) characterized by the following thickness:

$$w(z) = w_0 \sqrt{1 + \left(\frac{z}{z_R}\right)^2}$$

The parameter w_0 represents the value assumed by the thickness $w(z)$ at the focal distance, that is the minimum thickness of the light sheet, also called the waist, and is given by:

$$w_0 = \frac{\lambda}{\pi NA}$$

where NA is the numerical aperture of the lens that focuses the beam. From the profile of the excitation beam, we can also define the depth of focus (b) defined as:

$$b = \frac{2\pi w_0^2}{\lambda}$$

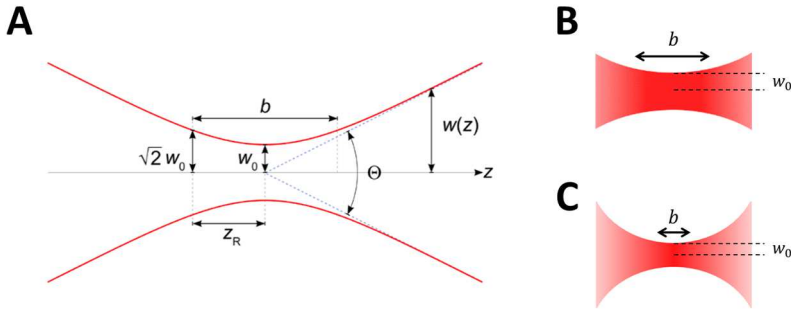


Figure 14: Gaussian profile. Scheme of a gaussian profile with main parameters (A) and two Gaussian profiles obtained with small (B) and big (C) numerical aperture (NA) objective respectively.

Both the thickness of the light sheet and its depth of focus, therefore, depend on the NA of the excitation system: higher NA generates a thin light sheet, but with a limited extension of the focusing zone (Figure 14, panel C), while lower NA generates a large light-sheet but with low sectioning power (Figure 14, panel B), compromising the possibility of analyzing three-dimensional structures with an isometric resolving power.

Different types of light-sheet microscopes have been developed over time, aimed at overcoming the main problems of the basic technique. In our study,

we chose to use a new generation of light-sheet microscopy called *MesoSPIM*, which allows us to acquire an entire mouse heart in a single tomographic scan with micrometric resolution.

2.4.3.2 *MesoSPIM Initiative*

MesoSPIM technology is a new generation of LSFM that combine the Axially Scanned Light-Sheet Microscopy (ASLM) technique with the rolling-shutter mechanism of the sensor to overcome the limitation that binds $w(z)$ and b (Figure 15) (59-61).

In detail, the beam is translated along the excitation plane using an Electrically Tunable polymeric Lens (ETL), an optical component capable of modifying its curvature, and consequently its focal distance. In this way, it is possible to translate the light-sheet waist inside the sample sweeping the imaging plane (i.e., along the X-axis), while the light-sheet is dynamically generated with the galvanometric mirrors along the Y-axis.

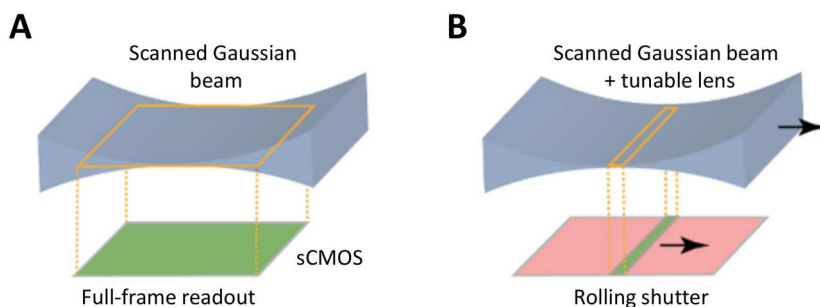


Figure 15: MesoSPIM rolling shutter mechanism. Schemes of a static light-sheet (A) and a dynamic light-sheet generated by synchronizing the rolling shutter of the camera with the light beam (B). MesoSPIM technology exploits dynamic light-sheet. From (61).

The sensor consists of an sCMOS camera set in rolling shutter mode: only a window of pixels is kept active and synchronized with the position of the

light-sheet waist; this ensures to acquire only the fluorescence signal from the area of the sample illuminated by the waist of the light sheet, and any fluorescence from other out-of-focus areas is therefore not detected because it reaches dull pixels.

Therefore, by combining the synchronization between excitation and sensor along the X-axis with the dynamic generation of the light-sheet along the Y-axis, it is possible to scan an entire XY plane with FOVs large enough to reconstruct the entire sample without a mosaic image reconstruction approach. This makes the acquisition much faster, with high optical sectioning and wide FOV, allowing to scan with the best possible axial resolution an entire plane of the clarified sample. In addition, the sample is only illuminated at the same time as the detection, which greatly reduces the effects of phototoxicity and photobleaching.

3 Methods

3.1 Animal models

For this study, nine C57BL/6J male mice and nine DSG2^{mut/mut} male mice were used. C57BL/6J mice were provided from Envigo S.R.L., while DSG2^{mut/mut} (DSG2 +/+ , or simply DSG2) mice were provided from Prof. Marco Mongillo and Dr. Tania Zaglia laboratories in Padua, Italy.

All experimental procedures performed on rodents were approved by the local ethical committee of the Ministry of Health (Authorization number 408/2018PR and 944/2018-PR) in compliance with Italian Animal Welfare Law (Law n.116/1992 and subsequent modifications). All procedures were performed by trained personnel with documented formal training and previous experience in experimental animal handling and care.

The animals were sacrificed at two different time points of age: 7 and 13 months.

3.2 Isolated and perfused mouse heart

CTRL and DSG2 mice (7 and 13 months old) were heparinized (0.1 mL at 5,000 units/mL) and anesthetized by inhaled isoflurane (5%). The excised heart was immediately bathed in Krebs-Henseleit (KH) solution and cannulated through the aorta. The KH buffer contained (in mM): 120 NaCl, 5 KCl, 2 Mg₂SO₄·7H₂O, 20 NaHCO₃, 1.2 NaH₂PO₄·H₂O, and 10 glucose pH 7.3 when equilibrated with carbogen (5% CO₂-95% O₂). Cardiac contraction was inhibited for the entire experiment with blebbistatin (5 µM) in the solution. The cannulated heart was retrogradely perfused (horizontal-Langendorff's perfusion) with the KH solution and then transferred to a

custom-built optical mapping chamber at a constant flow of 2.5 mL/min at 37°C. Two platinum electrodes were placed below the heart for monitoring cardiac electrical activity via ECG (Figure 16). After stabilization of the ECG, typically within a few seconds, 1 mL of perfusion solution containing the voltage-sensitive dye (di-4-ANBDQPQ; 5 μ g/mL, University of Connecticut Health Center, Farmington, CT, USA) (62) was bolus injected into the aorta.

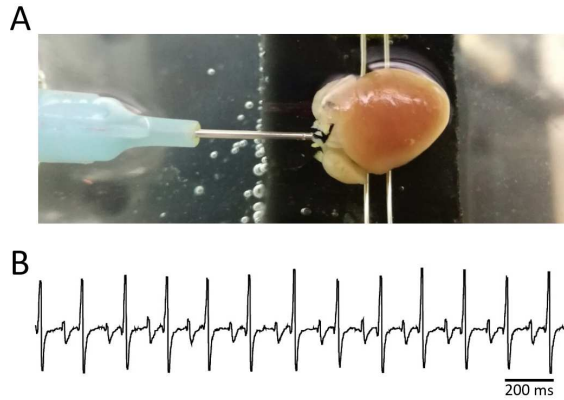


Figure 16: Picture of the mouse heart retrogradely perfused with Langendorff system. (A) The mouse heart was positioned in the recording chamber and retrogradely perfused with a constant flow of 2.5 mL/min at 37°C. (B) ECG tracing of the sinus rhythm was recorded using two platinum electrodes placed below the heart.

3.3 Optical Mapping platform and Arrhythmia induction

3.3.1 Optical Mapping platform

Optical mapping was performed using a custom-made mesoscope (Figure 17)(63). The whole mouse heart was illuminated in wide-field configuration using a $\times 2$ objective (TL2x-SAP, Thorlabs, Newton, NJ, USA) and a light

emitted diode (LED) operating at a wavelength centered at 625 nm (M625L3, Thorlabs) followed by a band-pass filter at 640/40 nm (FF01-640/40-25, Semrock, Rochester, NY, USA). The heart was illuminated with a maximum intensity of 1 mW/mm². A dichroic beam splitter (FF685-Di02-25 × 36, Semrock) followed by a band-pass filter at 775/140 nm (FF01-775/140-25, Semrock) was used for collecting the VSD-emitted fluorescence. A ×20 objective (LD Plan-Neofluar ×20/0.4 M27, Carl Zeiss Microscopy, Oberkochen, Germany) was used to focus the fluorescence in a central portion (128 × 128 pixels) of the sensor of an sCMOS camera (OrcaFLASH 4.0, Hamamatsu Photonics, Shizuoka, Japan) operating at a frame rate of 1 kHz (1 ms actual exposure time), with a resulting pixel size of 78 μm.

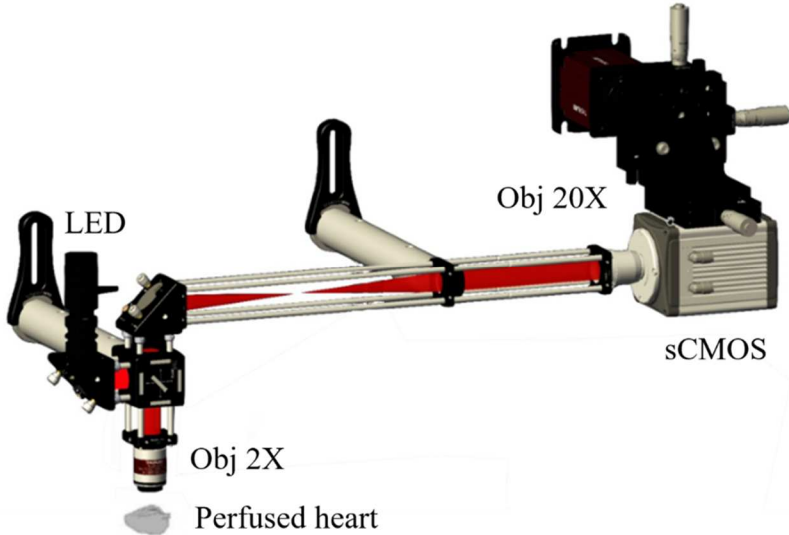


Figure 17: Scheme of the wide-field fluorescence mesoscope. A red LED followed by a band-pass filter (640/40 nm) excites through a 2× objective the whole mouse heart, stained with a red-shifted electro-chromic voltage-sensitive dye (Di-4-ANBDQPQ). A dichroic beam splitter followed by a band-pass filter (775/140 nm) is used for collecting the emitted fluorescence signal. A 4f system is adopted to collimate the beam onto a 20× objective. The signal is then focused into a central portion (128×128 pixels) of an sCMOS sensor operating at a framerate of 1 kHz (1 ms actual exposure time). Modified from (64).

3.3.2 Optical recording and arrhythmia induction protocol

The wide field mesoscope previously described was used to optically map AP propagation in mouse hearts. All experiments were performed at 36 ± 0.5 °C. To overcome the SR, mice hearts were electrically paced at the apex to follow AP propagation along conduction fibers. Using a bipolar electrode, a burst of 15 electrical stimuli for each frequency was delivered to the apex of the heart. Electrical stimulation frequency used: 5, 6, 8 Hz. For electrical stimulation, an Isolated Constant Voltage Stimulator (DS2A, Digitimer, Welwyn Garden City, Hertfordshire, UK), was used to deliver precisely adjustable voltage pulses, without introducing noise into the optical recordings.

To investigate susceptibility to arrhythmias, we mimicked the ventricular parasystole rhythm, wherein an ectopic pacemaker activity is protected from the impulse of the sinus pacemaker (65). Experimentally, the aim is to keep the sinus node (SN) intact and induce extra beats. In detail, we performed 4 trials where mouse hearts were electrically paced for 10 s at the right ventricular outflow tract (RVOT) at a period of $1.7 \times (\text{SN period of the mouse heart})$.

3.3.3 Optical mapping image analysis

All programs for optical mapping data acquisition and analysis are developed with LabVIEW 2015 (National Instruments, version 15.0, 64bit) which allows designing programs used for data acquisition, instrument control, and data analysis.

For optical recordings, $\Delta F/F_0$ imaging of electrical heart activity was performed processing raw data: for each frame, the mean baseline was first subtracted and then the frame was normalized to the mean baseline yielding a percentage change in fluorescence over time; next, a binning operation was

performed on $4 \times 4 \times 4$ pixels areas to reduce noise, generating thus activation maps with a spatial resolution of $4 \times 78 \mu\text{m} = 312 \mu\text{m}$. CV was calculated using the activation maps, by performing a threshold operation (pixel intensity $> 50\%$ maximum) on the cross-correlation data sets and replacing the active pixels with a time stamp. Sequential frames were collapsed into one frame where each pixel corresponds to the delay time of activation with respect to a user-defined start time. Since for each pixel the local direction of AP wave-front is represented by a vector, we evaluated wave-front dispersion as the standard deviation of angles of propagation vectors. For AP kinetics analysis, average values of time-to-peak (TTP) and APD were calculated from the TTP and APD maps respectively. In detail, for each pixel of the maps, a value of TTP and APD was assigned and an average across pixels was performed. TTP was calculated by dividing AP amplitude (%) by the upstroke velocity (%/ms). APD was calculated at 50% repolarization (APD50) and at 90% repolarization (APD90). Moreover, we also assessed the dispersion of TTP and APD across the heart by using the standard deviation of average across pixels values.

During cardiac arrhythmias induction protocol, we investigated: number of arrhythmia events per second (with a duration of at least 250 ms), duration of each event (in milliseconds, ms), and cycle length of arrhythmia episode expressed as frequency (Hertz, Hz) evaluated from the ECG.

3.4 Whole heart clearing

3.4.1 Tissue clearing method

After the optical mapping recording, the hearts have been subjected to the SHIELD protocol (Figure 18), slightly modified for its application on the cardiac tissue. The hearts have been perfused with 24 mL of a fixative solution containing 4% of paraformaldehyde (PFA) in PBS (pH 7.6) and

incubated in 30 mL of PFA 4% in PBS overnight (O/N) at 4°C; the following day they have been washed in PBS 3 times for 1h at 4°C. Then, the hearts have been incubated in 20 mL of SHIELD-OFF solution (25% of ddH₂O, 25% of LifeCanvas Technologies SHIELD Buffer solution, 50% of LifeCanvas Technologies SHIELD Epoxy solution) at 4°C in shaking for 6 days. The following day they have been incubated in 20 mL of LifeCanvas Technologies SHIELD-ON solution at 37°C in shaking for 24 hours. Then, the hearts have been incubated in SHIELD clearing solution (Sodium Dodecyl Sulfate 300 mM, Boric acid 10 mM, Sodium sulfite 100 mM; pH 9) at 37°C in shaking up to the achievement of good transparency (between 6 and 8 months). Finally, the hearts have been incubated in 10 mL of the RI matching solution (EasyIndex, LifeCanvas Technologies) at room temperature for 2 days.

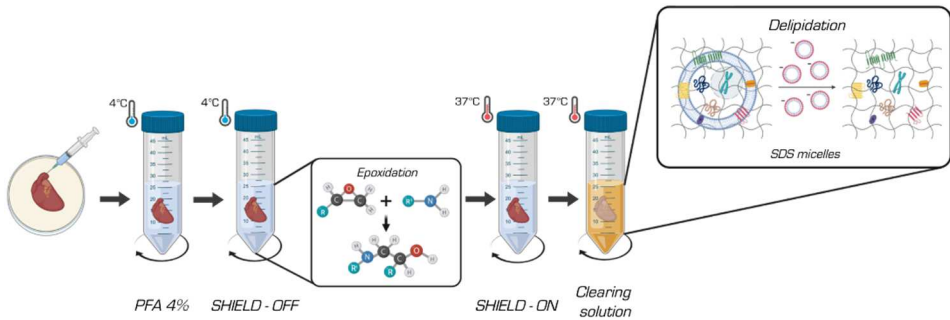


Figure 18: Scheme of the SHIELD protocol. Schematic representation of the optimized SHIELD protocol for the clearing of entire hearts. Insert panels elucidate the chemical processes underlying the most fundamental steps of the protocol: after the hearts have been fixed in PFA 4%, they have been incubated in the poly-epoxides solution (SHIELD-OFF) for 6 days at 4°C, then in a buffer solution (SHIELD-ON) for 1 day at 37°C and finally in the clearing solution at 37°C up to the achievement of the proper level of transparency. Image modified from (56).

3.4.2 Histological analysis on clarified tissue

Transverse sections were made in the plane of the minor axis of the cardiac specimens, from the middle portion of the ventricle to the apical level. The specimens were fixed by incubation in 10% neutral buffered formalin at 4°C

overnight and subjected to routine treatment and paraffin embedding. Serial sections (4 μm thick) were stained with haematoxylin-eosin or Masson's trichrome staining. Images were taken and acquired using the Leica DMD108 digital microscope.

3.5 Whole heart reconstruction

3.5.1 MesoSPIM setup

The system used for mesoscopic reconstructions of clarified samples is a custom-developed MesoSPIM microscope (66). All the microscope components are automatically controlled by a dedicated software developed in LabView 2012 (National Instruments, version 12.0f3 at 32 bit). The optical scheme of the microscope is shown in Figure 19.

The main parts of the MesoSPIM setup consist of two excitation arms, a detection system, and a sample mounting system (Figure 20). Each of the excitation arms (Figure 20: 2) consists of a laser combiner (Oxxius, L4CC-CSB-1311) operating at 638nm, that is collimated on the tunable lens (ETL in Figure 19) able of translating the light-sheet waist along the X-axis of the FOV; a high-frequency galvanometric mirror (Scan mirror in Figure 19) that generates the light-sheet on the XY plane by sweeping the light beam along the Y axis; and finally the excitation lens (L5 in Figure 19), that focus the excitation beam inside the sample.

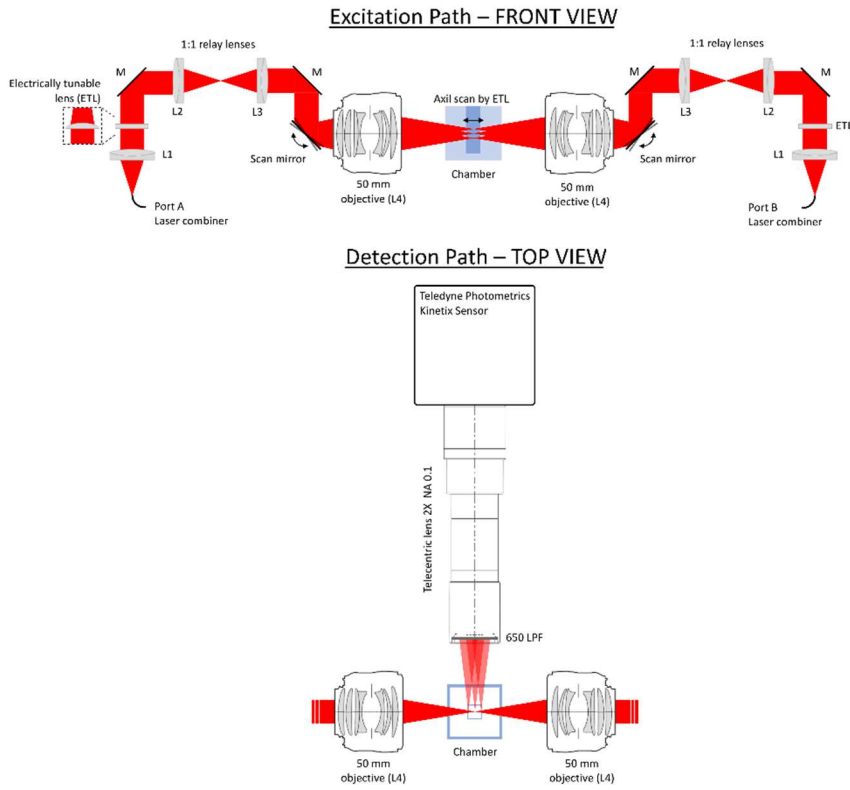


Figure 19: MesoSPIM optical scheme. L1: Achromatic doublets (AC254-050-A-ML, Thorlabs), ETL: Electrically Tuneable Lens (EL-16-40-TC-VIS-5D-1-C, Optotune), M: Dielectric Mirror (BBE1-E02, Thorlabs), L2 and L3: Achromatic doublets (G063200000, Qioptiq), Scanning mirror (GVS211/M, Thorlabs), L5: Camera objective (Nikkor AF-S 50mm f/1.4G, Niko), 650 LPF: Long-pass filter (ET655lp, Chroma).

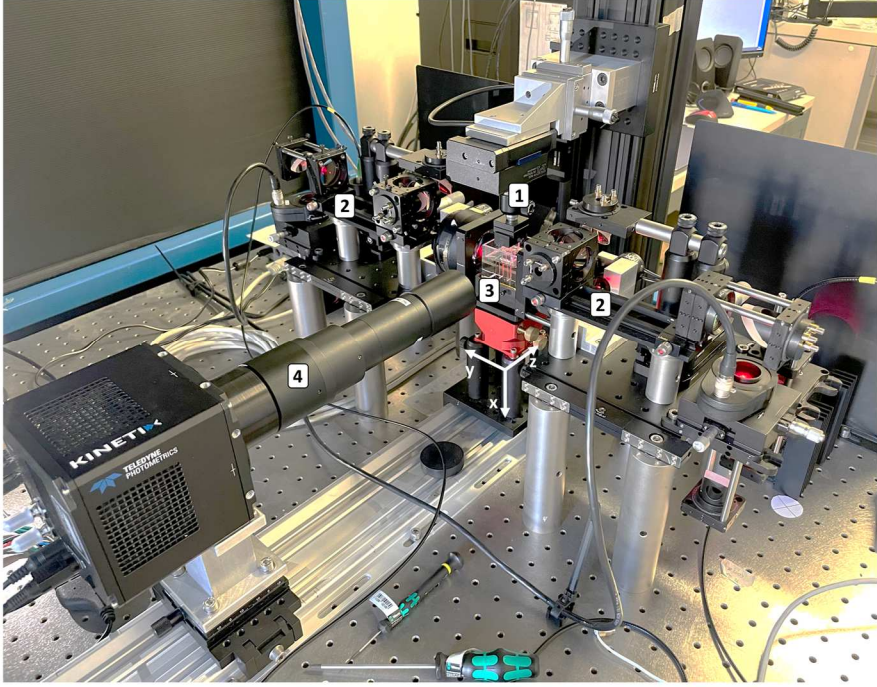


Figure 20: MesoSPIM setup. Numbers indicate the main components: 1) holder for positioning the sample, inserted into the inner cuvette; 2) excitation arms; 3) outer cuvette; 4) detection optics. The reference system is reported in white (XY: image plane; Z: optical axis).

The detection system (Figure 20: 4) is instead equipped with a 2x telecentric lens (Lenstation, Telecentric Lens TM42-10M-20-75) and a high-performance back-illuminated sCMOS sensor (Kinetix Scientific CMOS Camera, Teledyne Photometrics) allowing a FOV of approximately 1.04 cm with a pixel size of 3.25 μm , sufficient to acquire an entire murine heart with a negligible field-curvature distortion (Figure 21).

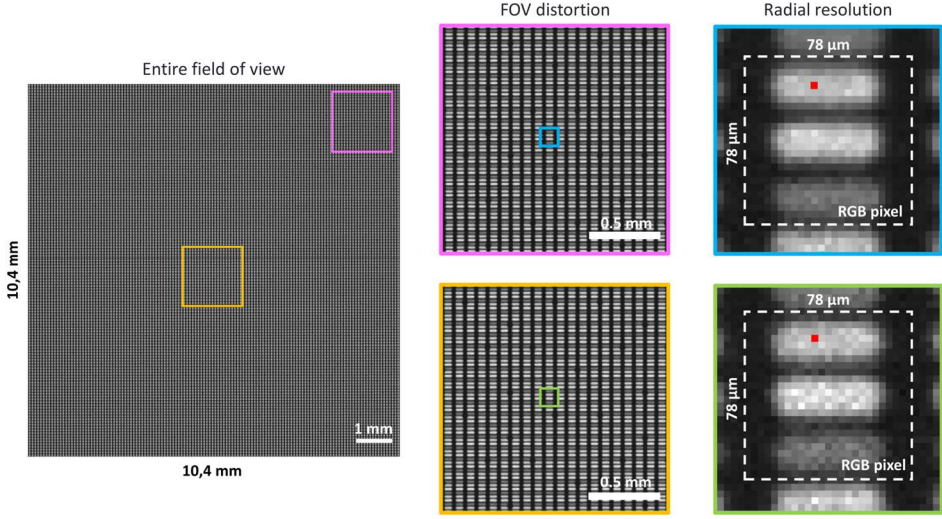


Figure 21: Performance of detection path. Qualitative investigation of radial resolution and field distortion of the MesoSPIM detection path (camera: Kinetix Scientific CMOS Camera, Teledyne Photometrics; telecentric lens (Lensation, TM42-10M-20-75); magnification: $2\times$) while imaging an RGB display. Blue and green inserts show a single RGB pixel imaged with 24×24 pixels; small red square highlights a single pixel of the Kinetix sensor (pixel size $3.25 \mu\text{m}$).

Each of the two excitation arms generates a sheet of light that illuminates only the half of the sample closest to it. To acquire an image plane inside the sample, the system initially generates a sheet of light from the right arm, and shifts the focus along the X-axis; once the central part of the FOV is reached, the right laser is switched off, and simultaneously the left arm is switched on, programmed to translate the focus from the center of the FOV to the left end. The camera's rolling shutter, 64 lines wide (about $208 \mu\text{m}$), is synchronized with the sliding of the focus, which takes 520ms to travel through the entire FOV, in order to acquire always the waist of the light-sheet (Figure 22). This mechanism makes it possible to resolve an entire image plane by halving the light path inside the sample; this further reduces the degradation of the light sheet due to light scattering, which is already drastically reduced by the homogenization of the RI during the tissue clearing protocol.

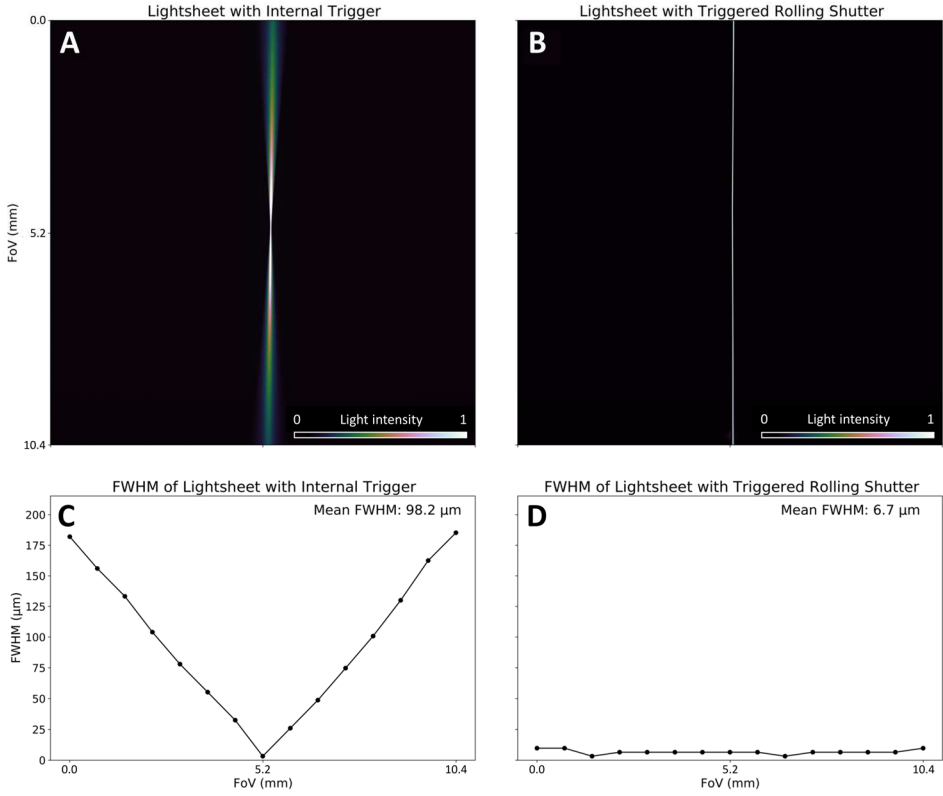


Figure 22: MesoSPIM light-sheet generation. (A, B) Excitation light-sheet focused statically into the centre of Field of View (A) and generated dynamically by the synchronization between the camera rolling shutter (operating at 1.92 Hz) and the scanning light-beam driven by the tunable lens (B). Pixel size: 3.25 μm ; exposure time: 10 ms; light source: 638 nm; light intensity is normalized and reported with a colormap. The Full Width Half Maximum (FWHM) of the light intensity profile is evaluated in 15 different positions along the FoV of pane A and B; results and averages are shown in panel C and D respectively.

During the acquisitions, the sample is placed in a quartz cuvette (Portmann Instruments, UQ-20°). The cuvette is mounted using magnets on the support (Figure 20: 1) equipped with two manual translators (Physik Instrument) mounted for translations along the X and Y axes, a motorized translator for movements along the Z-axis (Physik Instrument, M-122.2DD), and a rotational translator (Physik Instrument, M-116.DG), useful to rotate the sample around the Y-axis. The whole block can be shifted downwards to

immerse the inner cuvette in a second larger quartz cuvette (Figure 20: 3), filled with any solution that provides the same RI ($n=1.46$) as the quartz and the RI matching solution (EasyIndex, LifeCanvas). During this work, the TDE solution was used.

3.5.2 Acquisition protocol

To reduce the effect of light scattering within the sample, each heart was immersed in EasyIndex 2-3 days before the acquisition, to ensure optimal RI homogenization between the solution and the inner part of the tissues. After this time, the sample (which, once immersed in EasyIndex, would tend to float) is glued to a metal support using a commercial glue (Super Attak Precision, Loctite), placing at the base of the heart in contact with the support to not damage the ventricular tissue. Assembled in this way the sample is then placed in the inner quartz cuvette, previously filled with EasyIndex, which is subsequently immersed in the outer quartz cuvette, filled instead with TDE, having the same RI.

Tomographic reconstructions were obtained by moving the sample along the Z-axis at a constant speed of $6\text{ }\mu\text{m/s}$ thanks to the motorized translator. This mechanism, coupled with an image plane acquisition frequency of 2 Hz , guarantees a Z sampling of about $3.0\text{ }\mu\text{m}$. The tomographic reconstruction will therefore have voxel sizes of $3.25\text{ }\mu\text{m} \times 3.25\text{ }\mu\text{m} \times 3.0\text{ }\mu\text{m}$ in XYZ, respectively.

Since the light scattering problem involves not only the excitation source but also the emitted fluorescence, at the end of each tomography the motorized translation system moves the sample along the Z-axis to its starting position; then, the rotational motor rotates the sample around the heart main axis by $+90^\circ$, and the tomography is repeated, in the same manner, for a total of four acquisitions: 0° , 90° , 180° , and 270° of the sample (Figure 23, panel A).

The imaging mechanism just described is carried out in the same way to acquire the autofluorescence and scattering signals. Operationally, the

sample is illuminated with a power of 1 mW to perform tomographic reconstructions of the scattering signal, collected by the camera without the use of any optical filter. Once all the four tomographies (0°, 90°, 180°, and 270°) has been performed, the long-pass filter is mounted to collect only the autofluorescence contribution, and the sample is then illuminated with a power of 30 mW. The acquisition of the whole sample is repeated without moving the sample inside the cuvette, to ensure that the two signals are perfectly superposable.

For each sample, a total of eight partial tomographies were then generated, performed with the sample placed at 0°, 90°, 180°, and 270° around the long heart axis, four containing the autofluorescence signal and four the scattering signal, all quantized with 16 bit and with a voxel size of $3.25 \times 3.25 \times 3.0$ μm in XYZ.

3.5.3 Images pre-processing

First, the best couple *front/back* (0°/180° or 90°/270°) was selected by a qualitative check on the image. The selected 3d images were downscaled to an isotropic voxel size of $6 \times 6 \times 6$ μm and converted from 16 to 8 bit. This step reduced the data dimension (from about 40 GB to about 3.5 GB for each single-channel partial tomography) and intrinsically performed a 3d blurring operation that remove signal noise. This step is performed with ImageJ software (<https://imagej.net/software/fiji/>) (67), using the FIJI distribution (68).

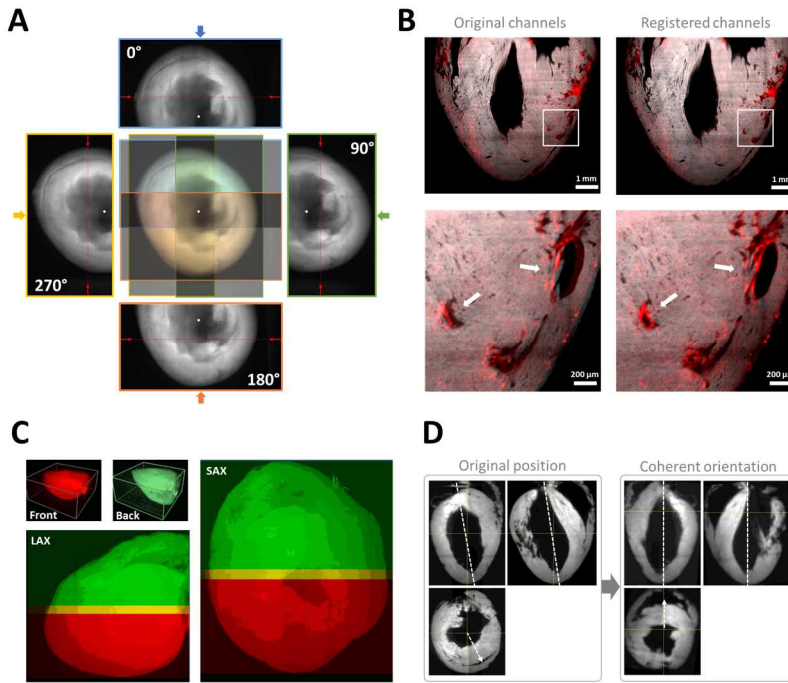


Figure 23 : Sample imaging and image preprocessing. (A) Scheme of multiple acquisitions performed to reconstruct an entire cleared mouse heart with the MesoSPIM setup. Partial tomography was performed for each rotation of the organ around its long axis (white spots superimposed on Short-Axis Average-Intensity-Projections) at 0°, 90°, 180°, and 270° degree (blue, green, orange and yellow arrows indicate the optical axis). Red lines represent the optical sectioning plane of the light-sheet generated by a light source at 638 nm from two parallel excitation arms (red arrows). In the center, the sample shape is reassembled by merging the four views as an example. (B) Result of the 3d channel registration process performed on a representative mouse heart reconstruction (muscle autofluorescence in grey, scattering light in red) with the plugin FijiYama (ImageJ) to correct the spatial shift (white arrows) caused by the optical aberration introduced by the long pass filter used to collect the autofluorescence signal. (C) Registration of two opposite partial tomographies (front and back) of a MesoSPIM mouse heart reconstruction using Huygens Professional (SVI). After the initial manual registration, the software optimizes the alignment and fuse the three-dimensional images. (D) Representative example of manual three-dimensional realignment performed on all mouse hearts reconstructions. The sample is rotated iteratively on each view of the 3d tomography to re-align the long axis of the organ and place the right ventricle on top of the SAX view.

Later, for each *half-heart* reconstruction (front and back), a three-dimensional co-registration was performed to realign autofluorescence and scattering signals. In fact, the remotion of the high-pass filter shifts the focus

plane position on the optical axis, producing a little – but not ignorable – shift between the autofluorescence and the scattering signal (Figure 23, panel B). The fine-tuned alignment of the two channels is performed using the FijiYama (69, 70) plug-in available in the ImageJ ecosystem.

Later, the two half-heart tomographies were merged exploiting the professional software Huygens Professional version 19.04 (Scientific Volume Imaging, The Netherlands, <http://svi.nl>). The software allowed the user to manually re-align the two portions of the sample (Figure 23, panel C), and then it refined the alignment by a multi-scale registration before merging the images optimizing the final output.

Entire-heart reconstructions were then manually realigned coherently with the reference system defined in the *Standardized Myocardial Segmentation and Nomenclature for Tomographic Imaging of the Heart* (71) of the American Heart Association (AHA). In our data, it means that from the Long Axis (LAX) view, i.e. the frontal view (XY plane or *sagittal* plane) and the Four Chamber (4C) view, i.e. the side view (YZ plane or *coronal* plane), the main heart axis has been made parallel to the Y-axis; by the Short Axis (SAX) view, i.e. the transverse view (XZ plane or *transversal* plane), right-ventricle (RV) and LV were placed on top and bottom respect to the XZ plane respectively (Figure 23, panel D).

Realigned two-channel entire-heart tomographies with a voxel size of 6 μm were defined as *high-resolution (HR) tomographies*. Later, *low-resolution (LR) tomographies* were generated by downscaling the HR data to a voxel size of $78 \times 78 \times 78 \mu\text{m}$, which is comparable with the functional imaging dataset. Realignment and low-resolution tomographies generation was performed with ImageJ software.

3.6 Image analysis

This section describes the image analysis pipeline performed on MesoSPIM reconstructions. Image segmentations based on intensity thresholding and manual measurements of myocardium anatomy were performed using ImageJ software (<https://imagej.net/software/fiji/>) under the FIJI distribution (67, 68). All the other image-processing steps were performed automatically by software tools developed ad-hoc in Python 3.6.8. Main Python3 libraries involved were: NumPy 1.17.3 (72), SciPy 1.3.1 (73), and Scikit-learn 0.16.2 (74) for numeric elaboration, Scikit-image 0.16.2 (75), OpenCV-python 3.2.0.8 (76), Tiffle 2019.7.26 and Pillow 6.2.1 for image processing.

3.6.1 Myocardium anatomy and fibrosis quantification

3.6.1.1 *Myocardium segmentation and anatomical measurements*

For each sample, the three-dimensional anatomy of the myocardium was segmented by thresholding the autofluorescence signal of LR tomographies. The total volume of the myocardium was automatically calculated for each sample by counting the voxels of the segmentation and multiplying the result for the volume of a single voxel in mm^3 , i.e. $0.078 \text{ mm} \times 0.078 \text{ mm} \times 0.078 \text{ mm} = 0,474552 \cdot 10^{-3} \text{ mm}^3$. Similarly, the volume of the LV chamber is automatically calculated by the software by extracting the LV chamber area from the myocardium segmentation.

Anatomical measurements of the LV wall thickness were based on the AHA's *Standardized Myocardial Segmentation and Nomenclature for Tomographic Imaging of the Heart* to define, orient, and display the heart using the LAX view of the LV. To select the right frames to be used for wall thickness measurement, we exploited the Horizontal LAX view of each LR tomography, showing on the upper side the RV cavity, and on the lower side

the LV cavity. The LV was then divided into equal segments perpendicular to the long axis of the heart: Apical (from the apical limit of the ventricular chamber to the beginning of the papillary muscles), Mid-Cavity (the central part of the cavity, which includes papillary muscles), and Basal (up to the orifice of the mitral valve). For the anatomical measurement of the ventricle wall, the central frame of each of these segments was selected and its SAX was displayed. Always on ImageJ, the Basal and Mid-Cavity segments were measured with 6 lines each (B1, B2, B3, B4, B5, B6 and M1, M2, M3, M4, M5, M6 respectively) 60 degrees apart, and the Apical segment with 4 lines (A1, A2, A3, A4), 90 degrees apart.

3.6.1.2 *Fibrosis quantification*

Patches of fibrotic tissue were reconstructed inside our tomographies exploiting scattering signal images. In detail, first, SAX views of HR tomographies were compared with the Masson's Trichrome staining of the same samples; later, a threshold $T=8$ was defined on the grey levels of scattering channel to discard the background accordingly with the histological images. finally, the scattering channel was equalized between 8 and 255 ldg to represent fibrotic tissue in both HR and LR tomographies.

Low-resolution tomographies were exploited to calculate the volume of fibrotic patches. Briefly, fibrosis was segmented by collecting all pixels of the scattering channel with an intensity greater than $T=8$. Later, segmentation was manually corrected to remove elements not correlated with cardiac tissue as little air bubbles or glue residuals; finally, the amount of fibrotic tissue was calculated by counting the voxels composing the fibrosis segmentation and multiplying the result for the volume of a single voxel in mm^3 .

The percentage of fibrotic tissue inside each sample was evaluated as:

$$PF = \frac{FV}{(MV + FV)} \%$$

with *PF*: Percentage of Fibrosis, *FV*: Fibrotic tissue volume; *MV*: myocardium volume.

3.6.2 Orientation fibers reconstruction and analysis

3.6.2.1 Fiber orientation through Structure Tensor Analysis

To virtually reconstruct the three-dimensional orientation of the contractile fibers of the entire myocardium, we involved the autofluorescence signal of the cardiac tissue in a Structure Tensor Analysis (STA) (77, 78). We used the myocardium segmentations already performed during the anatomical investigation to mask the myocardium tissue in the HR images obtained after the pre-processing operations. Images have a resolution sufficient to detect the local orientation of each contractile fiber bundle, i.e. in the order of tens of micrometers. Simplifying a single mouse cardiomyocyte as a cylinder with 100 μm long and 20 μm width, and considering the voxel size of our 3d images of 6 $\mu\text{m} \times 6 \mu\text{m} \times 6 \mu\text{m}$, we reconstructed the fiber orientation in sub-volumes (chunks ***p***) of $16 \times 16 \times 16$ pixels, resulting in a spatial resolution of 96 $\mu\text{m} \times 96 \mu\text{m} \times 96 \mu\text{m}$, i.e. theoretically containing at least 4×4 cells packed together.

Operatively, the analysis software virtually dissected each whole-heart autofluorescence reconstruction in chunks ***p*** and detect the three-dimensional average orientation inside ***p*** exploiting the local gradient of the autofluorescence signal, i.e. the mean direction of the muscle fibers.

In detail, each chunk ***p*** with a percentage of voxels labeled as *tissue* (i.e., not zero) greater than 95% was automatically labeled as *accepted* and analyzed. This step exclude the background and borders of the tissue during the composition of the fiber orientation map.

For each accepted ***p***, local (voxel-size) image gradient-structure tensors $S(x, y, z)$ were first computed as:

$$S(x, y, z) = \nabla I \nabla I^T * g_{\sigma_s} = \begin{pmatrix} I_x^2 * g_x & I_x I_y * g_y & I_x I_z * g_z \\ I_y I_x * g_x & I_y^2 * g_y & I_y I_z * g_z \\ I_z I_x * g_x & I_z I_y * g_y & I_z^2 * g_z \end{pmatrix}$$

where the first-order spatial derivatives I_x , I_y , and I_z were estimated using second-order accurate central differences, whereas g_x , g_y and g_z represent Gaussian smoothing filters with a standard deviation $\sigma_s = 1 \text{ pixel} = 6 \mu\text{m}$.

Local $S(x, y, z)$ elements were then averaged to extract the mean 3d tensor \bar{S} and the spectral decomposition reported below was performed:

$$\bar{S} = \begin{pmatrix} \bar{S}_{xx} & \bar{S}_{yx} & \bar{S}_{zx} \\ \bar{S}_{yx} & \bar{S}_{yy} & \bar{S}_{zy} \\ \bar{S}_{zx} & \bar{S}_{yz} & \bar{S}_{zz} \end{pmatrix} = \begin{pmatrix} | & | & | \\ v_1 & v_2 & v_3 \\ | & | & | \end{pmatrix} \begin{pmatrix} \lambda_1 & 0 & 0 \\ 0 & \lambda_2 & 0 \\ 0 & 0 & \lambda_3 \end{pmatrix} \begin{pmatrix} | & | & | \\ v_1 & v_2 & v_3 \\ | & | & | \end{pmatrix}^{-1}$$

(e-vectors) (e-values)

Eigenvalues λ_i, λ_j , and λ_k were involved to estimate the local Fractional Anisotropy (FA), defined as below:

$$FA = \sqrt{\frac{1}{2} \cdot \frac{\sqrt{(\lambda_i - \lambda_j)^2 + (\lambda_j - \lambda_k)^2 + (\lambda_i - \lambda_k)^2}}{\sqrt{\lambda_i^2 + \lambda_j^2 + \lambda_k^2}}}$$

Fractional anisotropy is a scalar value between zero and one that describes the degree of anisotropy of a diffusion process (79, 80). In our images, FA can be used to estimate the anisotropy of the autofluorescence signal, i.e. a degree of its directionality. Lower FA values correspond to image portions presenting a confused content without a predominant signal direction, and they have to be discarded during the reconstruction of the fibers muscle. We set a threshold on the FA values to include in the orientation map only \mathbf{p} with $FA > 0.25$; these \mathbf{p} were labeled as *reliable*.

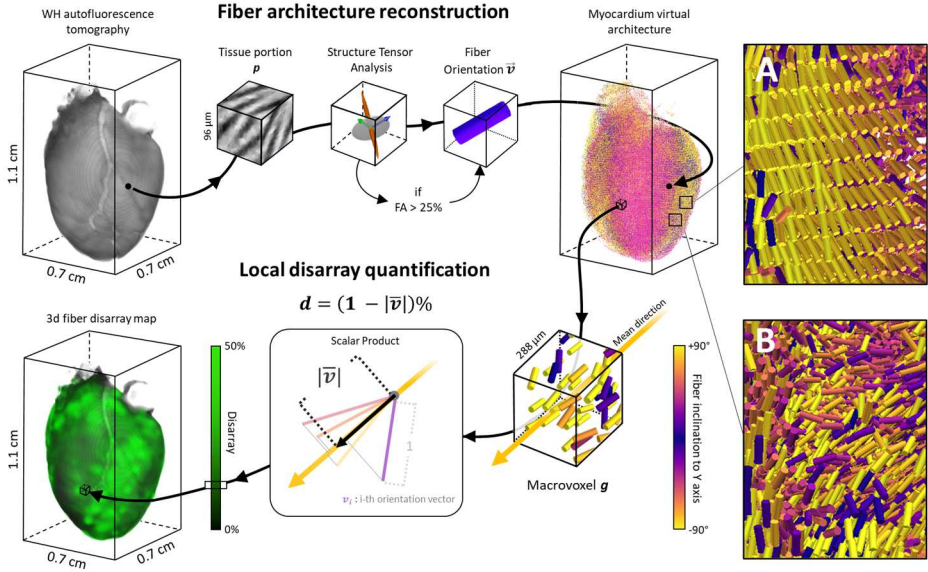


Figure 24: Three-dimensional fiber disarray quantification in entire mouse heart reconstruction. Scheme of the automatic image software analysis developed to map conduction fibers and quantify their disarray in whole-heart (WH) reconstructions of CTRL and DSG2 mouse hearts. The software exploits cardiac muscle autofluorescence signal contained in three-dimensional tomographies to detect 3d fiber orientation in tissue portions p of $96 \mu\text{m} \times 96 \mu\text{m} \times 96 \mu\text{m}$ with the Structure Tensor Analysis (STA) and re-builds the virtual muscle architecture of the entire heart. This orientation map is virtually dissected in macro-voxels of $288 \mu\text{m} \times 288 \mu\text{m} \times 288 \mu\text{m}$; there, local fiber disarray is evaluated by the scalar product between orientation vectors and the local average fiber direction, and the result is mapped in green over each voxel of the original tomography. (A, B) Two representative areas of the virtual myocardium reconstruction show high ordered (A) and disordered (B) muscle fibers.

For each reliable p , an eigenvalues analysis was conducted for identifying the eigenvectors $v_i \in \mathbf{R}^3$ associated with the lowest eigenvalue $\lambda_i \mid \lambda_i < \lambda_j < \lambda_k$ (where $i, j, k \in [1, 2, 3]$ are 3d image axes), thus indicating the direction carrying the lowest gradient variability, i.e. the principal direction of the biological structure present in the analyzed tissue chunk. The selected eigenvector was normalized and defined as *orientation vector* \vec{v} .

The automatic software iterated the presented STA-based orientation analysis on each portion p of the segmented myocardium tomography and

build the 3d virtual architecture of the entire cardiac muscle by reallocating each orientation vector \vec{v} in the original position of its correspondent \mathbf{p} . This vector space reassembles the fiber architecture of the whole sample. A scheme of the proposed analysis pipeline is shown in Figure 24.

3.6.2.2 Fibers Disarray Quantification

The virtual muscle architecture was analyzed to estimate local fiber disarray (81), defined as the misalignment degree of nearby orientation vectors to respect to the mean local direction. We set a spatial resolution of fiber disarray analysis of $288 \times 288 \times 288 \mu\text{m}$, thus dissecting the vector map in macrovoxels \mathbf{g} each including $3 \times 3 \times 3$ orientation vectors. A macrovoxel is labeled as *valid* if it contains at least 50% of *reliable* orientation vectors \vec{v} . For each valid \mathbf{g} , local disarray was evaluated exploiting the scalar product between valid orientation vectors contained in \mathbf{g} as explained below:

- the N valid vectors $\vec{v}_1, \dots, \vec{v}_N \in \mathbf{g}$ (with $\frac{3^3}{2} < N \leq 3^3$) are ordered to have decrescent FA values: $FA_1 > FA_2 > \dots > FA_N$;
- vectors $\vec{v}_2, \dots, \vec{v}_N$ are turned in the same *verse* of \vec{v}_1 (the vector with the highest FA, i.e. the strongest directionality) to avoid to average opposite vectors;
- the average vector $\overline{\mathbf{v}}_{\mathbf{g}}$ was estimated by a weighted mean of $\vec{v}_1, \dots, \vec{v}_N$ with their FA values:

$$\overline{\mathbf{v}}_{\mathbf{g}} = \frac{\sum_1^N F_i \cdot \vec{v}_i}{\sum_1^N F_i}$$

where $\overline{\mathbf{v}}_{\mathbf{g}} \in \mathbf{R}^3$ coincides with the average direction of the fibers inside \mathbf{g} ;

- finally, we defined *local disarray* as:

$$\mathbf{d_g} = (1 - |\overline{v_g}|)\%.$$

where, in the case of purely random orientations, we expected a zero value of $|\overline{v_g}| = 0$, while a perfect arrangement of all orientation vectors provides $|\overline{v_g}| = 1$, i.e. $\mathbf{d_g} = 100\%$ and $\mathbf{d_g} = 0\%$ respectively.

By evaluating $\mathbf{d_g}$ values across the entire myocardium fiber reconstruction, the software created a three-dimensional disarray map with a voxel size defined by the spatial resolution involved: $288 \times 288 \times 288 \mu\text{m}$.

To directly visualize the fibers disarray on the three-dimensional tomography of each sample, the 3d disarray map was first interpolated to a voxel size of $78 \times 78 \times 78 \mu\text{m}$ and then dual-channel LR tomographies were generated by representing autofluorescence signal in grey and fibers disarray in green. To enhance the visualization, in the figures the disarray channel was often equalized between 0 and 50%.

3.6.3 Fibrosis and fiber disarray spatial distribution

Spatial distribution around the LV chamber of fibrosis and local disarray was performed analyzing LR tomographies with a custom analysis tool developed in Python 3.8. The software is designed to exploit the myocardium segmentation as a reference and to analyze the spatial distribution of any other channel containing structural information to map the result on a two-dimensional model of the SAX view. The main steps are explained below.

First, the sample was automatically centered into the virtual volume that included it by evaluating the center of mass of the autofluorescence signal (i.e., the barycenter of the myocardium) and shifting the data accordingly (Figure 25, panel A).

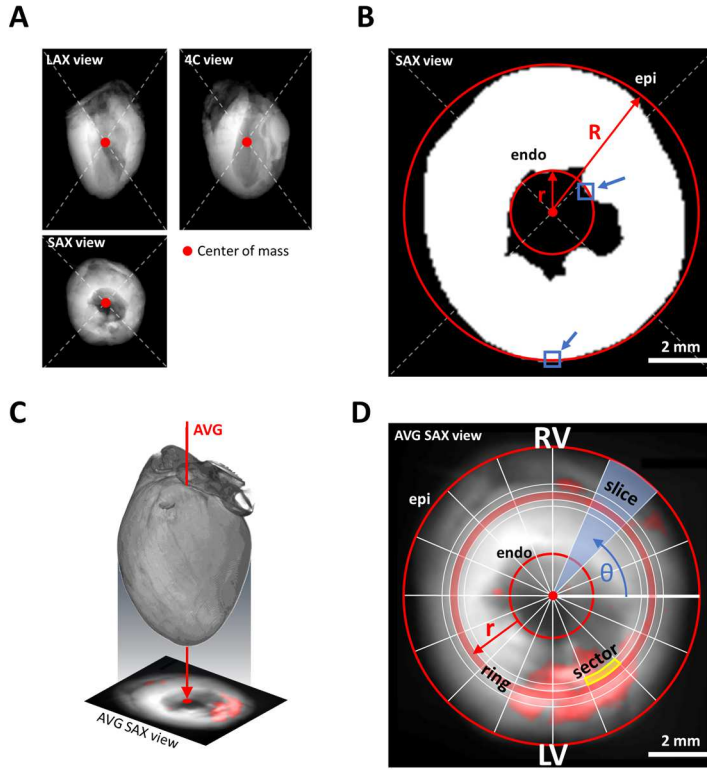


Figure 25: Automatic spatial quantization of 3d data around LV wall. Representative schemes of the main steps of the automatic quantization software developed to analyze the spatial distribution of fibrosis and fiber disarray around the left ventricle wall in low-resolution (LR) reconstructions of mouse hearts. (A) The myocardium is centered in the 3d volume by evaluating the barycenter of the autofluorescence signal. (B) The radii of circles that fit endocardium (r) and epicardium (R) surfaces are estimated matching smaller and bigger circumference touching a pixel (blue arrows) of the myocardium segmentation in the central SAX view. (C) All channels of the 3d tomography were averaged long the main axis of the hearts, generating an average SAX (AVG SAX) view. (D) Angular and radial quantizations of the AVG SAX view are performed with sixteen incremental angles and radius respectively. The sum of the signal inside each sector is stored in a normalized LV map.

Later, the central SAX plane of the segmentation was extracted to automatically detect the endo- and epicardium surfaces: pixels placed on circles with incremental radius were collected; the smaller and bigger circles with any not-zero voxels are found; the correspondent radii (r and R) was defined the position of endo- and epicardium surfaces respectively (Figure

25, panel B). This will represent the normalized shape of the SAX section where map the result of the spatial quantization.

The content of the channel that has to be investigated (red for fibrosis, green for disarray) was averaged along the Y-axis (the long axis of the heart) creating a two-dimensional 8-bit average SAX view (Figure 25, panel C), where the spatial quantization will be performed. Specifically, a radial (and angular) quantization was performed by splitting the image into sixteen circles (slices) with incremental radius (angle) (Figure 25, panel D). Finally, the combination of rings and slices created a grid used to quantize the signal: for each “sector”, the image is segmented and pixel values are sum, thus generating a map of the signal content around the LV.

Average maps were generated to confront two groups of samples. First, epi and endocardium circles were fit as:

$$\bar{r} = \frac{\sum_i r_i}{n} \quad ; \quad \bar{R} = \frac{\sum_i R_i}{n}$$

Where n is the number of samples to average; later, each sample’s map was normalized between \bar{r} and \bar{R} ; final, sectors of normalized maps are averaged.

3.7 Alignment of LV fibrosis maps with optical mapping images

Three-dimensional tomographies containing structural information have been correlated with two-dimensional maps of the propagation of the AP on the LV surfaces of mouse hearts. To this aim, the autofluorescence signal of LR tomographies was exploited to realign the tomography to the original position of the Langerdoff-perfused heart during the optical mapping protocol.

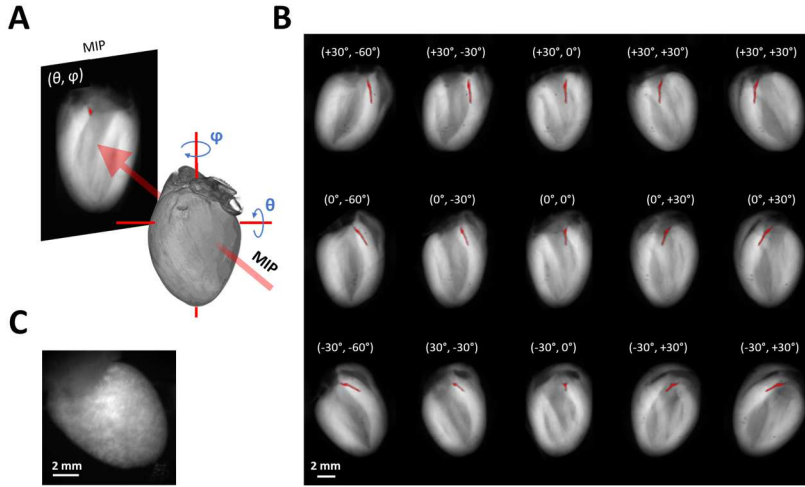


Figure 26: Automatic rotation of mouse heart tomographies for morpho-functional maps correlation. (A) Scheme of the automatic software tool used to create Maximum Intensity Projections (MIP) of whole mouse heart tomography previously fine-rotated around the long axis (with θ) and transversal axis (with ϕ). (B) Representative example of MIPs of a mouse heart tomography containing autofluorescence (grey) and scattering signal (red) for each couple of rotations (θ, ϕ) at -60° , -30° , 0° , 30° , and 60° . In the figure, the scattering signal related to the big vessel is used as a reference. (C) Representative example of a fluorescent signal image of a Langerdoff-perfused mouse heart during the optical mapping protocol.

First, a series of rotations around the long and transversal heart axes were automatically performed to LR tomography and, after each rotation, a Maximum Intensity Projection (MIP) was generated to extract the outer shape of the organ (Figure 26, panel A). Panel B of Figure 26 shows a representative example of a serie of MIPs generated with a CTRL mouse heart reconstruction. For each sample, MIPs are generated and visually compared with the fluorescent images of the same heart collected during the optical mapping protocol (panel C). The rotation of the MIP that best match the shape of the fluorescent image is used to create a new MIP including autofluorescence and scattering signal: the LR tomography was rotated, the half of the organ visible during the optical mapping was extracted, and the MIP of the resulting “half-heart” is finally generated. This mechanism

allowed us to generate two-dimensional fibrosis maps including the entire thickness of the unique cardiac wall exposed to the optical mapping.

3.8 Data visualization and statistical analysis

3.8.1 Statistical analysis

Statistical analyses were performed with were performed using OriginPro 2018, version 9.5 64-bit (OriginLab Corporation), and Python3 packages NumPy 1.17.3 (72), SciPy 1.3.1 (73), and Pandas 0.25.3 (82, 83).

Statistical analyses were performed with various statistical methods, depending on the data set. To assess the influence of two factors (categorical independent variables) on a continuous outcome variable (dependent variable), the two-way analysis of variance (ANOVA) was used. For the comparison of the mean, the significance level was set at 0.05, and Tukey's test was used. The Coefficient of Variation (CV) was calculated as the ratio between the standard deviation and the mean. On the other hand, to compare two experimental groups, the unpaired Student's t-test was used. A p-value of < 0.05 is considered as indicative of a statistically significant difference between means (NS: $p > 0.05$; * $p < 0.05$; ** $p < 0.01$, *** $p < 0.001$, **** $p < 0.0001$). Normality test on distributions was performed applying the D'Agostino-Pearson normal test (84, 85).

3.8.2 Data visualization

Graphical representations of numerical data were generated using OriginPro 2018, version 9.5 64-bit (OriginLab Corporation), and Python3 package Seaborn 0.9.0 (86). Two- and three-dimensional vectors fields

representations were generated with packages Matplotlib (87, 88) and Mayavi 4.7.1 (89) packages respectively. All microscopy images were equalized, processed and plot with ImageJ (67), using the FIJI distribution (<https://imagej.net/software/fiji/>) (68). Three-dimensional renderings were generated with the plugin *3d viewer* (90) included in the software FIJI.

4 Results

4.1 Functional data

4.1.1 Optical mapping of cardiac electrical activity

The optical platform described before was used to optically map the AP propagation in horizontally positioned Langendorff perfused mouse hearts stained with a red-shifted VSD. To overdrive the SR (5.2 ± 0.1 Hz at 7 months age and 4.7 ± 0.2 Hz at 13 months age in CTRL mice; 5.5 ± 0.2 Hz at 7 months age and 5.4 ± 0.2 Hz at 13 months age in DSG2 mice), CTRL and DSG2 mouse hearts were electrically paced at the apex with a burst of 15 stimuli at 5, 6, and 8 Hz (Figure 27, panel A).

Representative AP voltage traces (Figure 27, panel B) recorded at a pacing rate of 5 Hz, clearly show delayed depolarization and increased repolarization time in DSG2 as compared to CTRL. Indeed, a significant increase in TTP was observed in DSG2 hearts at all stimulation frequencies at age 13 months, which was markedly present at a pacing rate of 5 Hz. Additionally, variation of depolarization time across the heart, measured by TTP dispersion, was significant increased DSG2 mice at age 13 months and at all stimulation frequency. In contrast, no TTP variations were found at age 7 months at any pacing rates (Figure 27, panels C, D). A tendency to altered repolarization characteristics was also observed in DSG2 mouse hearts, with AP prolongation (both APD50 and APD90) at age 7 and 13 months and at all stimulation frequencies, although these differences were not statistically significant (Figure 27, panels E, F). However, no differences in APD dispersion were observed between DSG2 and CTRL mouse hearts.

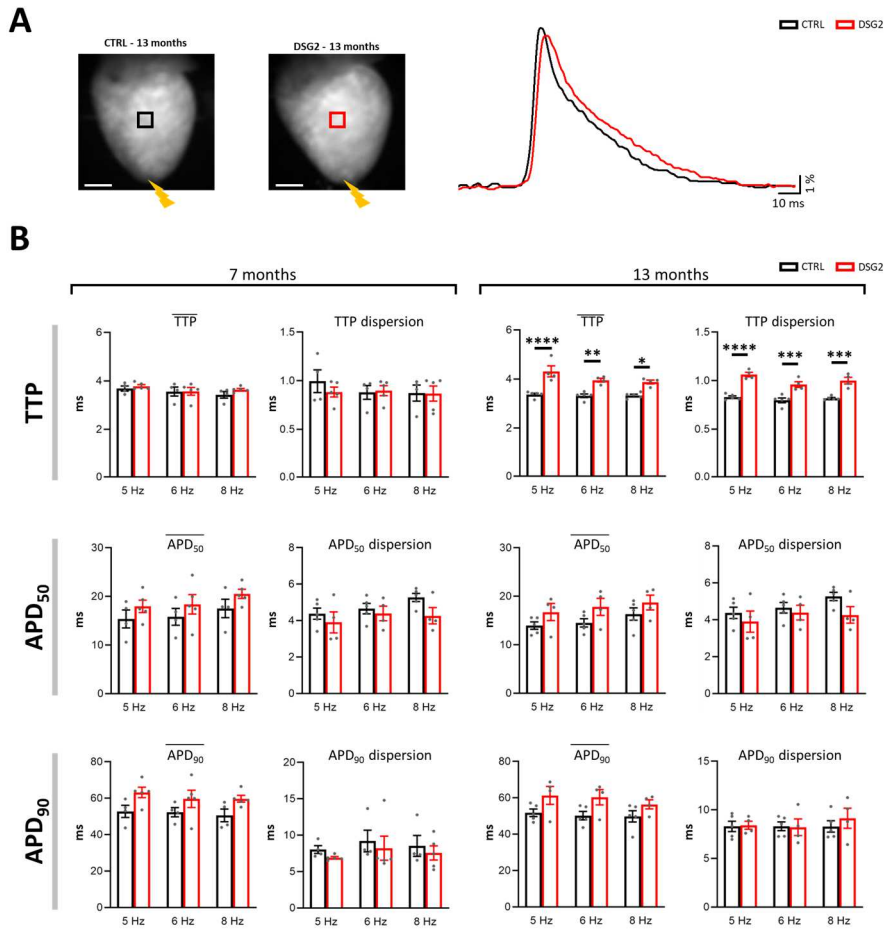


Figure 27: Action potential kinetics in CTRL and a DSG2 mouse hearts. (A) Representative fluorescence images of a CTRL and a DSG2 mouse heart. Scale bar 2 mm. Mouse hearts were electrically paced at the apex (yellow bolt) applying a burst of 10 stimuli at 5 Hz. Fluorescent signals ($\Delta F/F$) extracted from the black ROI (black trace) and in the red ROI (red trace) from CTRL and DSG2 mouse hearts respectively. (B) Mean values (average of the entire left ventricle) and dispersion (evaluated as the standard error of the mean across the left ventricle) extracted from left ventricular maps of Time-to-Peak (TTP) and Action Potential Duration (APD) at 50% and 90% of repolarization (APD₅₀ and APD₉₀ respectively). Data were collected from 9 CTRL mouse hearts (4 at 7 months and 5 at 13 months) and 9 DSG2 mouse hearts (5 at 7 months and 4 at 13 months). Two-way ANOVA with Tukey test means comparison was applied.

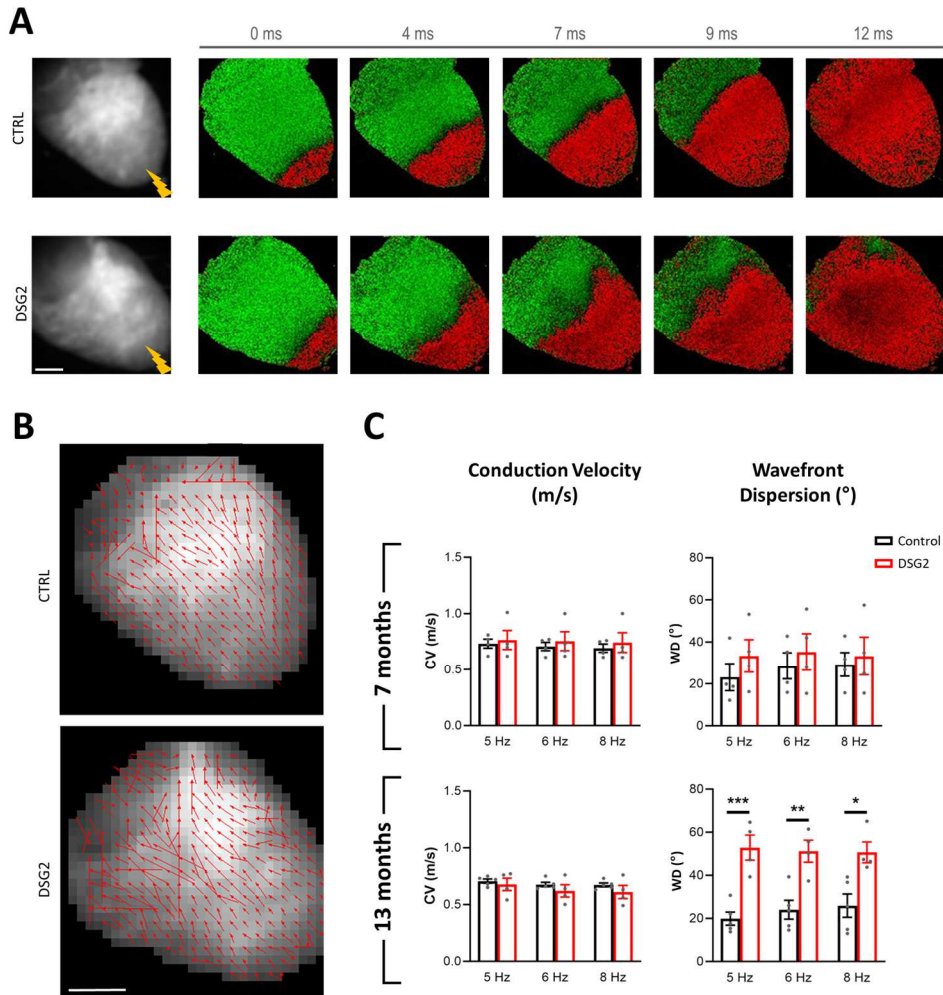


Figure 28: Conduction velocity in CTRL and a DSG2 mouse hearts. Action potential propagation analysis. (A) Electrical stimulation in CTRL and DSG2 whole mouse hearts. Left panels: fluorescence images (F_0) of CTRL (top) and DSG2 mice (bottom) hearts stained with a Voltage Sensitive Dye (VSD) and electrically stimulated at the apex (yellow bolt) with a pacing rate of 5 Hz. Scale bar: 2 mm. Right panels: five representative frames of optical mapping (DF/F_0) recordings in the same hearts. Electrical activation is visualized in red and the baseline in green. (B) Conduction velocity (CV) maps of the CTRL (top) and DSG2 (bottom) mouse hearts showed in (A), with the local direction of action potential propagation represented by a vector. Scale bar 2 mm. (C) Average CV and wavefront dispersion (evaluated as standard deviation of angles of propagation vectors in the CV maps) at 7 and 13 months of age. Data were collected from 9 CTRL mouse hearts (4 at 7 months and 5 at 13 months) and 9 DSG2+/+ mouse hearts (5 at 7 months and 4 at 13 months). Aggregated data is reported as mean \pm SEM and two-way ANOVA with Tukey test means comparison was applied.

We additionally evaluated CV and wavefront dispersion as a function of the pacing rate in DSG2 and CTRL intact hearts. Figure 28, panel A shows representative frames of the optical mapping recorded with a stimulation frequency of 5 Hz in CTRL (top) and DSG2 (bottom) mouse hearts aged 13 months. The CTRL mouse heart exhibits linear and uniform AP wave-front propagation from the apex towards the base. In contrast, in the DSG2 mouse heart, the AP wavefront is irregular and shows distortions. This is further emphasized in panel B of Figure 28, where AP wavefront dispersion as the standard deviation of angles of propagation vectors is reported. Wave-front dispersion was considerably increased in DSG2 hearts, as compared to CTRL (12.16° in CTRL; 64.62° in DSG2). This increased wavefront dispersion was only statistically significant at 13 months of age, while only a tendency was observed at 7 months of age. Meanwhile, local CV was similar between CTRL and DSG2 mouse hearts, and no significant differences were observed (Figure 28, panel C).

4.1.2 Arrhythmias

Susceptibility to arrhythmias was assessed by mimicking the ventricular parasystole rhythm in CTRL and DSG2 mouse hearts. While keeping the sinus node (SN) intact, we electrically induced extra beats at the right ventricular outflow tract (RVOT) at a period of $1.7 \times$ (SN period of the mouse heart). Figure 29 panel A shows an example of an induced arrhythmia, displaying a self-terminating episode of polymorphic ventricular tachycardia in a DSG2 mouse heart aged 13 months. During this arrhythmic episode, we observed AP propagating in two spiral waves which rotate and converge in one, thus eventually activating all cardiac tissue (representative frames in Figure 29, panel B).

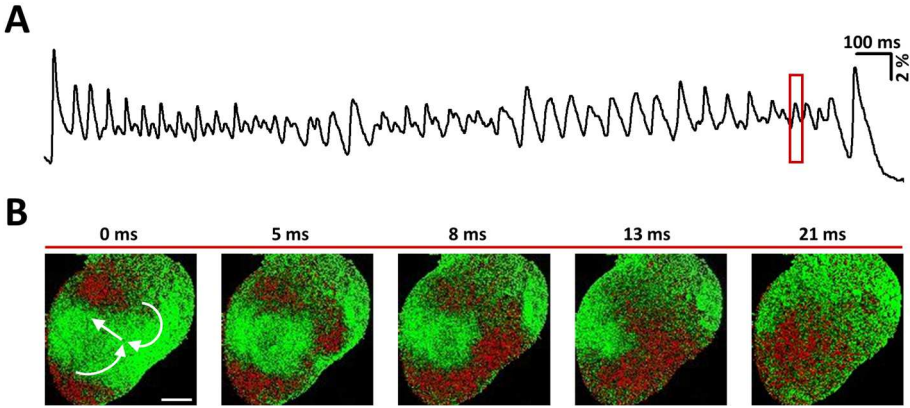


Figure 29: Arrhythmia episode in DSG2 mouse heart. (A) Fluorescent signals ($\Delta F/F$) showing a self-terminating episode of induced arrhythmia in a DSG2 mouse heart at 13 months of age. (B) Five representative frames of the fluorescent signals ($\Delta F/F$) recorded in the red box in panel A, showing AP propagation as two rotating spiral waves which converge in one. White arrow indicates wavefront direction. The electrical activation is reported in red and the baseline in green. Scale bar: 2 mm.

Overall, DSG2 mouse hearts aged 7 and 13 months exhibited a significant higher number of arrhythmia episodes compared to CTRL, thus showing a higher susceptibility for cardiac arrhythmias (Figure 30). We additionally evaluated the duration and frequency of cardiac arrhythmia episodes. While no difference in arrhythmia episode duration was found between CTRL and DSG2 mouse hearts at either 7 or 13 months of age, a significant decrease in arrhythmia frequency was found in DSG2 mice aged 13 months, but not at age 7 months. The latter may be explained by APs propagating and rotating around a region of non-excitabile tissue (e.g. fibrosis) in a vortex-like fashion (as shown in Figure 29, panel B), thus increasing the arrhythmias cycle length. To summarize, in DSG2 mouse hearts we found an increase in cardiac arrhythmia occurrence as well as a decrease in arrhythmia frequency.

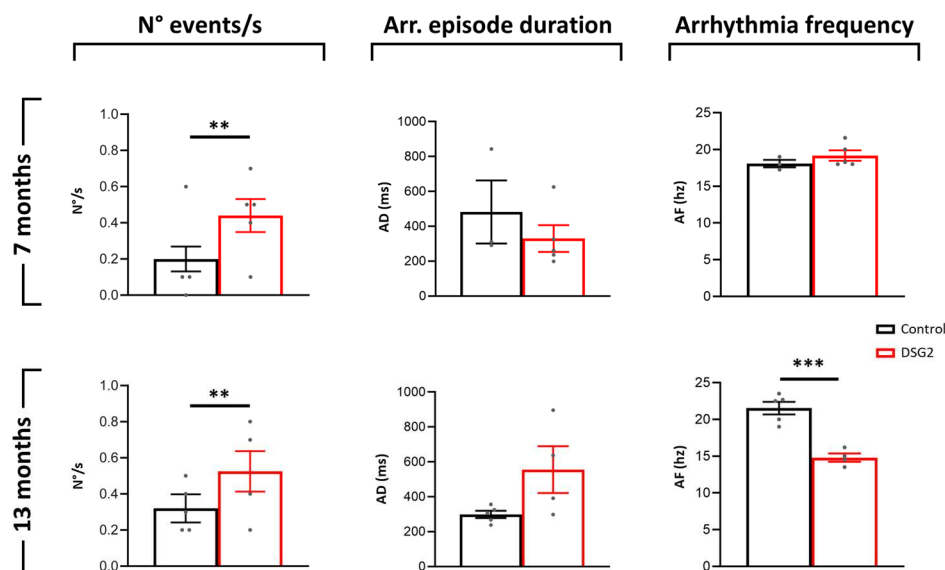


Figure 30: Arrhythmia analysis in CTRL and DSG2 mouse hearts. Susceptibility to arrhythmia was assessed by mimicking the ventricular parasystole rhythm. Briefly, mouse hearts were electrically paced (yellow arrow) for 10 s at the right ventricular outflow tract (RVOT) at a period of $1.7 \times$ (sinus node period of the mouse heart). The number of arrhythmic events induced per second (N°/s), arrhythmia episode duration (AD), and frequency (AF) in CTRL and DSG2 mice hearts at age 7 months and 13 months are shown. Data were collected from 9 CTRL mouse hearts (4 at 7 months and 5 at 13 months) and 9 DSG2^{+/+} mouse hearts (5 at 7 months and 4 at 13 months). Aggregated data is reported as mean \pm SEM and student's t-test for means comparison was applied.

4.2 Whole heart reconstruction

4.2.1 Cleared tissue preservation

The SHIELD tissue transformation protocol optimized for cardiac tissue was successfully applied to nine CTRL and nine DSG2 samples, allowing us to obtain perfectly preserved optically transparent whole mouse hearts.

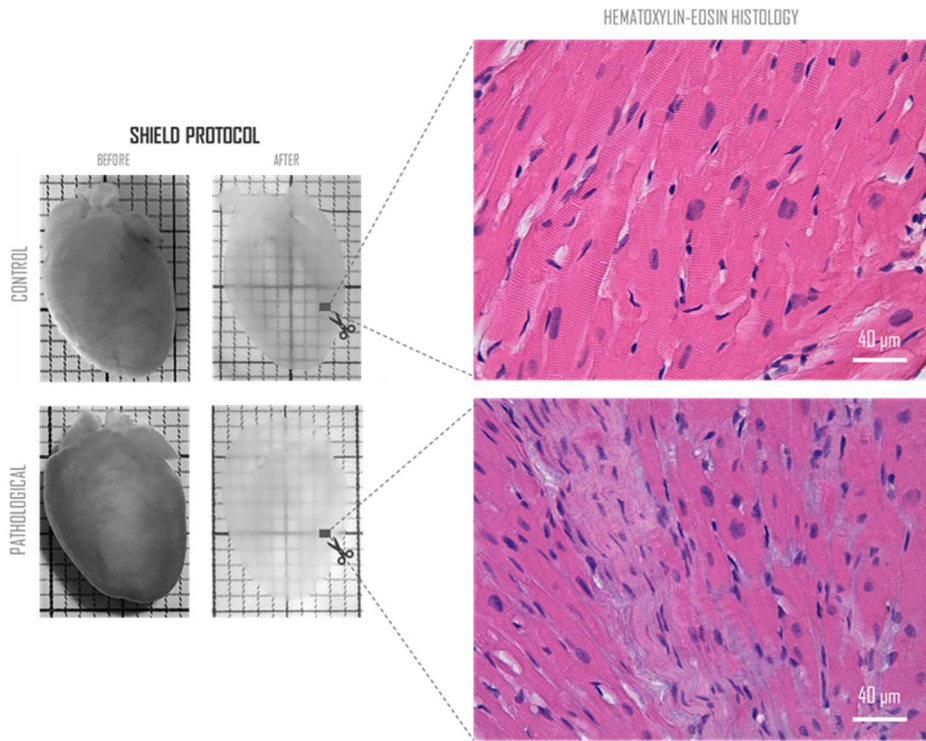


Figure 31: Clarified tissue preservation. Left panels: photos of representative CTRL (top) and DSG2 (bottom) pre- and post-clearing murine hearts. Size of background squares: 1mm x 1mm. Right panels: results of the histological inspection of post-clearing murine myocardium tissue, performed using haematoxylin-eosin staining of sections from the healthy (top) and DSG2 (bottom) samples. Scale bar = 40μm.

As shown in Figure 31, the sample tissue is optically transparent at the end of the SHIELD tissue transformation protocol. The overall size of the organ

is unaltered, and no deformations which could distort our structural studies were present.

Because of the aim of this thesis, it is fundamental to verify that the integrity of the organ was maintained from not only a macroscopic point of view, but also at a microscopic level. To confirm the tissue integrity after the clearing protocol, histological analyses were carried out on one CTRL and one DSG2 sample, using haematoxylin-eosin staining, which is still considered the gold standard for the morphological study topographical and general study of tissues and organs. Two representative histological sections are shown in Figure 31. Murine hearts cleared with tissue transformation protocol appear unaltered and perfectly preserved even at the histological level. All characteristic features of optimally preserved cardiac muscle tissue can be observed, including central nuclei, transverse striae, and the course of cardiomyocytes that bifurcate and anastomose with each other.

4.2.2 Image acquisition and analysis

We applied the label-free MesoSPIM imaging protocol developed during this project to all CTRL and DSG2 cleared murine hearts, allowing for the obtaining of dual-channel tomographic reconstructions of whole murine hearts with a final voxel size of $6\text{ }\mu\text{m} \times 6\text{ }\mu\text{m} \times 6\text{ }\mu\text{m}$. Figure 32 shows longitudinal and sagittal sections of a representative CTRL mouse tomography.

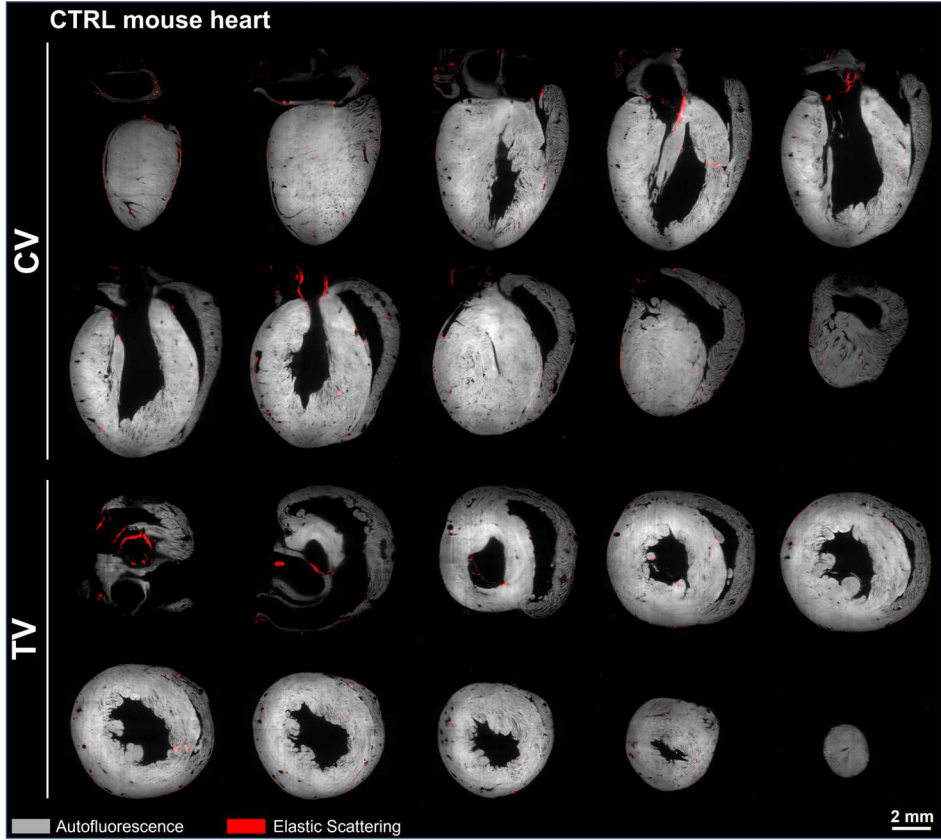


Figure 32: MesoSPIM tomography of a cleared murine heart. A representative whole-heart reconstruction of a murine heart from a healthy mouse was performed following the SHIELD clearing protocol and the MesoSPIM-based imaging protocol developed during this thesis. For each heart, two identical reconstructions were performed with and without a long-pass filter ($\lambda > 650$ nm) to collect tissue autofluorescence (here represented with a grey signal) and elastic scattering (red signal), respectively. TV = Transverse View; CV = Coronal View. Original images voxel size: $3.25 \mu\text{m} \times 3.25 \mu\text{m} \times 3.0 \mu\text{m}$; two-channels whole-heart tomography voxel size: $6 \mu\text{m} \times 6 \mu\text{m} \times 6 \mu\text{m}$.

From these tomographic images, it was possible to virtually reconstruct the three-dimensional anatomy of the entire heart with micron-scale resolution. Figure 33 shows two representative whole-heart 3D reconstructions views of CTRL and DSG2 mouse hearts.

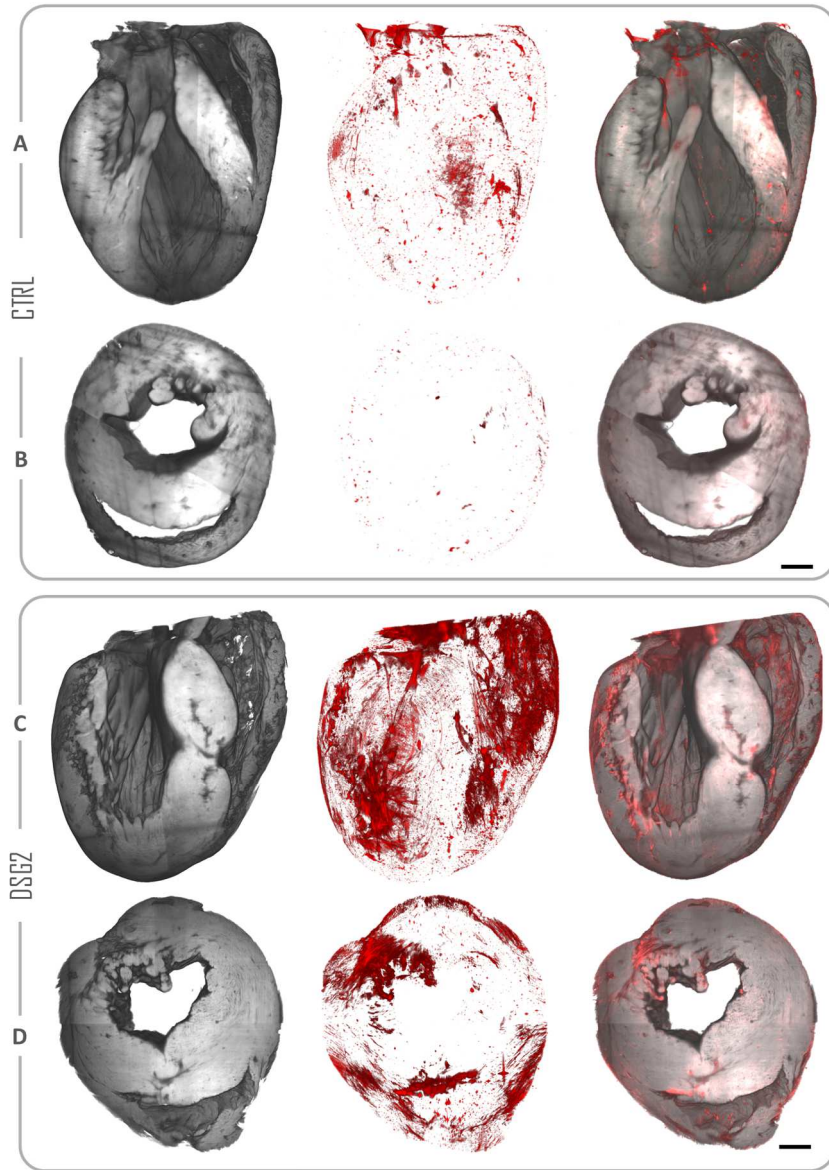


Figure 33: Mouse whole heart reconstruction. Coronal (A, C) and transversal (B, D) views of three-dimensional reconstructions of entire cleared mouse hearts performed with the MesoSPIM using a 638 nm light source are shown. Three-dimensional reconstructions are generated with an isotropic voxel size 6 μm by original images with a pixel size of 3,25 μm x 3,25 μm x 3 μm in XYZ and rendered with ImageJ software (). The final reconstructions (on the right) are generated by merging the two channels. Autofluorescence signal allow us to reconstruct the organ anatomy, useful for structural investigation. Here, the DSG2 heart affected by arrhythmogenic cardiomyopathy appears with a compromised left ventricle wall.

Instead, the intensity of the light scattering signal appears to be related to the extracellular matrix composition (in detail, we expected it is proportional with collagen deposition). In fact, in the healthy heart light scattering is evident only around vessels and valves. In the DSG2 heart, we observe high collagen depositions in the left ventricle myocardial walls, suggesting the presence of a patchy fibrosis area. Scale bars: 1 mm.

First, the muscle autofluorescence signal allowed to visualize in both samples the overall architecture of the heart chambers and to appreciate specific features of the cardiac anatomy: the thickness of the ventricular walls, their geometry, and the structure of the internal cavities: on the inner surface of the ventricles, reliefs called flesh trabeculae are visible, due to the protrusion of myocardial bundles.

Second, significant differences in the intensity of the elastic scattering signal were observed between the CTRL and the DSG2 heart. Our CTRL heart reconstructions show that the scattering signal comes almost exclusively from great vessels and heart valves, structures that are naturally made of collagen. In contrast, the representative DSG2 heart exhibited a scattering signal originating from the left ventricular wall as well as the endocardium of the RV, which are areas where such an abundance of collagen is not to be expected.

Therefore, a deeper investigation of the tomographic reconstructions obtained with the proposed imaging protocol is required. To this end, we first analyzed the content of each channel individually.

4.2.2.1 Myocardium anatomy by autofluorescence signal

We utilized autofluorescence images to perform a macroscopic structural investigation on the myocardium anatomy in our CTRL and DSG2 mouse hearts.

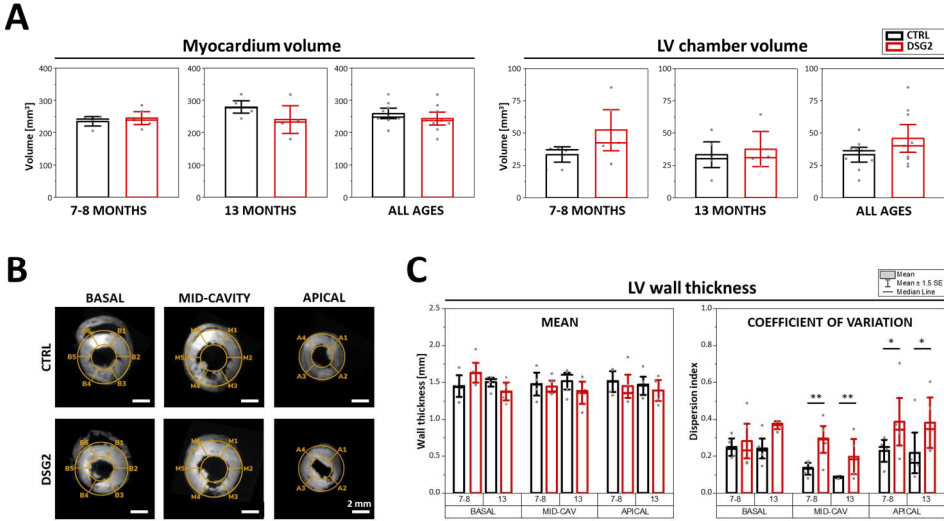


Figure 34: Results of myocardium anatomical investigation. (A) Volumes of myocardium and Left Ventricle (LV) chamber calculated by three-dimensional segmentation of MesoSPIM-based organ reconstructions of CTRL and DSG2 mouse hearts. (B) Representative Short-Axis views of autofluorescence signal (in grey) of CTRL and DSG2 mouse heart reconstructions used to measure LV wall thickness following the AHA seventeen-segments standard protocol (superimposed in yellow). (C) Mean and variation coefficient of LV wall thickness measurements performed on CTRL and DSG2 mouse hearts. Data were collected from 9 CTRL mouse hearts (4 at 7 months and 5 at 13 months) and 9 DSG2+/+ mouse hearts (5 at 7 months and 4 at 13 months). Aggregated data is reported as mean \pm sem and two-way ANOVA with Tukey test means comparison was applied.

First, by automatically segmenting the myocardium in our 3D LR reconstructions, we calculated the total volume of the contractile tissue and the volume of the LV chamber. Results are shown in Figure 34A.

We found no statistical differences between CTRL and DSG2 samples in terms of the amount of myocardial tissue and LV chamber volume, suggesting that tissue hypertrophy or ventricular chamber dilation did not occur in DSG2 hearts.

Next, we manually measured the cardiac wall thickness in all CTRL and DSG2 mouse hearts following the sixteen-segments model (Figure 34B) of the AHA. Results are shown in Figure 34C. We observed no difference in average wall thickness in basal, mid-cavity, and apical segments between

CTRL and DSG2 mouse hearts. However, the angular variability of the wall thickness was more pronounced in DSG2 mice in all segments, with statistical significance for both mid-cavity and apical segments. This observation suggests the presence of a remodeling process occurring in the LV wall of DSG2 mice.

This low-resolution anatomical investigation revealed the absence of strong dilation or tissue hypertrophy while providing preliminary clues about an LV remodeling process. Moreover, observations in CTRL hearts were coherent with the expected anatomical features, confirming the reliability of our cleared-heart mesoscopic reconstructions in terms of organ preservation.

By switching to high-resolution tomographies, we verified that the proposed method was able to resolve individual fibers that compose cardiac tissue. Figure 35 shows representative high-resolution autofluorescence images of a CTRL mouse reconstruction performed with the MesoSPIM setup.

The transparency of the sample, combined with the imaging performance of the MesoSPIM, allowed us to resolve each contractile fiber in three-dimension in the entire heart. The image quality is sufficient to detect single bundles of cardiomyocytes in both Long Axis (LAX) and Short Axis (SAX) planes i.e., in the image plane (XY plane) and in the transversal plane (XZ) respectively, where Z is the optical axis.

In the LAX view, the shape of the LV is clearly visible, with a big trabecula crossing the chamber. On the top-left of the image, a glimpse of the RV structure extending behind the image plane can be observed, while on the right near the epicardial surface the sections of the main vascular structures can be detected.

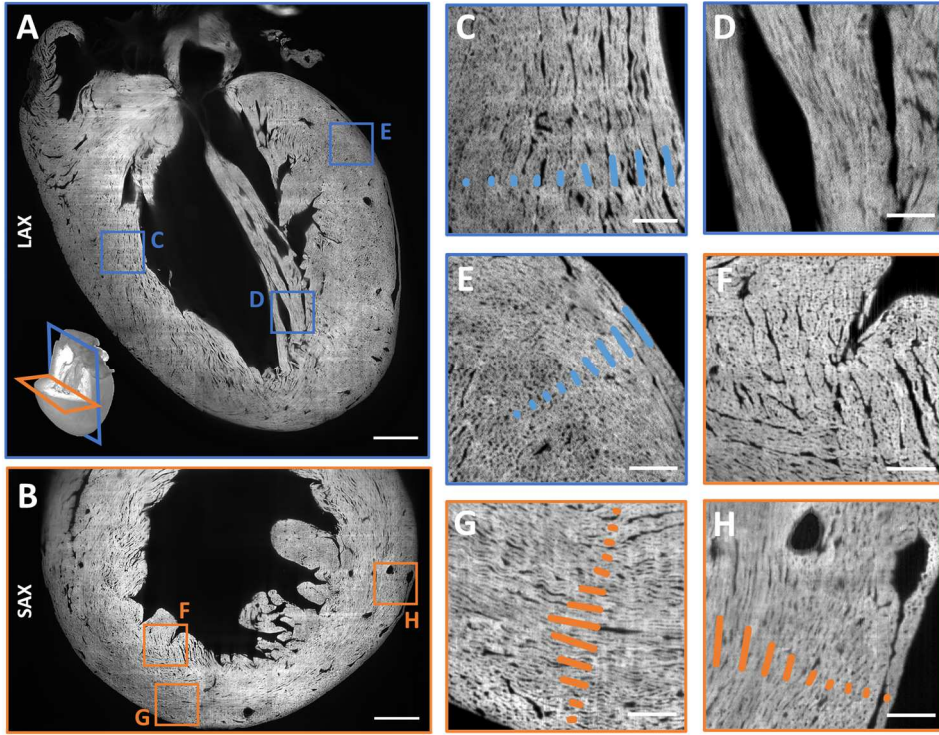


Figure 35: Resolving contractile fibers in the entire heart. High-resolution reconstructions of autofluorescence signal of cardiac muscle tissue of a cleared healthy mouse heart collected with the MesoSPIM. (A, B) The long axis (LAX) plane and Short Axis (SAX) plane sections are shown. Muscle fibers are well resolved in both LAX and SAX views, enabling detection of fibers alignment following the helical angle distribution in the myocardial wall (highlighted in C, E, G, and H panels). It is possible to resolve fibers also in the trabeculae inside the cardiac chamber (panels D, F). Pixel size: $3,25 \times 3,25 \mu\text{m}$. Scale bar: 1mm (left panels), $200 \mu\text{m}$ (1-6 inserts).

The presented results confirm that the resolution of the system allows us to reconstruct the tissue organization at a micrometric scale of up to the LV wall depth. In fact, we can identify sections and longitudinal profiles of each contractile fiber where perpendicular and parallel to the image plane respectively. As expected, fibers composing the LV wall follow the helix angle distribution between the epi- and the endocardium surfaces, as highlighted with blue strips in panels C and E. Moreover, the quality of the 3D reconstruction was confirmed also *inside* the LV, for example by

detecting the well-organized arrangement of the fibers composing a trabecula (panel D).

Even in the SAX view (Figure 35, panel B), where the optical capability is expected to be impaired to respect to the imaging plane, the MesoSPIM produced outstanding reconstructions. The LV pool is visible together with the sections of anterior and posterior papillary muscles, and a partial section of the RV chamber. As in the LAX view, by zooming in the organization of the fiber is clearly visible, arranged parallel to the heart circumference, and rotating between epi- and endocardium as highlighted by the orange strips (panels G, H). With a close look at the endocardial tissue (panel F), where are expected fibers almost parallel to the long axis of the heart, is possible to resolve tissue organization from the main bundles up to the section of each contractile fiber perpendicular to the image plane.

In short, these results confirm that the proposed label-free imaging protocol allows reconstruction of the organization of the contractile fiber in entire mouse hearts, able to resolve single contractile fibers bundles with a micrometric resolution. Hence, this technique opens the way to a more comprehensive three-dimensional structural investigation.

4.2.2.2 Scattering Signal

While autofluorescence can be used to visualize muscle components, collagen fibers are the main source of tissue scattering due to their high RI and fibrous nature. Therefore, the scattering signal can potentially be used to localize and quantify fibrous tissue. In CTRL hearts, scattering signal comes mainly from areas around main vessels and valves. Indeed, as shown in Figure 32 (SAX view, first section), the circumference of the aorta is clearly visible.

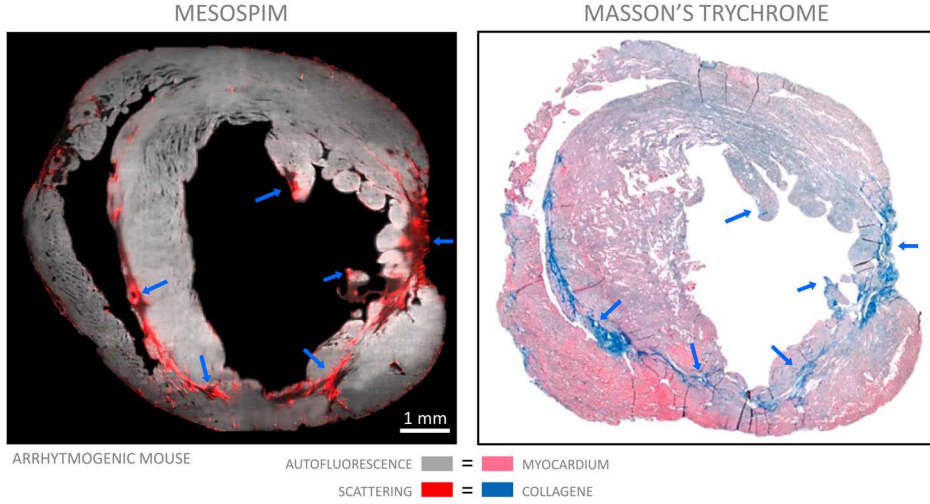


Figure 36: Comparison of the same cardiac section of a mouse affected by arrhythmogenic cardiomyopathy. On the left, a section of a MesoSPIM-based tomography where autofluorescence signal (in grey) and scattering signal (in red) are shown. On the right, a Masson's trichrome staining of the correspondent semi-final histological section of the same heart highlights myocardial tissue (in pink) and collagen deposition (in blue). Histology confirms the accuracy of the proposed scattering-based approach to detect fibrosis areas (blue arrows). Scale bar: 1 mm.

To validate our observations, we again used the histological analysis, performing Masson's Trichrome staining to our samples after the MesoSPIM-based imaging protocol. In Figure 36, the same SAX section of a DSG2 heart is shown reconstructed by MesoSPIM imaging (dual-channel image extracted by the heart tomography composed by autofluorescence (grey) and scattering (red) signal) and by Masson's Trichrome staining (where pink represent myocardium and blue collagen depositions).

Blue arrows superimposed on the MesoSPIM image point to areas with high scattering signal, thus indicating a prevalence of collagen deposition / fibrotic tissue. These areas can also be detected by the Masson's trichrome staining in blue, Therefore, these results validate our initial assumptions about the origin of the scattering signal and confirm the ability of our system

to successfully detect fibrotic areas within whole murine hearts using an optical sectioning process.

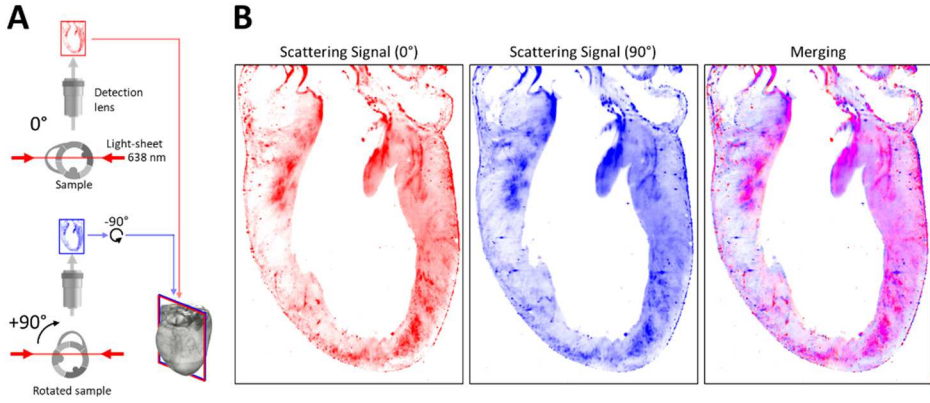


Figure 37: Scattering signal independency from excitation direction. (A) Schematic diagram of the excitation and acquisition paths of the scattering signal in two perpendicular configurations. (B) Representative tomographic sections of the scattering signal of the same murine heart affected by arrhythmogenic cardiomyopathy, collected at 0° and 90° and subsequently realigned, are shown separated and merged.

However, light scattering is a phenomenon of the interaction of waves with matter which consists of the deviation of a beam when it meets a set of particles in its path, from which it is deflected. This phenomenon is thus characterized by the directionality of the emission.

In the case of fluorescence, which is an incoherent process, the fluorescent molecule, regardless of how it has been excited, emits fluorescence isotropically, which is equiprobably in all directions. Scattering, on the other hand, is a coherent process, so maintains both energy and pulse; it retains the “memory” of the wave vector of the exciting photon.

Due to the intrinsic nature of the phenomenon, we decided to verify whether scattering information contained in our reconstructions could be affected by the direction of the optical sectioning. We performed our acquisitions placing the sample at two perpendicular angles of 0° and 90° (Figure 37, panel A).

Figure 37, panel B, shows that representative sections of two perpendicular acquisitions of the same heart previously realigned are perfectly superimposable. Result confirms that the different direction of the excitation does not change the nature and characteristics of the acquired scattering signal.

Therefore, the results of the imaging protocol are encouraging in the direction of applying high-resolution structural investigation to our cleared whole mouse heart reconstructions.

4.3 Mesoscopic structural investigation

We utilized our high-resolution tomographic reconstructions to perform an in-depth investigation of the fine anatomy of the organ, in terms of contractile fiber organization and fibrotic area distribution. In particular, after the macroscopical characterization of myocardial anatomy already performed on the low-resolution tomographies, now we focused on the local organization of cardiac muscle cytoarchitecture at a multicellular scale, and the amount (and spatial arrangement) of fibrotic areas in our samples.

The two channels composing our high-resolution images were first analyzed individually by specially developed analysis software tools, and results were interpreted and then combined to obtain a comprehensive overview of the structure of healthy and DSG2 mouse hearts.

4.3.1 Myocardium fiber organization

The autofluorescence signal of cleared hearts imaged with MesoSPIM provided us a beautiful overview of the fiber arrangement in the entire organ. We used our 3D images to reconstruct the complete three-dimensional fiber architecture with a high spatial resolution. Next, we quantified the fiber local

alignment degree of the myocardium in the entire organ creating three-dimensional maps that we can correlate with our functional maps.

4.3.1.1 Cytoarchitecture reconstruction

From the high-resolution autofluorescence images, we can reliably identify fiber orientation down to a scale of tens of micrometers (Figure 35). We applied the proposed STA-based fiber orientation analysis to our HR tomographies with a spatial resolution of $96\text{ }\mu\text{m} \times 96\text{ }\mu\text{m} \times 96\text{ }\mu\text{m}$. In Figure 38, fiber orientation tracking is superimposed on two representative sections of a CTRL mouse heart. Local three-dimensional fiber orientation is represented as a two-dimensional vector, where the vector length represents the “in-plane” component (XY plane), and color maps the “out-of-plane” component (Z-axis).

The result demonstrate the capability of the image analysis pipeline to correctly detect fiber orientation across the entire organ. In panel A, an LAX plane section of the LV with a depth of about 1.4 mm shows the entire depth of the cardiac wall, from the epicardial surface down to the beginning of the LV chamber. The orientation vectors follow the overall organization of tissue fibers. Notably, the color gradient from the epi- to endocardial surface suggests a correct detection of fiber inclination relative to the image plane, as the observed pattern overlaps with the expected helix angle distribution. Moreover, with a closer look in the center of the image where some contractile fibers located on the endocardium surface appear wavier, it is possible to verify the high spatial sensitivity of the analysis to detect the principal local orientation of each fiber portion.

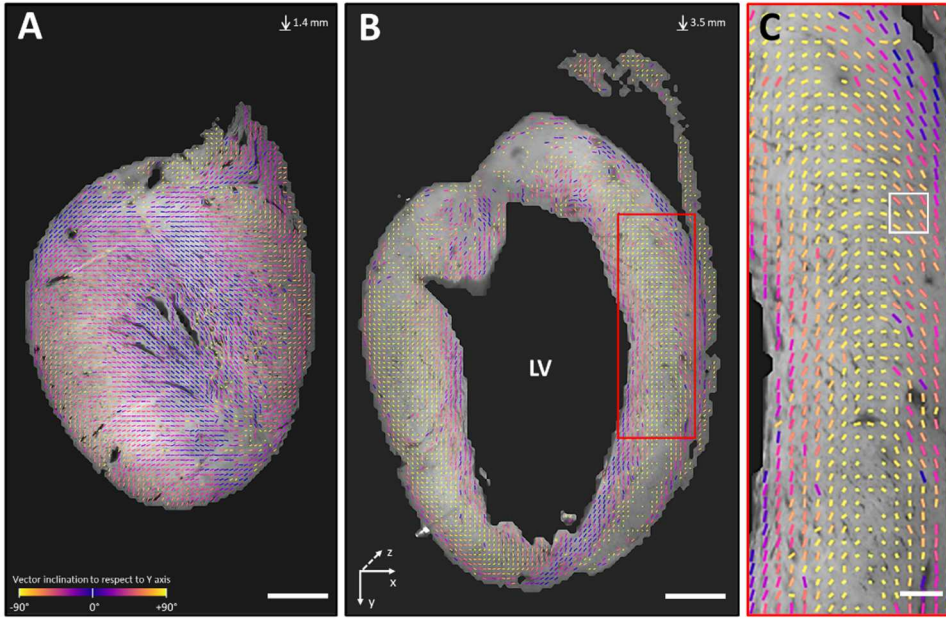


Figure 38: Whole-heart three-dimensional fiber orientation mapping. Result of three-dimensional fibers orientation analysis (colored vectors) is superimposed on the autofluorescence signal (grey) in two representative sections of a CTRL mouse heart reconstruction. Fiber orientation was estimated with a spatial resolution of $96\ \mu\text{m}$. Each 3d orientation is represented with a 2d vector: here, vectors length represents the “in-plane” component (xy plane); color represents the “out-of-plane” component (z-axis). The method can detect fiber orientation at different depths (A, 1.4 mm depth; B, 3.5 mm depth) as well inside the ventricular wall (C). The helix angle distribution of the fibers is clearly visible in the left ventricle wall (insert C). A $3 \times 3 \times 3$ vectors area (white square, panel C) highlights a spatial resolution $288\ \mu\text{m} \times 288\ \mu\text{m} \times 288\ \mu\text{m}$. Scale bars: (A, B) 1 mm, (C) $300\ \mu\text{m}$.

In Figure 38, panel B, a deeper section of the same reconstruction is shown, highlighting the result of fiber tracking analysis in the middle of the LV walls. The proposed approach gave promising results even here, where orientation vectors follow the fiber arrangement of the myocardium wall with high sensitivity. By comparing results with the expected organization of healthy CTRL mouse hearts, is possible to validate the proposed analysis: it is clearly visible the distribution of the vector from the endo- to the epicardial surface, with fibers parallel to the heart LAX in the endocardium surface, parallel to the circumference in the middle of the wall, and again

almost parallel to the heart LAX in the epicardial surface. Moreover, the fiber tracking correctly detects the ventricular muscle arrangement in the apex, where muscle sheets intertwine one layer on top of the other.

It is important to note that in some areas, especially near the base of the heart, where tissue is deeper and more compact, the lack of tissue transparency can affect the optical sectioning capability of the MesoSPIM. The resulting autofluorescence signal in those areas appears blurry, preventing determination of single muscle fibers. By utilizing the Fractional Anisotropy of each analyzed sub-volume as an index of the local resolution of autofluorescence signal, the software discards orientation vectors with too low reliability, preventing invalidate the overall result.

By reallocating each orientation versor in the original position inside the analyzed organ (i.e., the heart reference system), we reconstructed the three-dimensional cytoarchitecture of each sample as a virtual orientations map. In Figure 39, virtual cytoarchitectures of CTRL and DSG2 entire mouse hearts are shown in longitudinal and transversal views.

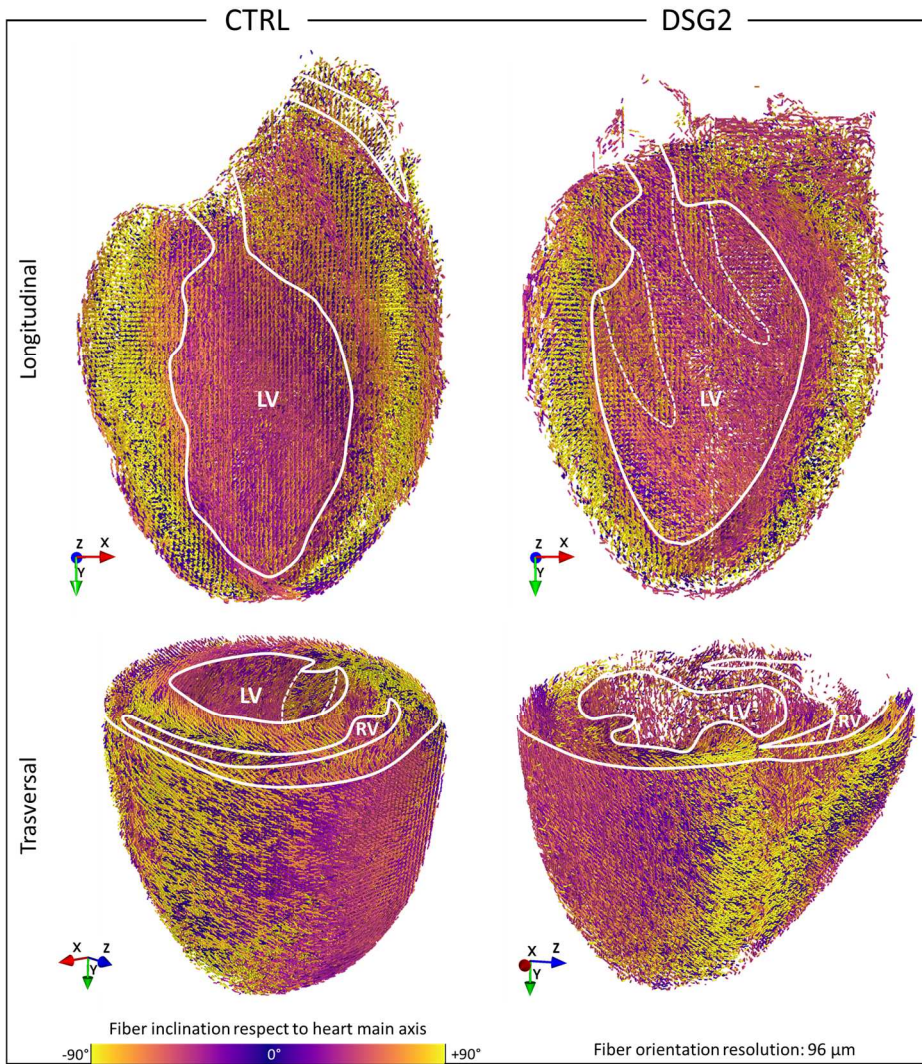


Figure 39: Whole heart cytoarchitecture reconstruction. Whole heart three-dimensional myocardium fibers reconstructions of representative CTRL and DSG2 mouse hearts are shown. Each fiber orientation (detected by analyzing the autofluorescence signal with a spatial resolution of 96 μm) is represented as a 3D vector with unitary length and mapped with colors. Here, virtual reconstructions are dissected longitudinally and transversally (white lines represent the profile of myocardium walls) to appreciate the fiber organization inside the ventricular walls. Dashed lines highlight the main papillary muscles in the left ventricle (LV) endocardium wall.

First, the capability of the proposed approach to detect fibers orientation in almost the entire organ is confirmed. Orientation vectors density suggests the fibers are correctly detected down the depth of the tissue, and main anatomical features like heart shape, ventricular chambers, and big papillary muscles are recognizable even from these virtual 3D vectors maps.

The longitudinal view shows the arrangement of the fibers inside the LV wall in both CTRL and DSG2 samples, where the borders of the tissue are highlighted with white lines and color (representing the inclination of each fiber to respect to the heart long axis), confirming the expected overall organization of fibers following the helix angle distribution.

Observing the same maps cut with a transversal plane, we can observe the fiber distribution following the circumference of the organ and changing inclination moving from the endo- to the endocardium surfaces; notably, in the DSG2 sample, the fiber density in the RV border appears reduced when compared to CTRL, suggesting a lack of fibers detected in those areas.

The proposed analysis method based on the autofluorescence signal appears able to reconstruct the fiber organization of the entire myocardium with a spatial resolution of 96 μm . The resulting virtual orientations map can be exploited to evaluate the local organization of cardiac tissue fibers.

4.3.1.2 *Fibers Disarray Quantification*

Cardiac muscle has a complicated macroscopical organization, from muscle sheets interlacement down to helix angle distribution of fibers inside the cardiac walls. To measure the local fiber disarray without being affected by macroscopical structures, we virtually dissected each organ in sub-volumes of 288 $\mu\text{m} \times 288 \mu\text{m} \times 288 \mu\text{m}$. As explained in the *Fibers Disarray Quantification* section, it means analyzing the 3D virtual orientations map by selecting macro-voxels containing $3 \times 3 \times 3$ vectors (white square in Figure 38, panel C).

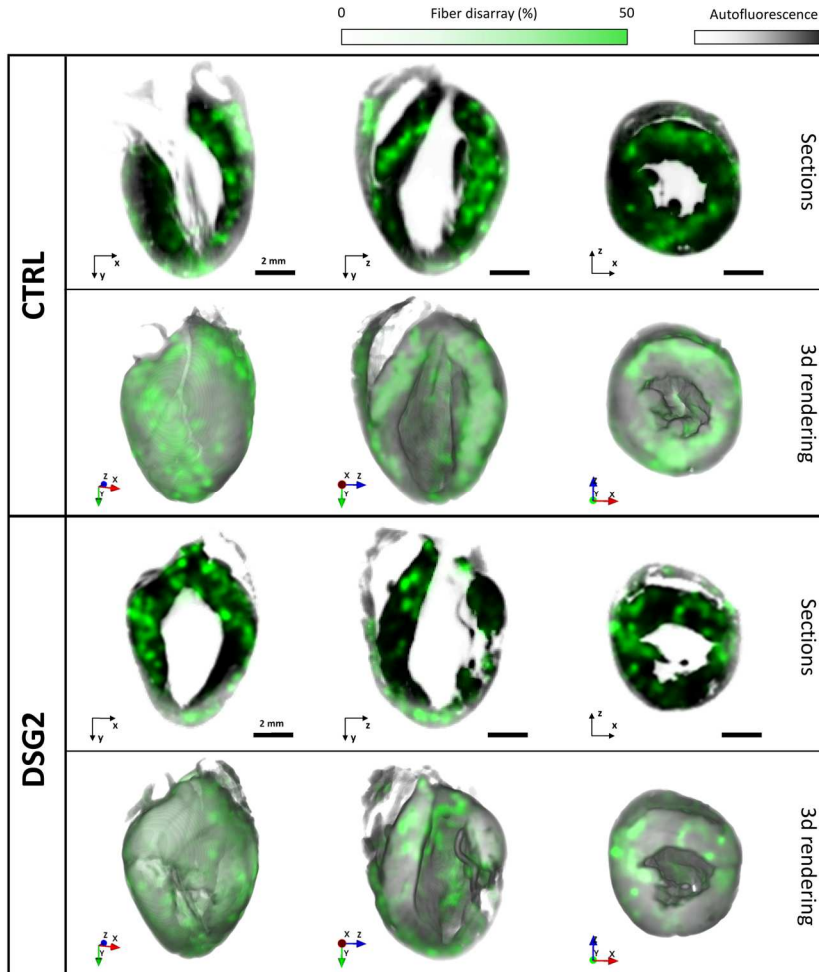


Figure 40: Myocardium local fibers disarray in entire mouse heart reconstructions. Sections and three-dimensional renderings of myocardium fibers disarray maps (green) of two representative samples are shown over the autofluorescence signal (grey). Local fiber disarray was calculated by the fiber orientation reconstructions with a spatial resolution of $288 \mu\text{m}$, and percentual results are mapped between 0% (order) and 50% (disorder) for better visualization. Both channels (disarray maps and myocardium reconstructions) are re-sampled with a voxel size of $78 \mu\text{m} \times 78 \mu\text{m} \times 78 \mu\text{m}$ before merging. Fiber disarray appears diffused inside the left ventricle walls in both CTRL and DSG2 samples, as well as distributed in the epi- and endocardium walls. The left ventricular wall appears compromised in the DSG2 sample (H, N). Scale bar: 2mm.

We measured the local fiber *disarray*, or ***d***, ranging from 0% (fibers perfectly parallel) to 100% (fibers completely disordered) in all our whole-heart cytoarchitecture reconstructions. Therefore, we created 3D tomographies of murine hearts with a spatial resolution of 78 μm combining the myocardium autofluorescence signal (in grey) and the local fiber disarray values (represented as increasingly intensity values of the green channel). Figure 40 shows representative 2D sections and 3D renderings of such fiber disarray maps of a CTRL and a DSG2 sample, where the intensity of the disarray channel (green) has been equalized between 0% and 50% to improve the visualization.

First, the results confirmed the capability of the proposed method to create comprehensive 3D anatomical reconstructions of the local fiber disarray in the entire organ. By a visual inspection of internal sections, contractile fiber disarray appears almost randomly distributed inside the myocardium, without evident differences between CTRL and DSG2 samples. Area with different degrees of fiber organization appeared in all the main hearts structures: LV, RV, and septum, while three-dimensional renderings show fuzzy fiber disarray in both epi- and -endocardium LV surfaces.

We then collected all ***d*** values from the disarray map of each sample and analyzed their distribution. In Figure 41, panel A, representative distributions of logarithmic values of fiber disarray - here called $\log(d)$ - are shown for two CTRL and two DSG2 hearts of mice at 7/8 months and 13 months of age with best normal fit superimposed.

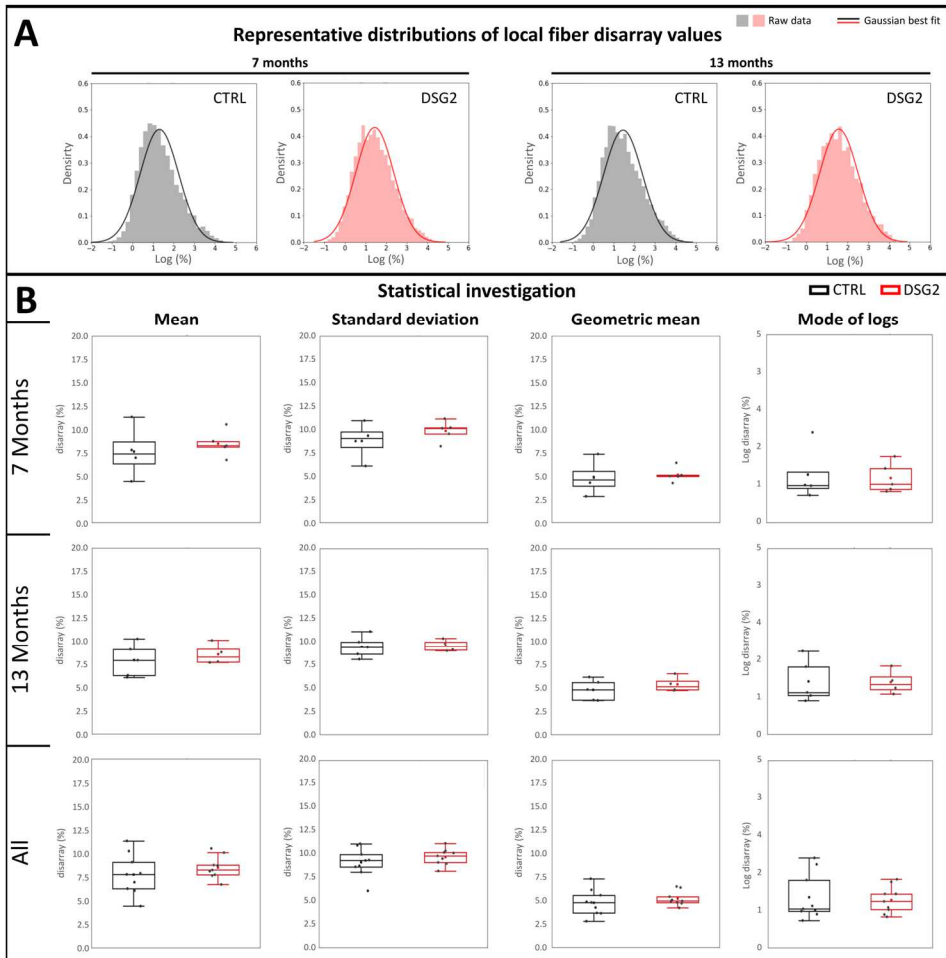


Figure 41: Myocardium fiber disarray distributions in CTRL and DSG2 mouse hearts. Results of contractile fibers disarray analysis performed with a spatial resolution of 288 μm on whole-heart myocardium reconstructions of nine ($n=4$ of 7 months age; $n=5$ of 13 months age) CTRLs and nine ($n=5$ of 7 months age; $n=4$ of 13 months age) DSG2 mouse hearts. (A) Representative distribution of $\log(d)$ (natural logarithm of disarray values) is shown for each group and mouse age. Best normal fits are superimposed. Distributions of fiber disarray are not log-normal (based on D'Agostino and Pearson's normality test (86, 87)) in all CTRL and DSG2 samples. (B) Results of statistical investigation on local fiber disarray values collected in CTRL and DSG2 mouse hearts. No statistical difference is found between CTRL and DSG2 mice at any age.

The fiber disarray data don't follow a log-normal distribution (D'Agostino-Pearson Normality Test). Therefore, we evaluated a set of statistical metrics

both to raw values d and $\log(d)$ distributions extracted by CTRL and DSG2 samples to provide an overall analysis of the fiber arrangement in the two groups for each mice's age and all ages together (Figure 41, panel B).

Arithmetic mean, standard deviation, and geometric mean of \mathbf{d} values don't show significant differences between CTRL and DSG2 mice. The average standard deviation is slightly higher than the arithmetic mean of disarray values in both CTRL and DSG2 samples, suggesting a wide heterogeneity of fiber arrangement, as anticipated by representative disarray maps. Moreover, the modes of the $\log(d)$ distribution were calculated and averaged. Also for these values, no significant difference in the distribution of disarray values between the two groups was detected.

The statistical investigation of fiber disarray values collected from CTRL and DSG2 mice shows no evidence of a different organization of contractile fibers between the groups. However, performing a structural analysis with a micrometric spatial scale to an entire centimeter-sized organ can hide some spatial patterns of myocardium fiber organization, which are potentially impossible to reveal by a visual inspection or aggregating all the local values. Therefore, we applied the spatial distribution analysis described in section 3.6.3 to our 3D fiber disarray maps, quantizing angularly and radially the LV circumference and LV wall in sixteen slices and sixteen rings respectively. We compared radial and angular distribution of fibers disarray in CTRL and DSG2 samples for each mouse age, and average results between samples creating 2D SAX maps of fiber disarray density. Results are shown in Figure 42.

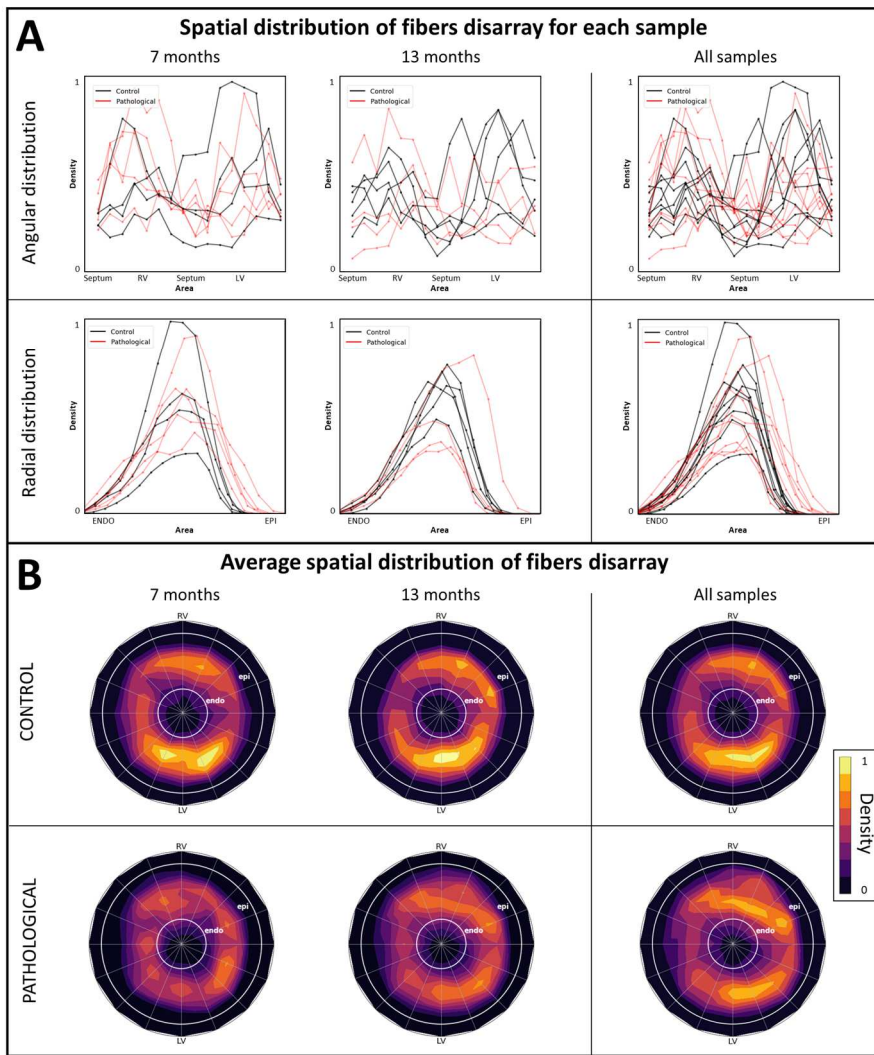


Figure 42: Spatial distribution of fiber disarray on CTRL and DSG2 mice. Angular and radial spatial investigations of fiber disarray (estimated with a resolution of 288 μm) were performed on nine ($n=4$ of 7 months age; $n=5$ of 13 months age) CTRLs and nine ($n=5$ of 7 months age; $n=4$ of 13 months age) DSG2 mouse hearts by sum the local fiber disarray along the main axis of each heart. (A) For each sample, results of angular (16-slices splitting of heart circumference) and radial (16 incrementally-radius rings from endo- to epicardium surface) fiber disarray quantization are shown. (B) Spatially-quantized disarray density is averaged between 7-months age, 13-months age and all CTRL and DSG2 samples, and mapped on a normalized SAX view of a mouse heart (endo: endocardium surface of left ventricle; epi: epicardium surface; LV and RV: Left (and Right) ventricles position).

The result of angular distribution analysis (panel A) shows that fiber disarray is uniformly distributed around the LV chamber; the results of radial quantization show fiber disarray is normally distributed between endo- and epicardium surface. Both investigations show fibers disarray is distributed comparably in CTRL and DSG2 samples. Average maps confirm an almost uniform distribution of fiber disarray in the whole heart myocardium, without difference between CTRL and DSG2 samples at any age.

In conclusion, the whole-heart fiber disarray investigation doesn't highlight a spatial pattern of the regularity of myocardium cytoarchitecture at multicellular level, nor a statistical difference between average results of CTRL and DSG2 mouse hearts at any investigated age.

4.3.2 Quantification of fibrotic tissue

We quantified the total amount of patchy fibrosis in all murine hearts using segmented scattering signals into our LR tomographies. Results are shown in Figure 43, panel A.

We found an average volume of fibrotic tissue (reported as mean \pm SEM in percentage respect to the myocardium volume) of $(1,74 \pm 0.47) \%$ for 7 months old mice increasing to $(1.98 \pm 0.81)\%$ for 13 months old mice, while in CTRLs mice we found $(0,30 \pm 0.16)\%$ and $(0,12 \pm 0.04)\%$ for 7 and 13 months old mice respectively. The difference between the two groups is statistically significant for mice aged 7 months and 13 months, as well as when aggregating all ages together.

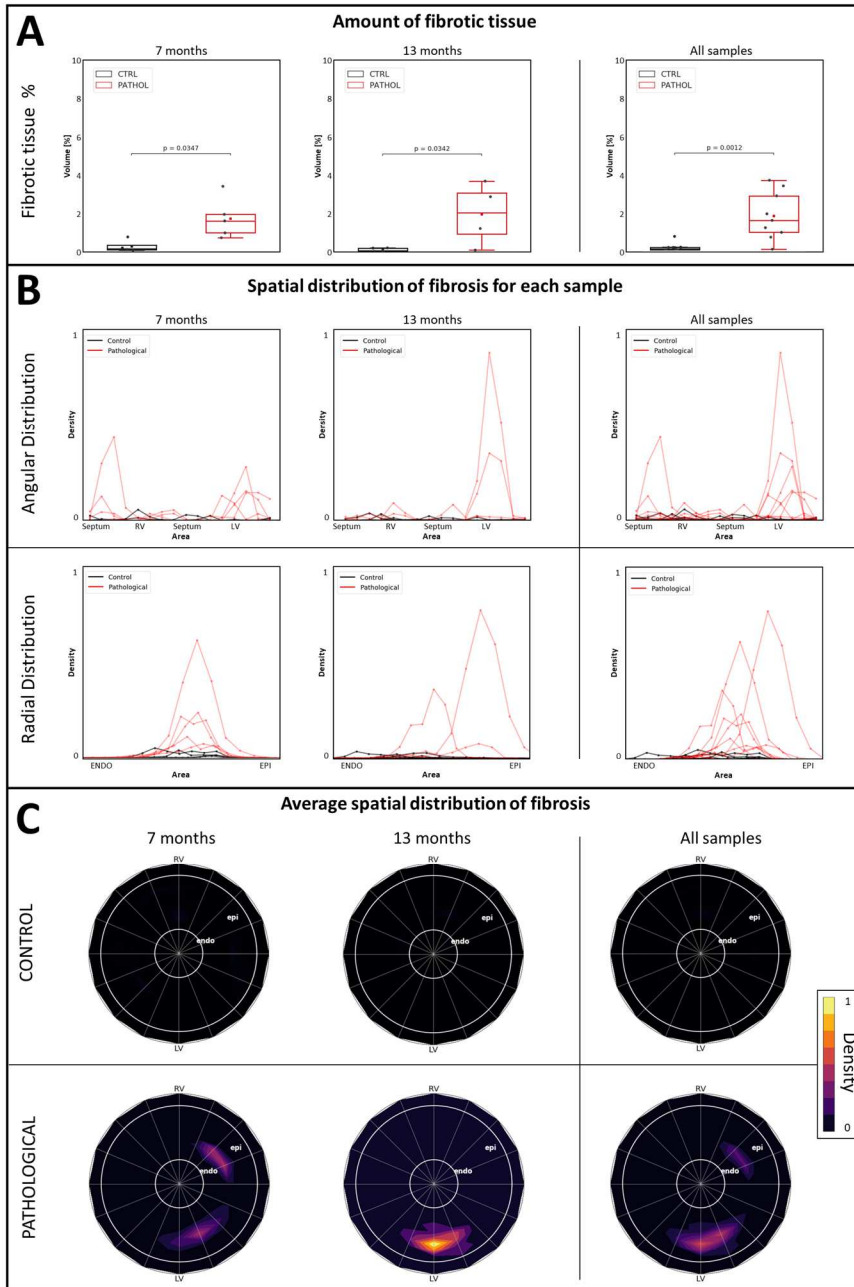


Figure 43: Quantification of fibrotic tissue. (A) Percentage of fibrotic tissue in respect to the total volume of the organ on nine ($n=4$ of 7 months age; $n=5$ of 13 months age) CTRLs and nine ($n=5$ of 7 months age; $n=4$ of 13 months age) DSG2 mouse whole hearts. (B, C)

Angular and radial spatial investigations of fibrotic area performed by averaging the scattering signal along the main axis of each heart. (A) For each sample, results of angular (16-slices splitting of heart circumference) and radial (16 incrementally-radius rings from endo- to epicardium surface) fibrosis quantization are shown. (C) Spatially quantized fibrosis density is averaged between 7-months age, 13-months age, and all CTRL and DSG2 samples, and finally mapped on a normalized SAX view of a mouse heart (endo: endocardium surface of the left ventricle; epi: epicardium surface; LV and RV: Left (Right) ventricles position).

Next, we applied our tool of spatial investigation previously applied to the local fiber disarray. Results are shown in Figure 43, panel B.

The angular inspection shows that the patchy fibrosis is not uniformly distributed around the LV. Instead, it is concentrated mainly in the left ventricular wall but appears also in the septum. Additionally, radial quantization gives us another interesting insight: fibrosis does not seem normally distributed between the endo- and epicardial wall, but shows a prevalence towards the epicardial surface.

Two-dimensional average maps of the spatial distribution of fibrosis around the LV are shown in Figure 43, panel C. The higher content of patchy fibrosis in DSG2 hearts is evident. On average, five hearts from 7 months old DSG2 mice show accumulated fibrosis in the left ventricular wall and septum; four hearts from 13 months old DSG2 mice, on the other hand, show a marked prevalence in the wall of the LV.

4.3.3 Spatial correlation between fibrosis and fibers disarray

We mapped, quantified, and spatially characterized both the contractile fibers disarray and the fibrotic patches in our whole-heart reconstructions. While the degree of fibers disorganization - *disarray* - appears almost randomly distributed in the cardiac tissue in all CTRL and DSG2 samples, fibrosis is distinctly higher in DSG2 samples, with a high average spatial density in the left ventricular wall. We combined the autofluorescence signal, cytoarchitecture reconstruction, disarray mapping, and fibrosis

segmentation to investigate the potential spatial correlation linking different remodeling processes such as fiber disarray and the occurrence of fibrosis.

In Figure 44, panel A, the proposed multimodal investigation is shown for a representative DSG2 mouse heart. In A1, we combined the high-resolution reconstruction of the myocardium obtained by the autofluorescence signal with the fibrosis map resulting from the scattering images segmentation. As expected, the reconstruction of fibrosis coincides with the absence of cardiac muscle, indicated by the lack of endogenous muscle autofluorescence in that area. In A2, we represented the virtual cytoarchitecture reconstruction of the same heart performed with a spatial resolution of 96 μm . The cytoarchitecture map shows a regular organization of cardiac fibers overall but has large areas (highlighted with asterisks) where the automated tracking software didn't find contractile fibers throughout the entire wall thickness. In A3, the HR fiber architecture reconstruction (A2) was superimposed on the HR tomography of the organ (A1): the absence of orientation vectors perfectly match the presence of fibrosis, confirming the good reliability of the proposed method performing this multimodal structural investigation; moreover, the overall fiber orientations in the border zone of the fibrotic tissue appears coherent with the rest of the myocardium, indicating the lack of fiber disorganization at multicellular level. Finally, in A4, we registered the fiber disarray map evaluated with a spatial resolution of 288 μm with the LR version of the tomography shown in A1. This three-channel representation allows us to qualitative check that fiber disarray appears to be uncorrelated with the presence of big fibrotic patches. The representative sample shows no evidence of fiber structural remodeling in the cardiac muscle caused by the fibrotic tissue formation in such a big area.

This representative result suggests the absence of a spatial correlation between fiber disarray and fibrosis.

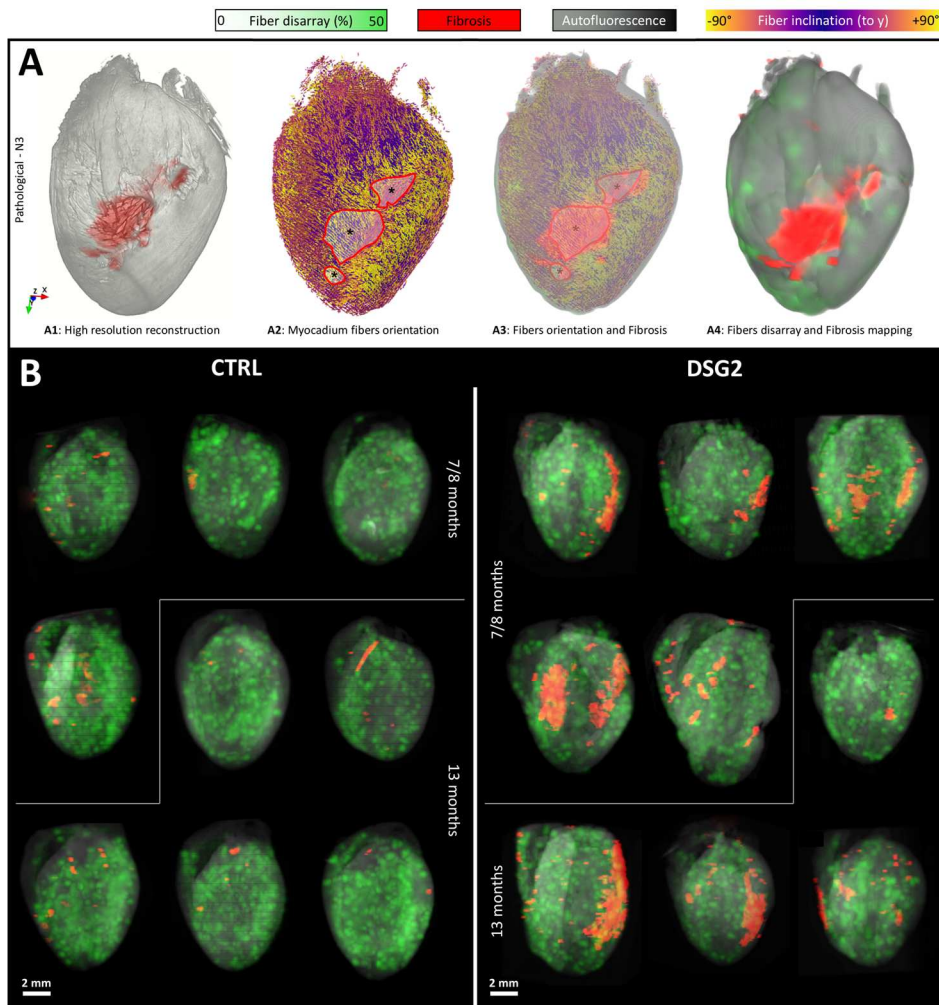


Figure 44: Spatial distribution of fibrosis and fiber disarray in CTRL and DSG2 entire mouse hearts. (A) Multimodal reconstruction of a representative pathological mouse heart is shown: A1 - 3D high-resolution reconstruction of the myocardium (autofluorescence signal, in grey) combined with fibrosis (scattering signal, in red); A2 - map of fiber orientation (estimated with a spatial resolution of 96 μm) with empty areas highlighted (asterisks); A3 - fiber orientation map superimposed on A1, where myocardium without fibers correspond to main fibrotic area; A4 - local fiber disarray (in green, estimated with a spatial resolution of 288 μm) is mapped on the low-resolution version of A1. (B) Three-dimensional Maximum-Intensity-Projection (MIP) of whole heart local fiber disarray (resolution of 288 μm, in green), fibrosis (red) and myocardium autofluorescence (grey) of all CTRL (n=4 of 7/8 months age; n=5 of 13 months age) and pathological (n=5 of 7/8 months age; n=4 of 13 months age) mouse hearts are shown. Fiber disarray appears homogeneous in both CTRL and pathological samples, while pathological samples show big fibrotic patches of tissue.

We applied the proposed method to all CTRL and DSG2 murine hearts, generating a three-dimensional Maximum-Intensity-Profile (3D-MIP) for each sample. Results are collected in Figure 44, panel B. Our tomographies confirm the spatial variability of fibers organization across the organ in both CTRL and DSG2 samples. Patchy fibrosis is evident only in DSG2 samples, with large fibrotic areas condensed principally into the LV wall. Moreover, this overview confirms the apparent lack of correlation between fiber disarray and fibrotic patches.

4.4 Morpho-Functional Correlation

Results of the functional investigation showed heterogeneity of the APP wavefront in hearts from DSG2 mice, as well as a variation of the AP kinetics. On the other hand, the result of the structural investigation on CTRL and DSG2 murine hearts shows that, on average, the disorder of the fibers is variable within the organ, without significant differences between CTRL and DSG2 samples; on the contrary, fibrotic tissue is significantly higher in CTRL mice. Therefore, compared the AP propagation with the fibrosis reconstruction in the LV wall of DSG2 mice hearts.

4.4.1 Alignment of morpho-functional data

We applied the data registration protocol described in section 3.7 to re-align the 2D APP map and the 3D HR tomography of each sample. Figure 45 shows the resume of the procedure applied to a representative DSG2 mouse heart reconstruction.

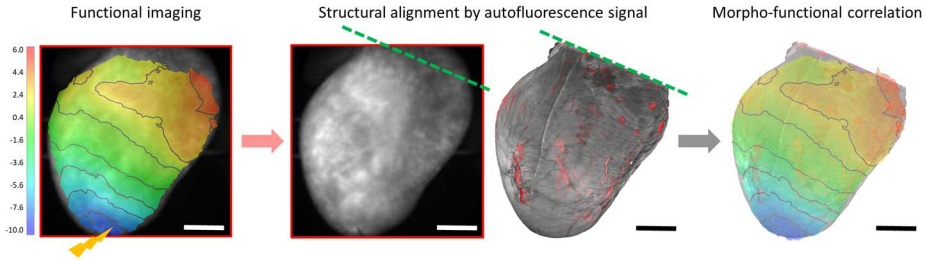


Figure 45: Alignment of morpho-functional data. The alignment procedure developed to register functional data and 3D high-resolution reconstruction of whole-heart murine hearts is schematized. On the left, a representative action-potential propagation (APP) map of a Langendorff-perfused mouse heart stained with a Voltage Sensitive Dye (VSD) and electrically stimulated at the apex (yellow) with a pacing rate of 5 Hz is superimposed on the heart fluorescence image. The same heart was cleared with SHIELD protocol and reconstructed with the MesoSPIM, and the 3d high-resolution tomography (where green dashed line represents the limit of the microscope field of view) was aligned to the fluorescence image of the optical mapping data. On the right, the result of the morpho-functional data registration: the 2D APP map is superimposed to the structural reconstruction. Scale bars: 2mm.

The proposed images correlation technique appears capable of correctly generating morpho-functional maps of the entire heart. The 2D map of the APP, generated by analyzing the electrical activation in the LV, perfectly matches the 3D reconstruction of the same sample obtained after the clearing-imaging process.

4.4.2 Fibrosis impacts on AP propagation

Morpho-functional maps of the LV were generated for all DSG2 mice hearts, superimposing AP propagation maps and fibrosis MIPs. Results are shown in Figure 46.

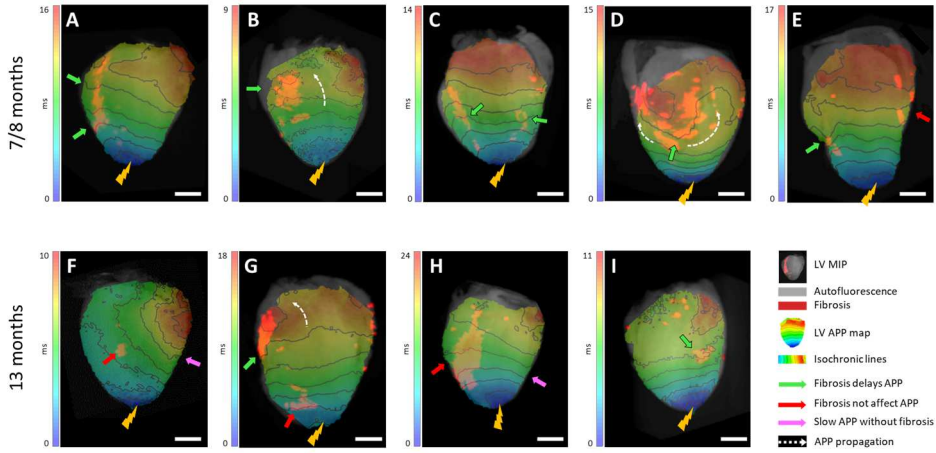


Figure 46: Morpho-functional correlation of fibrosis and action potential propagation in the left ventricle of DSG2 mouse hearts. Left-ventricle (LV) action potential propagation (APP) was detected by our optical mapping platform during an electrical stimulation at the apex of the DSG2 mouse hearts with a pacing rate of 5Hz. The APP maps are superimposed over left-ventricle (LV) dual-channel maximum intensity projections (MIPs) of myocardium autofluorescence (grey) and fibrotic-related scattering signal (red) of whole-heart reconstructions previously aligned with functional data. We found that APP wavefront distortion appears correlated with fibrosis patches (green arrows) in panels A-E, G, and I, showing local delays (A, C, E, I) and big deviations (dashed white arrows in panels B, D, and G). On the contrary, examples showing an APP not correlated with the position of the connective tissue are in panels E-H, where the electrical signal appears not affected by fibrosis (red arrows) or shows delay without evidence of fibrotic tissue (violet arrows). Scale bars: 2mm.

We found that the distortion of the APP wavefront detected on the LV wall appears correlated with the presence of fibrotic patches in the ventricular wall in seven DSG2 mice (panels A-E, G, I). Local distortions of the APP wavefront were observed in the proximity of fibrotic patches (green arrows in panels A, C, E, G, and I), where the optical mapping system detected a local delay of the electrical activation of the tissue located directly behind the fibrotic patch. In addition, we found a considerable distortion of the APP wavefront (dashed white arrows) around large fibrotic patches (panels B, D, and G).

However, we also found cases where APP wavefront distortion was completely uncorrelated to fibrotic tissue presence. For example, the APP

seems to be unaffected by the presence of fibrosis in four cases (panels E-H), where the electrical signal propagates undisturbed over fibrosis patches (red arrows). Peculiarly, in two samples we detected a slowing of the APP without evidence of fibrotic tissue (violet arrows in panels F and H).

In conclusion, AP propagation appeared to be correlated with the presence of fibrotic tissue patches, even if the only presence of fibrosis doesn't explain APP wavefront distortion in all cases.

5 Discussion and Conclusion

During my Ph.D. course, we developed a full-optics novel experimental workflow able to integrate functional and structural investigations performed at high resolution on entire mouse hearts in physiological and pathophysiological conditions. We first characterized the action potential propagation of the isolated heart exploiting optical mapping and we next reconstructed the three-dimensional anatomy of the same organ with micrometric resolution, to analyze myocardium fiber organization and fibrotic tissue deposition. Finally, by integrating these functional and structural studies, we provide a one-to-one correlative morpho-functional investigation.

While cardiac optical mapping is a well-established technique to characterize the electrical activity in Langerdoff perfused hearts, to date reconstructing entire mouse hearts with micrometric resolution through currently available optical methods is challenging. To date, the most efficient way to perform mesoscopic imaging by optical methods is by employing tissue clearing protocols to make the samples transparent, but these techniques are time-consuming and typically introduce tissue degradation or deformation. Therefore we put great effort to establish a tissue transformation protocol able to make whole mouse hearts optically transparent, and simultaneously ensure tissue preservation. We found that the SHIELD protocol carefully optimized for cardiac tissue required many months of treatment for each heart, but produces excellent results in both tissue clearing and preservation. Entire mouse hearts became almost completely transparent, while macroscopically intact in terms of tissue robustness and rigidity. Additionally, histological investigations confirmed the excellent tissue preservation at a micrometric scale.

Once an optically transparent and well-preserved mouse heart was obtained, performing mesoscopic investigations with micrometer resolution and in a reasonable time required to exploit the latest advances in optical imaging. For this purpose, axial-scanning light-sheet microscopy (ASLM) is currently the most efficient technique. In this project, we decided to pursue a new

generation of ASLM: the MesoSPIM initiative. MesoSPIM combines the advantages of dual-arm excitation, a dynamically generated light-sheet, and an innovative excitation/detection system based on synchronization between the axial scanning and sensor shutter. In addition, during the development of the system we combined the axial scanning technology with a new generation of detection path, using the Kinetix sCMOS Camera coupled with an effective telecentric lens designed ad-hoc. This technological effort allowed us to optimize the imaging performance of the microscope, achieving the capability to image a FOV of more than 1 square centimeter with a pixel size of $3.25\text{ }\mu\text{m} \times 3.25\text{ }\mu\text{m}$, with high sensitivity and almost zero field distortion. While the autofluorescence of muscle tissue can be used to visualize myocardium by collecting red wavelengths, we employed the higher RI of connective tissue to detect collagen by collecting elastically scattered light. This approach results in a label-free imaging protocol capable of reconstructing both myocardium and fibrosis. This solution combined with the MesoSPIM performance allowed the generation of a three-dimensional tomography of a whole cleared mouse heart including both autofluorescence and scattering signals at high resolution (HR) in approximately forty minutes. Three-dimensional tomographies were analyzed by using custom software tools able to detect, reassemble, and analyze the three-dimensional orientation of each contractile fiber of the heart, generating a 3D virtual representation of the entire architecture of the cardiac muscle where fiber disarray can be evaluated. By combining three-dimensional maps of fiber disarray and fibrotic tissue segmentation, we successfully generated a 3D comprehensive reconstruction of the heart anatomy at HR. Finally, we concentrated our efforts to find an effective method to merge functional and structural data by comparing APP map and 3D reconstruction, providing a true correlative morpho-functional investigation protocol.

We applied the outlined investigation on the Desmoglein-2^{mut/mut} (DSG2) mouse model presenting an ACM phenotype, which was provided thanks to the fruitful collaboration with Prof. Marco Mongillo and Dr. Tania Zaglia

from the University of Padua. This model shows a strong susceptibility to arrhythmogenic events and fibrotic remodeling at the RV wall which with increasing age also affects the LV. We studied nine CTRL mice (four at age 7 months and five at 13 months of age) and nine DSG2 mice (five at 7 months and four at 13 months).

Functional analyses revealed a variation of AP kinetics between the two groups, as both delayed depolarization and increased repolarization time were observed in DSG2 hearts. Both average value and dispersion of the TTP across the ventricle are significantly higher in DSG2 hearts at all stimulation frequencies at age 13 months suggesting an alteration of cell-to-cell electrical coupling or impairment of sodium current in the DSG2 model. In addition, we observed a tendency of an altered repolarization time in DSG2 mouse hearts, with AP prolongation at 50% (APD₅₀) and 90% (APD₉₀) at age 7 and 13 months and at all stimulation frequencies, although these differences were not statistically significant. These results indicate a mild remodeling of repolarizing currents in DSG2 mouse hearts. The more striking result from the functional analysis was the increased APP wavefront dispersion found at 7 months of age (as a trend) and 13 months of age (statistically significant) in DSG2 mice, while no significant differences in local CV were observed. The evident irregularity of APP propagation wavefronts observed in DSG2 mice could suggest macroscopical differences in the LV wall. Indeed, the AP conduction wavefront can be distorted by the presence of fibrotic tissue, disrupted arrangement of muscle fiber bundles, and the anatomical shape of the LV wall. On the other hand, unaltered local CV appears in contrast with the prolongation of TTP found in the DSG2 model. In this context, further investigations on the single-cardiomyocyte electro-physiology would be important to better explain variations of AP dynamics found in DSG2 hearts.

In addition to these finds, we also observed a higher susceptibility of DSG2 hearts to triggering arrhythmias. Notably, while the number of arrhythmic events per second was significantly higher in DSG2 mice, with a similar

average duration between the two groups, we found a longer cycle length of the arrhythmias recorded in pathological hearts. With a comparable CV found in CTRL and DSG2 mice, a longer cycle length could be explained by the presence of anatomical obstacles (fibrotic area for example) that increase the path length of the rotor.

Based on these results, we applied the proposed structural investigation protocol on all CTRL and DSG2 mouse hearts, focusing on quantifying myocardium hypertrophy, fibers disarray, and the presence of fibrosis.

Three-dimensional anatomical measurements performed on the myocardium revealed no differences in muscle tissue and LV chamber volumes between DSG2 and CTRL mouse hearts at any mice ages, suggesting a lack of hypertrophy or LV chamber dilation (Figure 34). Consistently, the average LV wall thickness in base, mid-cavity, and apex appears comparable between the two groups. On the other hand, we found a statistically significant increase of angular variability of the LV wall thickness in mid-cavity and apex in DSG2 hearts at any age. More precisely, we observed degeneration of LV wall thickness prevalently near M3-M4 and A2 in mid-cavity and apical segments respectively. This result suggests the presence of a sort of remodeling process occurring in the LV wall in DSG2 mouse hearts, potentially caused by the fibrotic replacement of contractile tissue.

Further, we quantified the degree of alignment of contractile fibers in all samples. As explained in section 4.3.1.2, we performed this investigation with a spatial resolution of 288 μm to avoid the contribution of macroscopical structures affecting the results, and even more important, to obtain information about the alignment of the fibers in a spatial scale consistent with the CV analysis (312 μm). We found comparable cardiac fiber disarray in CTRL and DSG2 mice at any age (Figure 41). Distributions of disarray values appear very similar between groups and ages, and no statistically significant differences were detected. This finding is consistent with functional data: at the same spatial, we were unable to detect any

variation between DSG2 and CTRL mice, neither in CV nor in alignment degree of cardiomyocytes. Although consistent with functional data, this structural finding is quite surprising considering that the DSG2 mutation could affect cellular alignment. In this respect, additional investigations focused to assess the organization of the tissue at the single-cell level would be very useful.

On the other hand, in DSG2 mouse hearts we found a significantly higher amount of fibrosis compared to CTRLs, at any age. Moreover, we found that fibrotic tissue patches are concentrated on average in the LV wall, but it is still present as well as in the RV wall and, in general, the distribution of collagen depositions in the LV cardiac wall is unbalanced through the epicardial surface.

All these characteristics are in line with the mutation present in the murine model involved in this study: a fibrotic remodeling present in the RV but involving also LV with aging, starting from the epicardium, and characterized by a thinning of the myocardium walls replaced by fibrosis. Finally, thanks to our integrated reconstructions where fiber disarray and fibrosis are superimposed, we had not found evidence of a spatial correlation between fiber disarray and border zones of fibrotic patches.

In conclusion, our structural investigation shows that fiber arrangement at a multi-cellular scale is not affected by the mutation, while we found a strong prevalence of fibrotic tissue in DSG2 mice coupled with a variability of the LV wall thickness. In addition, fiber disarray is almost homogeneous around the LV, and it is not affected by the presence of fibrosis.

Taking these results into account, we aligned our morpho-functional data using activation maps and fibrosis reconstructions of the LV to investigate the APP wavefront distortion that we found in DSG2 mice (Figure 46).

We found that in some cases we can assess the impact of fibrotic tissue on the APP wavefront. For example, where big fibrotic tissue patches prevent

the propagation of the AP, deviating the wavefront at the macroscopical level. Moreover, we can observe small fibrosis able to locally delay the conduction, resulting in APP wavefront showing little distortion around the fibrosis. By this correlative approach, we can directly observe the impact of 3D structural features on cardiac electrical activity, and observations show the expected impact of fibrotic tissue on the APP.

We also found cases where fibrosis doesn't affect the APP, or where the wavefront appears disrupted or curved without evidence of collagen depositions. This could be explained by taking into account other structural features. For example, we expect that irregularities of the LV wall thickness we found in DSG2 hearts can impact the APP wavefront: a thinning or thickening of the myocardium wall can deflect the wavefront of the depolarization current, up to resulting in conduction blocks (91, 92). Another important factor to consider is the position, and the geometry, of fibrotic tissue patches into the myocardial wall, especially combined with the wall thickness (93). In fact, we expected that a patch of connective tissue, even if small, will have an enormous impact on AP propagation if it involves the entire section of the ventricular wall, especially when the latter is compromised. In contrast, even larger collagen depositions placed on the endo- or epicardium of areas with an unaltered ventricular wall thickness, would have less impact on electrical propagation within the myocardial wall. Moreover, cardiac remodeling includes diffuse interstitial fibrosis as well as focal replacement fibrosis. In this context, the variable density of the collagen deposition in the myocardial wall can modify locally the electrical propagation velocity, generating a curvature of the APP without the presence of clearly visible fibrotic structures and resulting thus as an important arrhythmogenic factor (94). Finally, the fiber organization of the myocardium has to be further investigated. Indeed, although we did not observe variation between fiber disarray distribution in CTRL and DSG2 mice hearts, other geometrical features could affect APP, e.g. fibers sheets deformation and disrupted trabeculation (95).

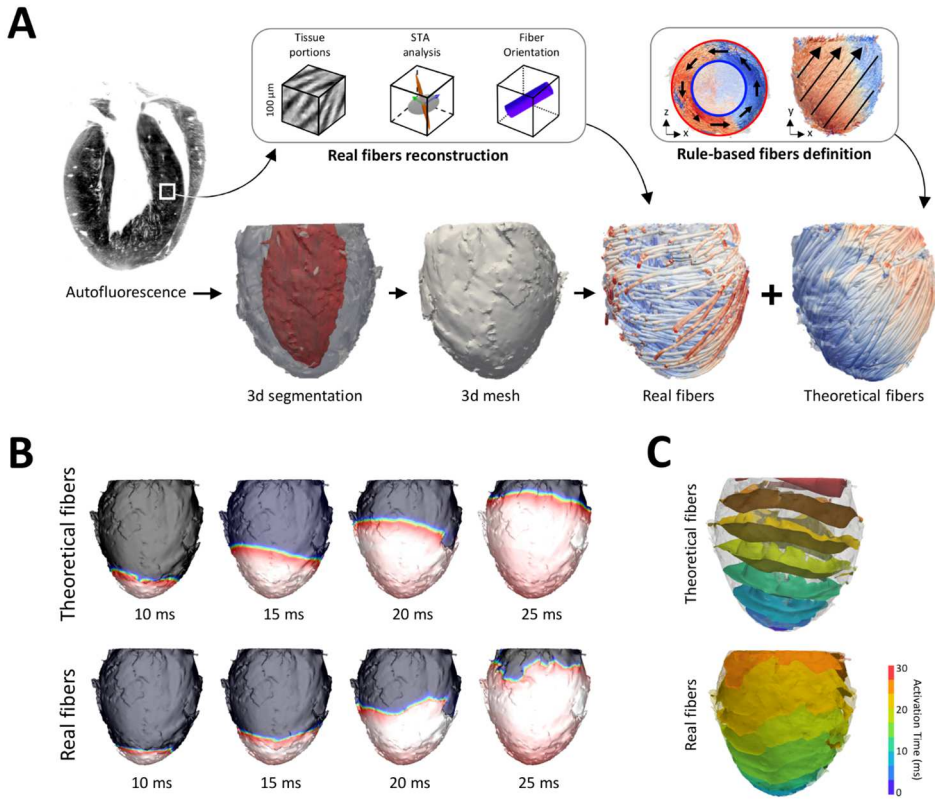


Figure 47: Electrophysiology computational modeling based on integrated cytoarchitectonic reconstruction. (A) Cytoarchitectonic reconstruction pipeline of the ventricular myocardium. On the left, a representative autofluorescence section of an entire mouse heart obtained with MesoSPIM and, on top, the pipeline of fibers orientation analysis. Image-based generation of the 3D finite elements mesh allow to map the fibers architecture on the 3D high-resolved anatomy of the heart. Rule-based theoretical fibers orientations are created as control. (B) An apex pacing protocol is simulated using an accurate model of Action Potential Propagation (APP) integrating the fibers architectures. Differences between real and theoretical fibers are clear. (C) The 3D maps of APP wavefronts of (B) are shown. This accurate representation will allow us to understand the actual impact of the structures composing the myocardium wall on the APP wavefronts.

These hypotheses could be tested employing computational modeling of AP propagation in whole-heart three-dimensional models (96, 97). In this direction, we already performed preliminary methodological efforts on an LV

mouse heart reconstruction where we assessed fibers orientation with a spatial resolution of about 100 μ m (Figure 47).

In particular, we employed high-resolution images of muscle autofluorescence to create a three-dimensional segmentation of the myocardium, from which we then generated a three-dimensional finite element mesh. Fiber orientations were mapped over the mesh to reconstruct the conduction pathways of the tissue and, in parallel, a rule-based theoretical fibers architecture was created as control (Figure 47, panel A) (95). A model of APP was integrated into the 3D architecture to simulate the electrical activity of the heart. Apical pacing protocols were simulated (Figure 47, panel B) and the 3D APP wavefronts were calculated and represented over the whole ventricle mesh (Figure 47, panel C). We found differences in the APP wavefront when including real or theoretical fibers. These preliminary results show the feasibility of integrating our structural reconstruction into reliable computational models and, more importantly, confirm that a computational approach can benefit the investigation of the role of each structural feature in APP propagation (98).

This approach could be further improved including in the computational model other structural information like diffuse fibrosis, connexin distribution, and cell-to-cell coupling by employing high-resolution immuno-histochemical imaging in a selected portion of tissue. Assembling all these functional and structural information in a high-resolution integrated model will provide a reliable tool to better characterize how structural features are triggering arrhythmic events in this DSG2 mouse model and more in general opening the way for generating integrated predictive models of healthy and pathological conditions.

6 Glossary

4C: Four Chambers (view)

ACM: Arrhythmogenic Cardiomyopathy

AHA: American Heart Association

ANOVA: Analysis Of Variance

AP: Action Potential

APD: Action Potential Duration

APP: Action Potential Propagation

ASLM: Axially Scanned Light-Sheet Microscopy

AV: Atrio-Ventricular

CCD: Charge-Coupled Devices

CTRL: Control

CV: Coefficient of Variation

CV: Conduction Velocity

DSG2: Desmoglein-2^{mut/mut} (or Desmoglein-2^{+/+})

ECG: Electrocardiogram

ECM: Extra-Cellular Matrix

ETL Electrically Tunable polymeric Lens

FA: Fractional Anisotropy

FOV: Field Of View

FV: Fibrosis Volume

HR: High Resolution

KH: Krebs-Henseleit

LAX: Long Axis (view)

LPF: Long-Pass Filter

LR: Low Resolution

LSFM: Light-Sheet Fluorescence Microscopy

LV: Left Ventricle

MIP: Maximum Intensity Projection

MV: Myocardium Volume

NA: Numerical Aperture

PF: Percentage of Fibrosis

PFA: Paraformaldehyde

RI: Refractive Index

RV: Right Ventricle

RVOT: Right Ventricular Outflow Tract

SA: Sinoatrial

SAX: Short Axis (view)

sCMOS: Scientific Complementary Metal-Oxide-Semiconductor

SDS: Sodium Dodecyl Sulphate

SHIELD: Stabilization to Harsh conditions via Intramolecular Epoxide Linkages to prevent Degradation

SN: Sinus Node

SR: Sinus Rhythm

STA: Structure Tensor Analysis

TDE: 2,2'-Thiodiethanol

TTP: Time to Peak

VSD: Voltage Sensitive Dye

WD: Wavefront Dispersion

7 Table of Figures

Figure 1: Cardiac anatomy.....	6
Figure 2: Section of the cardiac wall.	7
Figure 3: Cardiomyocyte.....	8
Figure 4: Cardiac conduction system.	10
Figure 5: Phases of the membrane action potential.	13
Figure 6: Action potential of a peacemaker cell.....	15
Figure 7: Schematization of ECG traces of SR and different cardiac rhythms.....	18
Figure 8: Scheme of a reentrant circuit.....	19
Figure 9: Cardiac remodeling in pathology.	22
Figure 10: Optical mapping setup and data acquisition.....	29
Figure 11: Histological imaging of contractile human heart tissue.....	31
Figure 12: Schematic representation of light scattering before and after an optical clearing process.....	33
Figure 13: Light-sheet fluorescence microscope	37
Figure 14: Gaussian profile.	38
Figure 15: MesoSPIM rolling shutter mechanism.....	39
Figure 16: Picture of the mouse heart retrogradely perfused with Langendorff system.	43
Figure 17: Scheme of the wide-field fluorescence mesoscope.	44
Figure 18: Scheme of the SHIELD protocol.	47
Figure 19: MesoSPIM optical scheme.....	49
Figure 20: MesoSPIM setup.	50
Figure 21: Performance of detection path.	51
Figure 22: MesoSPIM light-sheet generation.....	52
Figure 23 : Sample imaging and image preprocessing.	55

Figure 24: Three-dimensional fiber disarray quantification in entire mouse heart reconstruction.	61
Figure 25: Automatic spatial quantization of 3d data around LV wall.....	64
Figure 26: Automatic rotation of mouse heart tomographies for morpho-functional maps correlation.	66
Figure 27: Action potential kinetics in CTRL and a DSG2 mouse hearts.	71
Figure 28: Conduction velocity in CTRL and a DSG2 mouse hearts.	72
Figure 29: Arrhythmia episode in DSG2 mouse heart.....	74
Figure 30: Arrhythmia analysis in CTRL and DSG2 mouse hearts.....	75
Figure 31: Clarified tissue preservation.....	76
Figure 32: MesoSPIM tomography of a cleared murine heart.....	78
Figure 33: Mouse whole heart reconstruction.....	79
Figure 34: Results of myocardium anatomical investigation.	81
Figure 35: Resolving contractile fibers in the entire heart.	83
Figure 36: Comparison of the same cardiac section of a mouse affected by arrhythmogenic cardiomyopathy.....	85
Figure 37: Scattering signal independency from excitation direction.	86
Figure 38: Whole-heart three-dimensional fiber orientation mapping.	89
Figure 39: Whole heart cytoarchitecture reconstruction.	91
Figure 40: Myocardium local fibers disarray in entire mouse heart reconstructions.	93
Figure 41: Myocardium fiber disarray distributions in CTRL and DSG2 mouse hearts.	95
Figure 42: Spatial distribution of fiber disarray on CTRL and DSG2 mice.	97
Figure 43: Quantification of fibrotic tissue.....	99
Figure 44: Spatial distribution of fibrosis and fiber disarray in CTRL and DSG2 entire mouse hearts.....	102
Figure 45: Alignment of morpho-functional data.	104
Figure 46: Morpho-functional correlation of fibrosis and action potential propagation in the left ventricle of DSG2 mouse hearts.	105

Figure 47: Electrophysiology computational modeling based on integrated cytoarchitectonic reconstruction.	114
---	-----

Bibliography

1. Blausen.com. Medical gallery of Blausen Medical 2014. WikiJournal of Medicine. 2014;1(2).
2. Anastasi G, Capitani S. Trattato di anatomia umana: Edi-Ermes; 2012.
3. www.cardio-research.com/cardiomycytes
4. Racugno P, Callejo Crespo D. Cardiologia e chirurgia vascolare - Manuale CTO. 4th ed, 2019.
5. Netter FHBAM. Atlante di anatomia umana. Milano: Edra; 2014.
6. D'Angelo E, Peres A. Fisiologia. 3th ed, 2020.
7. Katz AM. Physiology of the heart. 4th ed. Philadelphia: Lippincott Williams & Wilkins; 2006. xix, 644 pages
8. Silverthorn DU. Human physiology : an integrated approach. San Francisco: Pearson/Benjamin Cummings;; 2010.
9. Klabunde RE. Cardiac electrophysiology: normal and ischemic ionic currents and the ECG. Adv Physiol Educ. 2017;41(1):29-37.
10. Hall JE, Guyton AC. Guyton and Hall textbook of medical physiology. 12th ed. Philadelphia: Saunders/Elsevier; 2011. 1091 p.
11. <https://en.wikipedia.org/wiki/File:SinusRhythmLabels.png>.
12. Database M-BMVA. Human ECGs, records #426. MIT-BIH Malignant Ventricular Arrhythmia Database.
13. Mines GR. On dynamic equilibrium in the heart. J Physiol. 1913;46(4-5):349-83.
14. Cherry EM, Fenton FH. Visualization of spiral and scroll waves in simulated and experimental cardiac tissue. New J Phys. 2008;10(12):125016.
15. Stevenson WG, Delacretaz E. Strategies for catheter ablation of scar-related ventricular tachycardia. Curr Cardiol Rep. 2000;2(6):537-44.
16. Gaggin HK, Dec GW. Pathophysiology of Heart Failure. In: Education M-H, editor. The Heart2017.

17. Chinnaiyan KM, Alexander D, Maddens M, McCullough PA. Curriculum in cardiology: integrated diagnosis and management of diastolic heart failure. *Am Heart J*. 2007;153(2):189-200.
18. Krumholz HM, Larson M, Levy D. Prognosis of left ventricular geometric patterns in the Framingham Heart Study. *J Am Coll Cardiol*. 1995;25(4):879-84.
19. Grant C, Greene DG, Bunnell IL. Left ventricular enlargement and hypertrophy. A clinical and angiocardiographic study. *Am J Med*. 1965;39(6):895-904.
20. Ho CY. Hypertrophic cardiomyopathy. *Heart Fail Clin*. 2010;6(2):141-59.
21. F. C. Post-necrotic left ventricular remodeling. *Trends in Medicine*. 2004;4(2):10.
22. Mann DL. Heart failure : a companion to Braunwald's heart disease. 2nd ed. St. Louis: Elsevier/Saunders; 2011. xix, 902 pages p.
23. Leonard BL, Smaill BH, LeGrice IJ. Structural remodeling and mechanical function in heart failure. *Microsc Microanal*. 2012;18(1):50-67.
24. Mann DL, Bristow MR. Mechanisms and models in heart failure: the biomechanical model and beyond. *Circulation*. 2005;111(21):2837-49.
25. Spinale FG. Matrix metalloproteinases: regulation and dysregulation in the failing heart. *Circ Res*. 2002;90(5):520-30.
26. de Boer RA, De Keulenaer G, Bauersachs J, Brutsaert D, Cleland JG, Diez J, et al. Towards better definition, quantification and treatment of fibrosis in heart failure. A scientific roadmap by the Committee of Translational Research of the Heart Failure Association (HFA) of the European Society of Cardiology. *Eur J Heart Fail*. 2019;21(3):272-85.
27. Basso C, Baucé B, Corrado D, Thiene G. Pathophysiology of arrhythmogenic cardiomyopathy. *Nat Rev Cardiol*. 2011;9(4):223-33.
28. Norman M, Simpson M, Mogensen J, Shaw A, Hughes S, Syrris P, et al. Novel mutation in desmoplakin causes arrhythmogenic left ventricular cardiomyopathy. *Circulation*. 2005;112(5):636-42.
29. Sen-Chowdhry S, Syrris P, Ward D, Asimaki A, Sevdalis E, McKenna WJ. Clinical and genetic characterization of families with

- arrhythmogenic right ventricular dysplasia/cardiomyopathy provides novel insights into patterns of disease expression. *Circulation*. 2007;115(13):1710-20.
30. Basso C, Corrado D, Marcus FI, Nava A, Thiene G. Arrhythmogenic right ventricular cardiomyopathy. *Lancet*. 2009;373(9671):1289-300.
 31. Agullo-Pascual E, Cerrone M, Delmar M. Arrhythmogenic cardiomyopathy and Brugada syndrome: diseases of the connexome. *FEBS Lett*. 2014;588(8):1322-30.
 32. Delmar M, McKenna WJ. The cardiac desmosome and arrhythmogenic cardiomyopathies: from gene to disease. *Circ Res*. 2010;107(6):700-14.
 33. Groeneweg JA, Bhonsale A, James CA, te Riele AS, Dooijes D, Tichnell C, et al. Clinical Presentation, Long-Term Follow-Up, and Outcomes of 1001 Arrhythmogenic Right Ventricular Dysplasia/Cardiomyopathy Patients and Family Members. *Circ Cardiovasc Genet*. 2015;8(3):437-46.
 34. Chelko SP, Asimaki A, Andersen P, Bedja D, Amat-Alarcon N, DeMazumder D, et al. Central role for GSK3 β in the pathogenesis of arrhythmogenic cardiomyopathy. *JCI Insight*. 2016;1(5):e85923.
 35. Chelko SP, Asimaki A, Lowenthal J, Bueno-Beti C, Bedja D, Scalco A, et al. Therapeutic Modulation of the Immune Response in Arrhythmogenic Cardiomyopathy. *Circulation*. 2019;140(18):1491-505.
 36. Awad MM, Dalal D, Cho E, Amat-Alarcon N, James C, Tichnell C, et al. DSG2 mutations contribute to arrhythmogenic right ventricular dysplasia/cardiomyopathy. *Am J Hum Genet*. 2006;79(1):136-42.
 37. Bauce B, Nava A, Beffagna G, Basso C, Lorenzon A, Smaniotto G, et al. Multiple mutations in desmosomal proteins encoding genes in arrhythmogenic right ventricular cardiomyopathy/dysplasia. *Heart Rhythm*. 2010;7(1):22-9.
 38. Pilichou K, Nava A, Basso C, Beffagna G, Bauce B, Lorenzon A, et al. Mutations in desmoglein-2 gene are associated with arrhythmogenic right ventricular cardiomyopathy. *Circulation*. 2006;113(9):1171-9.
 39. Syrris P, Ward D, Asimaki A, Evans A, Sen-Chowdhry S, Hughes SE, et al. Desmoglein-2 mutations in arrhythmogenic right ventricular

- cardiomyopathy: a genotype-phenotype characterization of familial disease. *Eur Heart J*. 2007;28(5):581-8.
40. Davila HV, Salzberg BM, Cohen LB, Waggoner AS. A large change in axon fluorescence that provides a promising method for measuring membrane potential. *Nat New Biol*. 1973;241(109):159-60.
 41. Laughner JI, Ng FS, Sulkin MS, Arthur RM, Efimov IR. Processing and analysis of cardiac optical mapping data obtained with potentiometric dyes. *American journal of physiology Heart and circulatory physiology*. 2012;303(7):H753-65.
 42. Efimov IR, Nikolski VP, Salama G. Optical imaging of the heart. *Circulation research*. 2004;95(1):21-33.
 43. Gray RA, Pertsov AM, Jalife J. Spatial and temporal organization during cardiac fibrillation. *Nature*. 1998;392(6671):75-8.
 44. Franceschini A, Costantini I, Pavone FS, Silvestri L. Dissecting Neuronal Activation on a Brain-Wide Scale With Immediate Early Genes. *Front Neurosci*. 2020;14:569517.
 45. De Santanna A. *Histology Atlas*: University of Genova; 2021.
 46. Bisen PS. *Laboratory protocols in applied life sciences* 2014. 1 online resource (1772 pages) p.
 47. Kao F-J, Keiser G, Gogoi A. *Advanced Optical Methods for Brain Imaging*. Singapore: Springer; 2019. Available from: <https://libproxy.mst.edu/login?url=https://link.springer.com/openurl?genre=book&isbn=978-981-10-9020-2>.
 48. Richardson DS, Lichtman JW. Clarifying Tissue Clearing. *Cell*. 2015;162(2):246-57.
 49. Dodt HU, Leischner U, Schierloh A, Jahrling N, Mauch CP, Deininger K, et al. Ultramicroscopy: three-dimensional visualization of neuronal networks in the whole mouse brain. *Nat Methods*. 2007;4(4):331-6.
 50. Erturk A, Becker K, Jahrling N, Mauch CP, Hojer CD, Egen JG, et al. Three-dimensional imaging of solvent-cleared organs using 3DISCO. *Nat Protoc*. 2012;7(11):1983-95.
 51. Renier N, Wu Z, Simon DJ, Yang J, Ariel P, Tessier-Lavigne M. iDISCO: a simple, rapid method to immunolabel large tissue samples for volume imaging. *Cell*. 2014;159(4):896-910.

52. Costantini I, Ghobril J-P, Di Giovanna AP, Mascaro ALA, Silvestri L, Müllenbroich MC, et al. A versatile clearing agent for multi-modal brain imaging. *Scientific Reports*. 2015;5(1):9808.
53. Ke MT, Fujimoto S, Imai T. SeeDB: a simple and morphology-preserving optical clearing agent for neuronal circuit reconstruction. *Nat Neurosci*. 2013;16(8):1154-61.
54. Kuwajima T, Sitko AA, Bhansali P, Jurgens C, Guido W, Mason C. ClearT: a detergent- and solvent-free clearing method for neuronal and non-neuronal tissue. *Development*. 2013;140(6):1364-8.
55. Chung K, Wallace J, Kim SY, Kalyanasundaram S, Andalman AS, Davidson TJ, et al. Structural and molecular interrogation of intact biological systems. *Nature*. 2013;497(7449):332-7.
56. Olianti C, Giardini F, Lazzeri E, Costantini I, Silvestri L, Coppini R, et al. Optical clearing in cardiac imaging: A comparative study. *Prog Biophys Mol Biol*. 2022;168:10-7.
57. Park YG, Sohn CH, Chen R, McCue M, Yun DH, Drummond GT, et al. Protection of tissue physicochemical properties using polyfunctional crosslinkers. *Nat Biotechnol*. 2018.
58. Krieger J. Prinzip eines SPIM-Mikroskops. www.wikipedia.org.
59. Dean KM, Roudot P, Welf ES, Danuser G, Fiolka R. Deconvolution-free Subcellular Imaging with Axially Swept Light Sheet Microscopy. *Biophys J*. 2015;108(12):2807-15.
60. www.mesospim.org.
61. Voigt FF, Kirschenbaum D, Platonova E, Pages S, Campbell RAA, Kastli R, et al. The mesoSPIM initiative: open-source light-sheet microscopes for imaging cleared tissue. *Nat Methods*. 2019;16(11):1105-8.
62. Matiukas A, Mitrea BG, Qin M, Pertsov AM, Shvedko AG, Warren MD, et al. Near-infrared voltage-sensitive fluorescent dyes optimized for optical mapping in blood-perfused myocardium. *Heart Rhythm*. 2007;4(11):1441-51.
63. Giardini F, Biasci V, Scardigli M, Pavone FS, Bub G, Sacconi L. A Software Architecture to Mimic a Ventricular Tachycardia in Intact

- Murine Hearts by Means of an All-Optical Platform. *Methods and protocols*. 2019;2(1).
64. Scardigli M, Mullenbroich C, Margoni E, Cannazzaro S, Crocini C, Ferrantini C, et al. Real-time optical manipulation of cardiac conduction in intact hearts. *J Physiol*. 2018;596(17):3841-58.
 65. Myburgh DP, Lewis BS. Ventricular parasystole in healthy hearts. *Am Heart J*. 1971;82(3):307-11.
 66. Giardini F, Lazzeri E, Olianti C, Beconi G, Costantini I, Silvestri L, et al. Mesoscopic Optical Imaging of Whole Mouse Heart. *J Vis Exp*. 2021(176).
 67. Schneider CA, Rasband WS, Eliceiri KW. NIH Image to ImageJ: 25 years of image analysis. *Nat Methods*. 2012;9(7):671-5.
 68. Schindelin J, Arganda-Carreras I, Frise E, Kaynig V, Longair M, Pietzsch T, et al. Fiji: an open-source platform for biological-image analysis. *Nat Methods*. 2012;9(7):676-82.
 69. Fernandez R, Moisy C. FijiYama: a registration tool for 3D multimodal time-lapse imaging. *Bioinformatics*. 2021;37(10):1482-4.
 70. Ourselin S, Roche A, Prima S, Ayache N, editors. *Block Matching: A General Framework to Improve Robustness of Rigid Registration of Medical Images*. *Medical Image Computing and Computer-Assisted Intervention – MICCAI 2000*; 2000 2000//; Berlin, Heidelberg: Springer Berlin Heidelberg.
 71. Cerqueira MD, Weissman NJ, Dilsizian V, Jacobs AK, Kaul S, Laskey WK, et al. Standardized myocardial segmentation and nomenclature for tomographic imaging of the heart. A statement for healthcare professionals from the Cardiac Imaging Committee of the Council on Clinical Cardiology of the American Heart Association. *Circulation*. 2002;105(4):539-42.
 72. Harris CR, Millman KJ, van der Walt SJ, Gommers R, Virtanen P, Cournapeau D, et al. Array programming with NumPy. *Nature*. 2020;585(7825):357-62.
 73. Virtanen P, Gommers R, Oliphant TE, Haberland M, Reddy T, Cournapeau D, et al. SciPy 1.0: fundamental algorithms for scientific computing in Python. *Nature Methods*. 2020;17(3):261-72.

74. Pedregosa F, Varoquaux G, Gramfort A, Michel V, Thirion B, Grisel O, et al. Scikit-learn: Machine Learning in Python. *Journal of Machine Learning Research*. 2011;12:5.
75. van der Walt S, Schönberger JL, Nunez-Iglesias J, Boulogne F, Warner JD, Yager N, et al. scikit-image: image processing in Python. *PeerJ*. 2014;2:e453.
76. Bradski G. The OpenCV Library. *Dr Dobb's Journal of Software Tools*.
77. Olianti C, Costantini I, Giardini F, Lazzeri E, Crocini C, Ferrantini C, et al. 3D imaging and morphometry of the heart capillary system in spontaneously hypertensive rats and normotensive controls. *Sci Rep*. 2020;10(1):14276.
78. Costantini I, Baria E, Sorelli M, Matuschke F, Giardini F, Menzel M, et al. Autofluorescence enhancement for label-free imaging of myelinated fibers in mammalian brains. *Sci Rep*. 2021;11(1):8038.
79. Basser PJ, Pierpaoli C. Microstructural and physiological features of tissues elucidated by quantitative-diffusion-tensor MRI. *J Magn Reson B*. 1996;111(3):209-19.
80. Ozarslan E, Vemuri BC, Mareci TH. Generalized scalar measures for diffusion MRI using trace, variance, and entropy. *Magn Reson Med*. 2005;53(4):866-76.
81. Giardini F, Lazzeri E, Vitale G, Ferrantini C, Costantini I, Pavone FS, et al. Quantification of Myocyte Disarray in Human Cardiac Tissue. *Front Physiol*. 2021;12:750364.
82. team Tpd. pandas-dev/pandas: Pandas 0.25.3. v0.25.3 ed: Zenodo; 2022.
83. McKinney W, editor *Data Structures for Statistical Computing in Python*. Python in Science Conference; 2010 2010. Austin, Texas.
84. D'Agostino R, Pearson ES. Tests for Departure from Normality. Empirical Results for the Distributions of b^2 and \sqrt{b} . *Biometrika*. 1973;60(3):613-22.
85. D'Agostino RB. An Omnibus Test of Normality for Moderate and Large Size Samples. *Biometrika*. 1971;58(2):341-8.
86. Waskom M. seaborn: statistical data visualization. *JOSS*. 2021;6(60):3021.

87. community M. matplotlib/matplotlib: REL: v3.1.1. v3.1.1 ed: Zenodo; 2019.
88. Hunter JD. Matplotlib: A 2D Graphics Environment. *Comput Sci Eng.* 2007;9(3):90-5.
89. Ramachandran P, Varoquaux G. Mayavi: 3D Visualization of Scientific Data. *Comput Sci Eng.* 2011;13:40-51.
90. Schmid B, Schindelin J, Cardona A, Longair M, Heisenberg M. A high-level 3D visualization API for Java and ImageJ. *BMC Bioinformatics.* 2010;11(1):274.
91. Fast VG, Kleber AG. Role of wavefront curvature in propagation of cardiac impulse. *Cardiovasc Res.* 1997;33(2):258-71.
92. Whitaker J, Rajani R, Chubb H, Gabrawi M, Varela M, Wright M, et al. The role of myocardial wall thickness in atrial arrhythmogenesis. *Europace.* 2016;18(12):1758-72.
93. Hansen BJ, Zhao J, Fedorov VV. Fibrosis and Atrial Fibrillation: Computerized and Optical Mapping; A View into the Human Atria at Submillimeter Resolution. *JACC Clin Electrophysiol.* 2017;3(6):531-46.
94. Balaban G, Costa CM, Porter B, Halliday B, Rinaldi CA, Prasad S, et al. 3D Electrophysiological Modeling of Interstitial Fibrosis Networks and Their Role in Ventricular Arrhythmias in Non-Ischemic Cardiomyopathy. *IEEE Trans Biomed Eng.* 2020;67(11):3125-33.
95. Bishop MJ, Plank G, Burton RA, Schneider JE, Gavaghan DJ, Grau V, et al. Development of an anatomically detailed MRI-derived rabbit ventricular model and assessment of its impact on simulations of electrophysiological function. *Am J Physiol Heart Circ Physiol.* 2010;298(2):H699-718.
96. Clayton RH, Bernus O, Cherry EM, Dierckx H, Fenton FH, Mirabella L, et al. Models of cardiac tissue electrophysiology: progress, challenges and open questions. *Prog Biophys Mol Biol.* 2011;104(1-3):22-48.
97. Clayton RH, Panfilov AV. A guide to modelling cardiac electrical activity in anatomically detailed ventricles. *Prog Biophys Mol Biol.* 2008;96(1-3):19-43.

98. Crozier A, Augustin CM, Neic A, Prassl AJ, Holler M, Fastl TE, et al. Image-Based Personalization of Cardiac Anatomy for Coupled Electromechanical Modeling. *Ann Biomed Eng.* 2016;44(1):58-70.

Thanks

The first person that comes to my mind it's my scientific supervisor, Dr. Leonardo Sacconi, who guided me throughout my Ph.D. with great professionalism, knowledge, and kindness. Leo, I have learned so much from your experience, and in that long journey, you have also become a very good friend.

Right after, I would like to thank all the members of the Cardiac Imaging Group of the European Laboratory for Non-Linear Spectroscopy. Without our intense teamwork, this thesis would never have existed. My gratitude goes in particular to Camilla Olianti, for the effort to optimize the tissue transformation techniques applied to the cardiac tissue, and for helping me process the huge amount of structural data; to Dr. Valentina Biasci, for the optical mapping measurements and for her support in electrophysiological results understanding; to Giulia Arecchi, for all the support received in performing the structural measurements and interpreting them; to Dr. Gerard Marchal, for his contribution in the functional analysis and during my thesis correction, to Dr. Erica Lazzeri, last but not least, for being a support when I was taking my first steps in a biochemical laboratory during my first year.

A huge thank you to my two Ph.D. scholarship mentors, Prof. Elisabetta Cerbai and Prof. Corrado Poggesi. It was an honor to be watched by two personalities of such a high scientific and human standard.

I would like to thank Dr. Martin Bishop for welcoming me in the best possible way in his Computational Cardiac Electrophysiology group, during my visit to the School of Biomedical Engineering & Imaging Sciences at King's College London. Dr. Bishop followed me with professionalism and helpfulness. Together with him and with Sofia Monaci, Dr. Fernando Campos, and Dr. Elias Karabelas, I really learned a lot about the fascinating

world of computational modeling. This was a wonderful experience in a wonderful city.

A thought also goes to Prof. Marco Mongillo and Dr. Tania Zaglia, from the University of Padua, for the animal model provision on which this project was based, and for their highest scientific level advice.

I also thank Prof. Gabriella Nesi, from the Department of Health Sciences of the University of Florence, for performing histological inspections to validate our methodology.

Many thanks to Prof. Cecilia Ferrantini and Dr. Giulia Vitali that, together with Prof. Poggesi, included me in their research projects about the biomechanics of muscle tissue, which resulted (and I hope will result) in interesting scientific articles.

I would also like to thank Prof. Leonardo Bocchi, from the Information Engineering Department of the University of Florence, and Dr. Giacomo Mazzamuto, Dr. Ludovico Silvestri, and Dr. Irene Costantini, from the Brain Imaging Group of L.E.N.S., for all their advice during these 3 years.